

SEARCHES FOR GAUGE MEDIATED  
SUPERSYMMETRY BREAKING AT ALEPH  
WITH CENTRE-OF-MASS ENERGIES  
UP TO 209 GeV

by

Arán García-Bellido



Department of Physics  
Royal Holloway  
University of London

A thesis submitted to the University of London  
for the degree of Doctor of Philosophy  
September, 2002

# Searches for gauge mediated supersymmetry breaking at ALEPH with centre-of-mass energies up to 209 GeV

Arán García-Bellido

Royal Holloway University of London

A total of  $628 \text{ pb}^{-1}$  of data collected with the ALEPH detector at centre-of-mass energies from 189 to 209 GeV is analysed in the search for gauge mediated supersymmetry breaking (GMSB) topologies. In this framework, a novel search for six-lepton final states when the stau is the next-to-lightest supersymmetric particle (NLSP) and has negligible lifetime is performed. Other possible signatures at LEP are studied and the ALEPH final results described for two acoplanar photons, non-pointing single photons, acoplanar leptons, large impact parameter leptons, detached slepton decay vertices, heavy stable charged sleptons and multi-leptons plus missing energy final states. No evidence is found for new phenomena, and lower limits on the masses of the relevant supersymmetric particles are derived. A scan of a minimal GMSB parameter space is performed and lower limits are set for the NLSP mass at  $54 \text{ GeV}/c^2$  and for the mass scale parameter  $\Lambda$  at  $10 \text{ TeV}/c^2$ , independent of the NLSP lifetime. Including the results from the neutral Higgs boson searches, a NLSP mass limit of  $77 \text{ GeV}/c^2$  is obtained and values of  $\Lambda$  up to  $16 \text{ TeV}/c^2$  are excluded.

## Acknowledgements

I am grateful to the following people for their help and support during the last three years.

It would have been impossible for me to come to Royal Holloway without the effort and perseverance of Mike Green who has also been a great advisor.

I cannot be thankful enough to Grahame Blair for his supervision throughout my PhD. I treasure the conversations I have had with him whether related to work, physics or my future. He has been a source of knowledge, guidance, motivation and encouragement. I just hope one day I can become that good.

I would like to thank Fabio Cerutti for his help and dedication with the scan, based on his previous work. The people involved in GMSB searches at ALEPH, Gary Taylor, Barbara Clerbaux, Chris Booth, Fabio Cerutti, Paolo Azzurri, Eva Bouhova, Luke Jones and Jason Nielsen were all of immense help to explain and provide their results. Needless to say, this thesis could not have been done without them. A special thank you to Christoph Rembser, always joyful and supportive, for pointing me towards the six-lepton topology and for doing such a fantastic job in the GMSB LEP combination.

Grahame Blair, Mike Green and Glen Cowan have read all or parts of this work and their comments and suggestions have been very helpful. Glen was always there to sort out my endless questions about statistics.

I acknowledge the support from CLRC and CERN who funded my stays in Geneva. Special thanks to Dieter Schlatter, Roberto Tenchini, Fabiola Gianotti and Fabio Cerutti for making the second one possible. The Physics Department also funded my attendance to schools and conferences.

Thanks to everyone in the HEP group at RHUL for being such a great crowd. David, Graham, Onuora, Omar, Fernando, Raúl, Jordi and Ana made life really enjoyable at CERN. Thanks for pulling me out of the office and teaching me the intricacies of rock climbing and kitchen-cloth squeezing.

My aunt Paloma in Oxford and my cousins Juan and Ester in Geneva have provided the warmth and affection of the family abroad. In Geneva, I had the good advice, hospitality, and a car from my cousins and I could even babysit from time to time the adorable Sara; in Oxford, I was the one babysitted.

Finally, my parents. I owe them everything. This thesis is dedicated to them.

Egham, September 2002.

# Contents

<b>Outline</b>	<b>1</b>
<b>1 The Standard Model and beyond: Supersymmetry</b>	<b>2</b>
1.1 Symmetries in physics: the Standard Model	3
1.1.1 Electroweak symmetry breaking	4
1.1.2 Defects of the SM	5
1.2 The last symmetry: Supersymmetry	8
1.2.1 Supersymmetry breaking	11
1.2.2 Super-Higgs mechanism and the gravitino	12
1.3 Gravity mediated SUSY breaking	13
1.4 Gauge mediated SUSY breaking	15
1.5 Collider signatures	16
<b>2 Experimental Overview</b>	<b>20</b>
2.1 The LEP collider	21
2.2 The ALEPH detector	22
2.3 Charged Particle Tracking	23
2.3.1 Vertex Detector	23
2.3.2 Inner Tracking Chamber	25
2.3.3 Time Projection Chamber	26
2.4 Calorimetry and Luminosity Monitors	28
2.4.1 Electromagnetic Calorimeter	28
2.4.2 Hadron Calorimeter	29
2.4.3 Muon Chambers	31
2.4.4 Luminosity Monitors	31
2.5 Trigger System	32
2.6 Event reconstruction	33
2.6.1 Track reconstruction	33
2.6.2 Energy Flow	34
2.6.3 Lepton Identification	34
2.7 Event Simulation	39
<b>3 Searches for six-lepton final state topologies in GMSB</b>	<b>40</b>
3.1 Phenomenology	41
3.1.1 Available parameter space	43
3.1.2 Kinematics of two- and three-body $\tilde{l}_R$ decays	43
3.2 Data sample and Monte Carlo simulation	46
3.2.1 Data sample	48

3.2.2	Signal . . . . .	48
3.2.3	Background . . . . .	49
3.3	Signal Selection . . . . .	53
3.3.1	Description of the selections . . . . .	53
3.3.2	Optimisation . . . . .	56
3.3.3	Selection efficiencies . . . . .	61
3.4	Results . . . . .	62
3.4.1	Events selected in the data . . . . .	62
3.4.2	Limits on slepton production . . . . .	63
<b>4</b>	<b>GMSB searches and present limits</b>	<b>68</b>
4.1	Description of GMSB topologies . . . . .	69
4.2	Searches for neutralino NLSP . . . . .	70
4.2.1	Acoplanar photons . . . . .	70
4.2.2	Non-pointing photons . . . . .	71
4.2.3	Indirect searches . . . . .	73
4.3	Searches for slepton NLSP . . . . .	73
4.3.1	Acoplanar leptons . . . . .	73
4.3.2	Large impact parameters and kinks . . . . .	73
4.3.3	Heavy stable charged particles . . . . .	76
4.3.4	Cascade decays of neutralinos . . . . .	79
4.4	Neutral Higgs boson searches in the MSSM . . . . .	81
<b>5</b>	<b>Interpretation of results</b>	<b>83</b>
5.1	The scan . . . . .	84
5.1.1	Scan ranges . . . . .	84
5.1.2	Exclusion procedure . . . . .	85
5.2	Lower limit on the NLSP mass . . . . .	86
5.3	Lower limit on the mass scale parameter $\Lambda$ . . . . .	88
5.3.1	Validity of the limits . . . . .	89
5.4	Lower limit on the gravitino mass . . . . .	91
<b>6</b>	<b>Summary and discussion</b>	<b>93</b>
6.1	This work . . . . .	93
6.2	GMSB after LEP . . . . .	94
6.3	Prospects . . . . .	95
	<b>List of Figures</b>	<b>98</b>
	<b>List of Tables</b>	<b>100</b>
	<b>Bibliography</b>	<b>101</b>

# Outline

This thesis describes the final searches performed by the ALEPH collaboration at LEP for supersymmetry (SUSY) when a light gravitino is the lightest supersymmetric particle. The first chapter is devoted to symmetries in particle physics: those of the Standard Model and supersymmetry. The limitations of the Standard Model are reviewed and the solutions given by supersymmetry are analysed. The fact that SUSY is a broken symmetry, and a very difficult one to break, will lead to a variety of possible models. Gravity mediation and gauge mediation, the subject of this thesis, will be presented and the production and decay of the predicted new particles will be introduced.

In Chapter 2 the ALEPH detector and its analysis tools are explained. Chapter 3 documents the search for selectron or smuon production developed by the author to cover the case of heavy neutralinos and light staus with zero lifetime. Chapter 4 summarises all other searches carried out by other collaborators within ALEPH in the context of gauge mediated SUSY breaking (GMSB) scenarios, including neutral Higgs boson searches. Together with the six-lepton topology described in Chapter 3, these results are interpreted in terms of excluded areas in the minimal GMSB parameter space. Chapter 5 describes the scan performed by the author over these parameters and the combined results on mass limits, cross sections, and the input parameters of the theory.

Chapter 6 will compare ALEPH results with other collaborations and overview the status of GMSB models after LEP. A brief look ahead is also given.

# Chapter 1

## The Standard Model and beyond: Supersymmetry

The Standard Model of fundamental interactions is probably one of the most accurately tested theories in physics. Its foundations will be briefly reviewed here, stressing the importance of symmetries as the organising principle behind it. Symmetries provide an important route to advance the understanding and development of a theory. But sometimes as well as discovering a fundamental symmetry it is as important to know how to break it. The concept of spontaneous symmetry breaking is also central to the Standard Model, and it leads to the main untested sector of the theory: the Higgs sector. Hereafter, the problems of the Standard Model are outlined and a possible solution in terms of a new (ultimate) symmetry will emerge.

Supersymmetry is regarded as the most likely incarnation of physics beyond the Standard Model to be accessible at present experiments. The strong points of the theory are studied in this chapter and special attention is given to the consequences of the breaking of this symmetry. The different phenomenological consequences for current particle colliders will be described paying special attention to the framework of this thesis: models where the electroweak and strong interactions (and not gravity) mediate the breaking.

## 1.1 Symmetries in physics: the Standard Model

The Standard Model (SM) of particle physics describes the electromagnetic, weak and strong interactions in terms of the internal symmetries they exhibit. The discovery of a symmetry in Nature provides the means not only to describe observations, but to *construct* theories and make powerful predictions based on calculations from conserved quantities.

In the Standard Model [1, 2, 3], the forces between the fundamental particles are mediated by the exchange of spin-1 bosons. Thus the electromagnetic force is ‘carried’ by the photon which couples to charged particles, the weak force couples all fermions by the W and Z bosons, and the strong force couples quarks via the gluons and accounts for the stability of nucleons. Table 1.1 lists all four known interactions and the corresponding force carriers. The constituents of matter are spin- $\frac{1}{2}$  fermions, the leptons and quarks, which come in three families (or generations), as listed in Tab. 1.2.

Interaction	Strength	Range	Carrier particles		
			Name	Mass ( $\text{GeV}/c^2$ )	Spin
Strong	$\alpha_3 \sim 0.121$	$10^{-15}\text{m}$	Gluons (g)	0	1
Electromagnetic	$\alpha_1 \sim 1/128$	$\infty$	Photon ( $\gamma$ )	0	1
Weak	$\alpha_2 \sim 10^{-6}$	$10^{-17}\text{m}$	$Z^0, W^\pm$	91.2, 80.4	1
Gravitation	$G_N \sim 10^{-39}$	$\infty$	Graviton (G)	0	2

Table 1.1: The four interactions in Nature, with the corresponding boson carriers. The values of the couplings  $\alpha$  are measured at the Z mass; they evolve with energy. The graviton has not yet been observed. The gravitational constant  $G_N$  has units of  $(\text{GeV}/c^2)^{-2}$ . Adapted from Ref. [4].

		Leptons			Quarks		
		Name	$Q$	Mass ( $\text{MeV}/c^2$ )	Name	$Q$	Mass ( $\text{MeV}/c^2$ )
Families	1 <sup>st</sup>	electron	$e - 1$	0.511	up	$u + 2/3$	1–5
		e-neutrino	$\nu_e 0$	$< 3 \times 10^{-6}$	down	$d - 1/3$	3–9
	2 <sup>nd</sup>	muon	$\mu - 1$	106	charm	$c + 2/3$	1150–1350
		$\mu$ -neutrino	$\nu_\mu 0$	$< 0.19$	strange	$s - 1/3$	75–170
	3 <sup>rd</sup>	tau	$\tau - 1$	1780	top	$t + 2/3$	$174 \pm 5 \times 10^3$
		$\tau$ -neutrino	$\nu_\tau 0$	$< 18.2$	bottom	$b - 1/3$	4000–4400

Table 1.2: The fermions in the SM are grouped into three families (or generations). Leptons feel the electroweak force whilst quarks also feel the strong force. Masses are given in  $\text{MeV}/c^2$  [5]. Only upper limits exist on the mass of neutrinos. The quark masses cannot be precisely determined since QCD forbids isolated quarks. For each fermion  $f$  there is an antifermion  $\bar{f}$  with opposite electric charge  $-Q$ .

By imposing certain symmetries, one can write down the Lagrangian and thus derive the equations of motion for all particles described above. This is the beauty of the theory: specify a global symmetry group and the nature of the interaction is fully determined. So by building on experiment, one learns the following symmetries need to be fulfilled by the Standard Model Lagrangian:



- Poincaré invariance [4]. The theory must be invariant under continuous spacetime transformations such as translations, rotations and Lorentz transformations, i.e. the SM obeys the laws of Special Relativity. These symmetries imply the conservation of linear momentum, angular momentum and 4-momentum, respectively.
- The CPT symmetry, which swaps the charge, parity and time flow of the process, must be respected exactly. This implies the conservation of the corresponding discrete quantum numbers.
- And finally, the gauge (phase) symmetries. The Standard Model is based on the local symmetry group  $SU(3)_C \otimes SU(2)_L \otimes U(1)_Y$ . This structure uniquely determines the form of the interactions. The  $SU(3)_C$  symmetry is that of the strong interaction between quarks, which can transform one quark to another by means of eight gauge bosons (the gluons) conserving the colour charge. Similarly, the gauge invariance under  $SU(2)_L$  requires three gauge fields (eventually the  $W^+$ ,  $W^-$  and  $Z^0$ ) and conserves the weak isospin  $I_L$ . This symmetry allows an up-type fermion to interact with a down-type fermion via the weak force. And the group  $U(1)$  is associated with one boson field and conserves the hypercharge  $Y$ , giving rise to the electromagnetic force. Actually, only left-handed fermions which are weak isospin doublets like  $(\nu_e)_L$  will couple to the  $SU(2)_L$  gauge bosons. Right-handed fermions are isospin singlets like  $u_R$ , and can only interact if they carry non-zero hypercharge or colour quantum numbers.

At this stage the theory is gauge invariant, i.e. transforming the fermion fields in the theory by a local phase shift requires the introduction of gauge bosons to leave the Lagrangian unchanged. But all the particles in the theory are massless. Indeed, fermion masses should appear in terms like  $m\bar{\psi}\psi = m(\bar{\psi}_L\psi_R + \bar{\psi}_R\psi_L)$ , which explicitly breaks the  $SU(2)_L \otimes U(1)_Y$  symmetry in which left-handed fields transform independently of right-handed fields. And similarly for vector boson mass terms like  $\frac{1}{2}m^2W_\mu W^\mu$ . Nevertheless, by inspecting Tables 1.1 and 1.2, it is obvious that fermions have mass and the weak bosons are (very) massive. The  $Z$  and  $W$  bosons *have* to be massive to give the weak interactions a very short range. Thus some mechanism to break the  $SU(2)_L \otimes U(1)_Y$  symmetry into  $U(1)_{em}$  is needed if the theory is to describe massive  $W$  and  $Z$  bosons and a massless photon.

### 1.1.1 Electroweak symmetry breaking

An elegant way of introducing massive gauge bosons for the weak interactions without explicitly breaking the  $SU(2)_L \otimes U(1)_Y$  gauge invariance of the Lagrangian, was proposed by Higgs and others [6, 7] using the concept of *spontaneous symmetry breaking*. Briefly, the introduction of a complex spin-0 (scalar) field  $\phi$  does the job if it is a doublet in  $SU(2)_L$  and its potential respects the most general  $SU(2)_L \otimes U(1)_Y$  gauge invariant form:

$$V(\phi) = \mu^2\phi^\dagger\phi + \lambda(\phi^\dagger\phi)^2 \quad ; \quad \phi = \sqrt{\frac{1}{2}} \begin{pmatrix} \phi_1 + i\phi_2 \\ \phi_3 + i\phi_4 \end{pmatrix} \quad (1.1)$$

where  $\mu$  is the mixing parameter and  $\lambda$  is the quartic scalar self-coupling. For  $\mu^2 < 0$  and  $\lambda > 0$ , the above potential has an infinite number of non-zero solutions for which only the field's norm is known:  $|\phi|^2 = \frac{1}{2}(\phi_1^2 + \phi_2^2 + \phi_3^2 + \phi_4^2) = -\mu^2/2\lambda \equiv v^2/2$ , where  $v$  is the energy scale at which the electroweak symmetry will be broken. The fundamental state is thus degenerate (the circle of vacuum states at  $V(\phi) = 0$  in Fig 1.1b and  $SU(2)_L$  is broken when only one of the

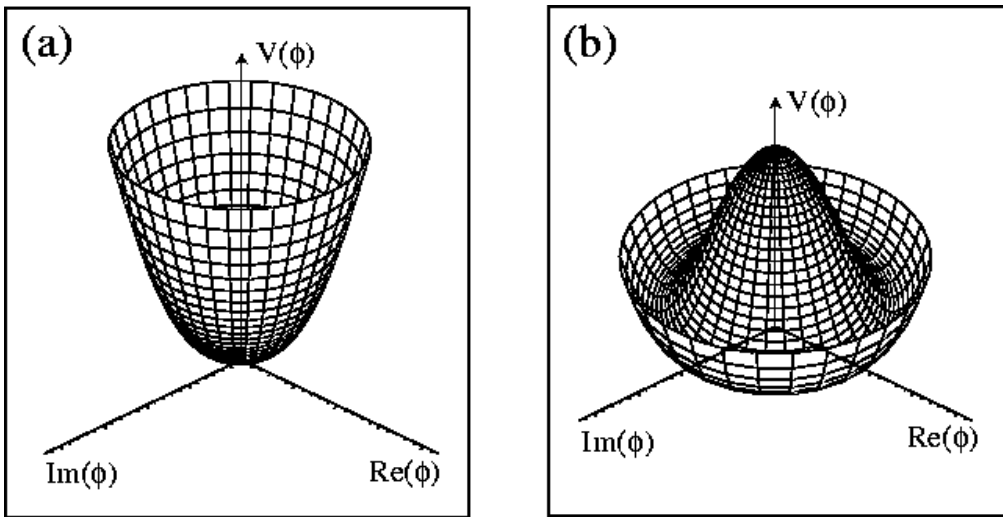


Figure 1.1: The scalar potential  $V(\phi) = \mu^2 \phi^\dagger \phi + \lambda (\phi^\dagger \phi)^2$  for a single complex field  $\phi = \phi_1 + i\phi_2$ , with (a)  $\mu^2 > 0$  and (b)  $\mu^2 < 0$ . In (a) the minimum (ground state) is at  $\text{Re}\phi = \text{Im}\phi = 0$ , while for (b) the minimum of the potential is at  $|\phi| = v/\sqrt{2} = 174 \text{ GeV}$ , which describes a circle in the  $(\text{Re}\phi, \text{Im}\phi)$  plane. Any point in the circle is equally likely, thus the spontaneous symmetry breaking occurs when only one vacuum state gets chosen, e.g.  $\phi_1 = v; \phi_2 = 0$ . From Ref. [8].

infinite points in the circle is chosen by the physical vacuum. Such a choice, for example  $\phi_3 = v; \phi_{1,2,4} = 0$ , constitutes a spontaneous breaking of the invariance around the circle, but leaves  $U(1)_{\text{em}}$  unbroken. This is the essence of spontaneous symmetry breaking in the Higgs mechanism: the physical vacuum adopts a specific ground state with non-zero expectation value  $v/\sqrt{2}$  (thus naturally breaking the symmetry) but the Lagrangian remains invariant.

By spontaneously breaking a continuous symmetry, massless particles called Goldstone bosons must be produced [9]. In this case the electroweak gauge symmetry had four scalar degrees of freedom  $\phi_{1,2,3,4}$ , but only  $SU(2)$  is broken thus only three massless Goldstone bosons are expected. These three degrees of freedom are interpreted as the longitudinal components of the three now massive vector bosons  $W^+, W^-$  and  $Z^0$ . The fourth degree of freedom is predicted to be the Higgs boson  $H^0$ , the only particle in the Standard Model yet to be discovered.

In summary, the Higgs mechanism has allowed the massless weak bosons to become massive by eating up the Goldstone bosons arising from the  $SU(2)$  breaking, while keeping the photon massless. Furthermore, it predicts the existence of a scalar boson with mass  $m_H = \sqrt{-2\mu^2}$ , which is a free parameter and must be experimentally measured. The fermion masses can then be generated by Yukawa couplings  $g_f$  between the fermion fields and the Higgs field of the form:  $g_f[\bar{\psi}_L \phi \psi_R + \bar{\psi}_R \phi^\dagger \psi_L]$ . The inner products of Higgs and left-handed fermion doublets of  $SU(2)_L$  yield gauge invariant singlets, so these terms can now be added to the Lagrangian without destroying its invariance.

### 1.1.2 Defects of the SM

The Standard Model is not only an elegant description of the symmetries behind matter and interactions. It has been tested in detail by experiments and agreement has always been found between the measured and predicted values from the theory [5]. However, despite its experimental success, there remain some theoretical issues which make it impossible for it to be a complete description of Nature. They are reviewed here.

## Gravity

The Standard Model is an accurate description of the electromagnetic, weak and strong interactions, but does not include the fourth known force: gravity. Newton's constant has dimensions of the inverse of a mass squared ( $G_N = 1/M_P^2$ , where  $M_P \sim 10^{19}$  GeV is the Planck mass where quantum effects become important) whereas the other interactions have dimensionless coupling constants. In General Relativity, gravity, as a force, manifests itself through deformations in spacetime. In the Standard Model the spacetime is assumed to be flat and forces to arise from the exchange of quanta. This is probably one of the remaining great issues to be resolved in physics: how to make the Standard Model and General Relativity compatible.

## Number of free parameters

Ideally, one would expect that the three coupling constants ( $\alpha_1, \alpha_2, \alpha_3$  for each symmetry group in Tab. 1.1) would be the only free parameters of the theory. Assigning the matter particles to a specific representation of the gauge group and then measuring the couplings should be enough to have a complete theory of Nature. Conversely, the SM has at least 28 arbitrary parameters to account for: three gauge couplings; two parameters in the Higgs potential ( $\mu$  and  $\lambda$ ); 12 fermion masses (including the neutrinos); three mixing angles and one phase in the quark sector and another three mixing angles and three phases in the lepton sector for massive neutrinos; and finally one CP violation phase in the strong interaction.

## Fermion masses

Looking back at Tab. 1.2 the diversity of observed masses for the fermions is striking. As was mentioned in the previous section, the Higgs mechanism incorporates massive fermions into the theory while keeping the Lagrangian gauge invariant. The couplings between the Higgs and the fermion fields are proportional to the fermion masses:  $g_f = \sqrt{2}m_f/v$ . If  $v/\sqrt{2} = 174$  GeV, why is the top-quark Yukawa coupling so close to one and the electron's five orders of magnitude weaker? The SM does not explain this mass hierarchy.

The recent experimental evidence for neutrino oscillations [10, 11], only possible if they are massive, strongly suggests physics beyond the SM. The extreme smallness of their masses ( $m_\nu \lesssim 0.2 \text{ eV}/c^2 \sim 10^{-6}m_e$ ) indicates that their origin cannot be the Higgs mechanism. Such small masses may only arise if the existence of right-handed neutrinos is postulated (Dirac masses, e.g.  $\overline{\nu}_R m_D \nu_L$ ) or if a Majorana nature of the neutrinos is invoked (if the neutrino is its own antiparticle:  $\nu_L^T m \nu_L$ ) [12]. In both cases, the origin of neutrino masses must be linked with an energy high enough to violate lepton number L.

## Dark matter and the baryon asymmetry

Conventional matter, made of baryons like the proton and the neutron, represents  $\lesssim 5\%$  of the total energy content of the Universe according to Big-Bang nucleosynthesis [13] and cosmic microwave background (CMB) radiation [14] analyses. Studies of large-scale structure, rotation curves in spiral galaxies, luminous matter and CMB, suggest that the total amount of dark matter in the Universe corresponds to about 30% of the total energy density  $\rho_c \sim 5 \times 10^{-6} \text{ GeV}/\text{cm}^3$  [15]. If the SM seems to describe only 5% of  $\rho_c$ , what kind of matter is this remaining 30%?

Furthermore, why is the Universe made of matter and not antimatter? The SM equations are the same for matter and antimatter, but then there is no evidence for antimatter galaxies

or stars in the Universe, only matter. Three conditions are required to generate a baryon asymmetry [16]: the baryonic quantum number  $B$  cannot be conserved; the  $C$  and  $CP$  symmetries are violated; and a period of thermal inequilibrium is necessary for the asymmetry not to be washed away. Although the SM could accommodate in non-perturbative processes a violation of the baryon number, and  $CP$  violation arises naturally in a three generation model, it seems the amount of  $CP$  violation predicted in the SM is not sufficient [17]. Today there are  $\sim 10^9$  photons for each baryon in the Universe, so at some point there had to be roughly one extra quark per billion  $q\bar{q}$  pairs. The origin of this asymmetry requires the existence of physics beyond the SM with a stronger  $CP$  violation.

### Hierarchy or naturalness problem

Paradoxically, it is a particle whose existence is not yet proven that poses the most serious threat to the Standard Model. The Higgs boson mass is a free parameter in the Standard Model, but for the theory to be valid it must be bound from below and, specially, from above. However, the Higgs mass in the Standard Model gets contributions from loops with the gauge bosons, fermions and with itself, as seen in Fig. 1.2. The problem arises when considering radiative corrections from scalar particles, as in Fig. 1.2c. Gauge boson and fermion masses are protected against divergences, so their loops do not pose a problem.

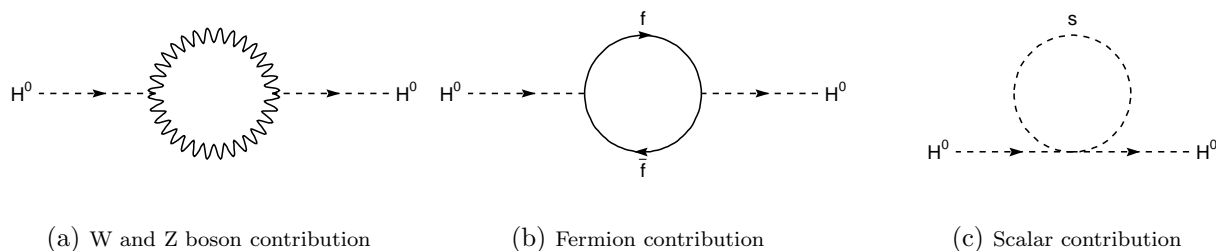


Figure 1.2: One-loop quantum corrections to the Higgs mass.

Scalar particles tend to get masses of the order of the largest mass scale in the theory. And if the SM is to hold unscathed up to the energy where gravity becomes strong,  $M_P$ , then the quantum corrections to the Higgs mass diverge. Normally one introduces a cutoff energy scale  $\Lambda$  between the  $W$  mass and  $M_P$ , above which the SM is invalid and some new physics must appear. Thus the Higgs mass will be given by some ‘bare’ mass term  $m_0^2$  (where no assumption on new physics is made) and the corrections that involve the new energy scale:  $m_H^2 \simeq m_0^2 + \delta m_H^2 + \dots$ , with:  $\delta m_H^2 = \mathcal{O}\left(\frac{\alpha}{\pi}\right) \Lambda^2$ . Then, if on the one hand the Higgs mass involves radiative terms of order  $\Lambda^2 \sim 10^{38} \text{ GeV}^2$ , but on the other hand it is known to be of the order of the electroweak symmetry breaking scale ( $m_H^2 \sim -v^2$ ), how is it possible that the bare mass is so finely tuned as to exactly absorb the enormous radiative contributions and be left with the correct physical value? This unnatural fine tuning (of up to 34 orders of magnitude) is referred to as the *hierarchy* or *naturalness problem*. It can also be expressed as: why is the  $W$  mass much smaller than the Planck mass? Or equivalently, why is the Coulomb potential for a typical particle mass  $m$  in the atom so much greater than the Newtonian potential:  $e^2 \gg G_N m^2 = m^2/M_P^2$ ?

All these reasons lead to the idea that the SM is only an effective theory at the present energy scale  $\sim 100 \text{ GeV}$  and that there must be a new more fundamental theory just around the corner, at  $\Lambda \lesssim \mathcal{O}(1) \text{ TeV}$ . Supersymmetry is widely accepted as the most promising extension of the SM to explain some of the theoretical problems outlined here.

## 1.2 The last symmetry: Supersymmetry

The symmetries of the SM involve scalar charges, such as colour or hypercharge, that link particles with the same spin:  $Q|J\rangle = |J\rangle$ . The basic idea in supersymmetry (SUSY) is to have fermionic charges that relate fermions and bosons, so that:

$$\hat{Q}|\text{fermion}\rangle = |\text{boson}\rangle \quad \text{and} \quad \hat{Q}|\text{boson}\rangle = |\text{fermion}\rangle. \quad (1.2)$$

Supersymmetry is therefore a transformation that relates states of different spin. Particles like bosons and fermions that in principle have a completely different nature may be linked and form part of the same representation.

Perhaps the most compelling argument for supersymmetry is that it is the last undiscovered symmetry allowed in scattering processes. Considering possible extensions of the Poincaré group, Coleman and Mandula [18] proved that the addition of any new operator which transforms as a boson leads to a trivial S-matrix, i.e. in particle scattering experiments the only allowed outcomes would be completely forward or backward scattering, which of course completely disagrees with observation. But this very strict ‘no-go’ theorem can be avoided if the operator is fermionic and as was demonstrated later [19], supersymmetry is actually the only extension of the Poincaré group which does not lead to a trivial S-matrix. So this argument should be persuasive enough: ‘in Nature something not illegal is compulsory’.

Supersymmetry is not only attractive aesthetically as an underlying theory for the SM, it is also a step towards unification with gravity<sup>1</sup>. Furthermore, it cures several of the SM shortcomings.

The supersymmetric algebra derived from the above conditions requires the existence of new particles with the same mass, gauge quantum numbers and couplings as the SM ones. Thus for each fermion in the SM there is a bosonic partner and *vice versa*, structured in *supermultiplets* like:

$$\left( \begin{array}{c} \text{fermion}(J = \frac{1}{2}) \\ \text{sfermion}(J = 0) \end{array} \right) \quad ; \quad \left( \begin{array}{c} \text{g. boson}(J = 1) \\ \text{gaugino}(J = \frac{1}{2}) \end{array} \right) \quad ; \quad \left( \begin{array}{c} \text{graviton}(J = 2) \\ \text{gravitino}(J = \frac{3}{2}) \end{array} \right) \quad (1.3)$$

which describe matter and Higgses, gauge fields and gravity, respectively. The convention in naming the superpartners (or sparticles) is to add a prefix ‘s’ (for scalar) to each fermion and a suffix ‘ino’ for each boson. Could any of the known particles be one of these superpartners? No, it is impossible to pair together any of the known fermions with the known bosons, for the simple reason that their internal quantum numbers do not match. For example, leptons have non-zero lepton number  $L = 1$ , but bosons have  $L = 0$ , thus they cannot form part of the same supermultiplet.

By predicting this plethora of new particles supersymmetry solves neatly the hierarchy problem. The radiative corrections from fermions and scalars (diagrams b and c in Fig. 1.2) now cancel each other naturally at all levels of loops [21]. For each positive scalar loop there is now a negative fermion loop with the same couplings. The radiative contribution to the Higgs mass becomes [20]:

$$\delta m_H^2 = -\frac{g_f^2}{16\pi^2} (\Lambda^2 + m_f^2) + \frac{g_s^2}{16\pi^2} (\Lambda^2 + m_s^2) + \dots$$

---

<sup>1</sup>Making supersymmetry a local (spacetime dependent) symmetry necessarily involves gravity. Local SUSY transformations are equivalent to a local coordinate transformation; therefore supersymmetry is entangled with a new approach to spacetime, which must be present in any viable ‘Theory of Everything’ [20].

$$\simeq \mathcal{O}\left(\frac{\alpha}{\pi}\right)(m_s^2 - m_f^2) \quad (1.4)$$

where the quadratic divergences have disappeared and the residual term is much smaller than  $m_H^2$  if the masses of the SUSY bosons and fermions are similar:

$$|m_s^2 - m_f^2| \lesssim 1 \text{ TeV}^2 \quad (1.5)$$

This means that a light Higgs boson, such as electroweak data constraints [22] and recent direct searches seem to suggest [23], might be only possible if SUSY exists at a relatively low energy.

Another appealing feature of SUSY is that it permits the unification of the three forces at a very high energy scale, which cannot be achieved within the SM. The three coupling constants  $(\alpha_1, \alpha_2, \alpha_3)$  are not constants at all, but depend on the energy. Every particle with mass  $m_X$  below a scale  $Q$  will contribute to the running of the couplings via loop corrections to the force carriers propagators and vertices [24]:

$$\frac{1}{\alpha_i(Q)} = \frac{1}{\alpha_i(m_X)} + 8\pi b_i \ln\left(\frac{Q}{m_X}\right) \quad i = 1, 2, 3 \quad (1.6)$$

where the coefficients  $b_i$  depend on the number of colours and the number of active flavours (particles whose mass threshold is below  $Q$ ), including Higgs bosons. These coefficients are different in the SM and SUSY, as can be seen in Fig. 1.3. In the SM the three lines do not intersect at a same energy, even allowing for experimental error bands on the measurements at present energies. But SUSY models do in fact permit a complete unification of the couplings at around  $Q_U = 10^{16}$  GeV. Although this is a nice feature of supersymmetry, it does not take into account anything else happening during some 14 orders of magnitude from the scale where SUSY is turned on up to the GUT (Grand Unified Theory) scale.

There are two more characteristics of SUSY models worth discussing. The first is that two Higgs doublets are needed to give mass to up-type fermions and down-type fermions separately. In the SM only one doublet  $\phi$  and its complex conjugate  $\phi^\dagger$  was sufficient, but in SUSY models  $\phi^\dagger\phi$  terms are not allowed since they do not transform appropriately under supersymmetric transformations. Then, two Higgs doublets  $\phi_1 = (\phi_1^+, \phi_1^0)$  and  $\phi_2 = (\phi_2^+, \phi_2^0)$  with opposite hypercharge ( $\mp 1$ ) are needed in order to give masses to the SM fermions. Both will acquire a non-zero vacuum expectation value, fixed like before:  $v_1^2 + v_2^2 = (246 \text{ GeV})^2$ , but their ratio is a free parameter, called  $\tan\beta$ :

$$\tan\beta \equiv \frac{\langle\phi_2\rangle}{\langle\phi_1\rangle} = \frac{v_2}{v_1} \quad (1.7)$$

This makes phenomenology somewhat more interesting since there are now eight degrees of freedom and only three of them get ‘eaten’ to give mass to the weak gauge bosons, leaving five physical massive particles: the lighter CP-even neutral  $h$ , the heavier CP-even neutral  $H$ , the CP-odd neutral  $A$  and two charged  $H^\pm$ . Once the two Higgs supermultiplets have been introduced, they can couple to each other in terms like  $\mu\phi_1\phi_2$ , where  $\mu$  is the mass mixing parameter, analogous to the Higgs mass  $m_H$  in the SM.

The other very important phenomenological consequence of SUSY models is that new terms which violate lepton- and baryon-number are now allowed in the Lagrangian and still are consistent with gauge symmetries. Couplings which violate both B and L are strongly constrained from nuclear physics and specially from the proton lifetime [25]. In the SM, B–L conservation was never imposed by hand but rather was an ‘accidental’ outcome of the theory. Since the strength of these couplings is severely limited, one can impose the conservation of a

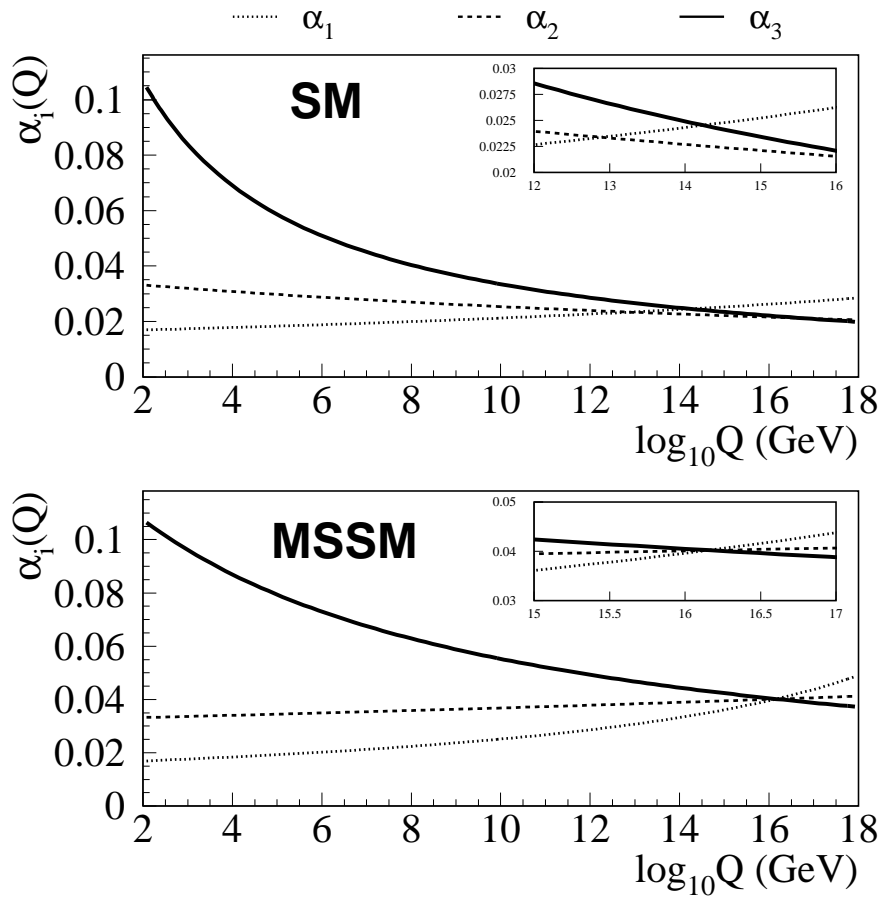


Figure 1.3: Evolution of the gauge couplings  $\alpha_i$  as a function of the energy  $Q$ , with the particle content of the Standard Model (above) and with the minimal supersymmetric extension of the SM (below). The energy scale where SUSY appears has been assumed to be  $10^2$  GeV.

new multiplicative quantum number: R-parity, defined as:

$$R_P = (-1)^{3B-L+2S} \quad (1.8)$$

where  $S$  is the spin of the particle. Standard Model particles will have  $R_P = +1$  and SUSY particles  $R_P = -1$ . To assume R-parity conservation, which is to some extent to impose B–L conservation by hand, has three fundamental consequences:

- sparticles are always produced in pairs,
- heavier sparticles decay to lighter ones, and
- the lightest sparticle is stable because it has no allowed decay mode.

The last point is perhaps the most attractive, since it implies the existence of heavy stable particles. If these are neutral they could very well constitute that 30% of the energy density of the Universe that must be in the form of cold dark matter [15]. However, R-parity conservation is not obligatory and there may exist terms, with maybe significant strength, that only violate B or L. Nonetheless, the work throughout this thesis assumes that R-parity is strictly conserved.

Standard Model Particles		Supersymmetric Particles			
		Weak Eigenstates		Mass Eigenstates	
particle	spin	particle	spin		
$q = u, d, c, s, t, b$	$\frac{1}{2}$	$\tilde{q}_L, \tilde{q}_R$	squarks	0	$\tilde{q}_1, \tilde{q}_2$
$\ell = e, \mu, \tau$	$\frac{1}{2}$	$\tilde{\ell}_L, \tilde{\ell}_R$	sleptons	0	$\tilde{\ell}_1, \tilde{\ell}_2$
$\nu = \nu_e, \nu_\mu, \nu_\tau$	$\frac{1}{2}$	$\tilde{\nu}$	sneutrinos	0	$\tilde{\nu}$
$g$	1	$\tilde{g}$	gluino	$\frac{1}{2}$	$\tilde{g}$
$\gamma$	1	$\tilde{\gamma}$	photino	$\frac{1}{2}$	$\chi_{1,2,3,4}^0$ neutralinos
$Z$	1	$\tilde{Z}$	zino	$\frac{1}{2}$	
$h, H, A$	0	$\tilde{H}_{1,2}^0$	neutral Higgsinos	$\frac{1}{2}$	
$W^\pm$	1	$\tilde{W}^\pm$	wino	$\frac{1}{2}$	$\chi_{1,2}^\pm$ charginos
$H^\pm$	0	$\tilde{H}^\pm$	charged Higgsinos	$\frac{1}{2}$	
$G$	2	$\tilde{G}$	gravitino	$\frac{3}{2}$	$\tilde{G}$

Table 1.3: The MSSM particle zoo.

### 1.2.1 Supersymmetry breaking

The major problem with SUSY is that it must be a broken symmetry. There is not a single piece of experimental evidence for SUSY in particle physics so far. If a supersymmetric companion of the electron existed with its same mass and spin-0 it would have been discovered long ago. The problem then is to write a SUSY Lagrangian with terms that make sparticles heavier than their SM counterparts, but do not introduce quadratic divergences to the Higgs mass (Eq. 1.5). These terms are thus said to induce a ‘soft SUSY breaking’. The origin of such terms is not known and several possibilities exist [26]. So in general one writes all possible terms [27] and does not make any assumption about *how exactly* SUSY is broken. But to parametrise our ignorance on the origin of these terms, at least 105 new free parameters must be introduced. They account for the sparticle masses, their mixing angles, 40 new CP violating phases, etc. . . Thus a theory that was simple and extraordinarily predictive becomes almost unmanageable, plagued with many more free parameters than before. The hope is that these parameters will be eventually explained by GUT-scale physics in terms of a few fundamental ones. Making some assumptions on how SUSY breaking is transmitted and imposing experimental constraints will lead to more predictive models as will be seen shortly.

The minimal supersymmetric extension of the Standard Model, or MSSM for short, can then be constructed in the most general way, allowing for R-parity violating terms and soft-SUSY breaking terms. The properties of the mass spectrum are now reviewed.

Table 1.3 lists the complete particle content of the MSSM. For each left- or right- handed fermion  $f_{L,R}$  there exist two different sfermions  $\tilde{f}_{L,R}$  with spin-0 and weak isospin  $\frac{1}{2}$  and 0, respectively. Of course the sfermions being scalars do not have a defined helicity, but they do have different weak isospin depending on the helicity of their SM partners. Once electroweak symmetry is broken these different weak isospin states are allowed to mix. Thus for each flavour a  $2 \times 2$  mixing matrix exists which will give the physical mass states from the weak eigenstates  $\tilde{f}_{L,R}$ . It takes the following general form [20]:

$$(\tilde{f}_L \quad \tilde{f}_R) \begin{pmatrix} m_f^2 + m_{\tilde{f}_L}^2 + m_D^2 & a_f m_f \\ a_f m_f & m_f^2 + m_{\tilde{f}_R}^2 + m_D^2 \end{pmatrix} \begin{pmatrix} \tilde{f}_L \\ \tilde{f}_R \end{pmatrix} \quad (1.9)$$



with

$$\begin{aligned} m_D^2 &\equiv m_Z^2 \cos 2\beta (I_3 + Q \sin^2 \theta_W) \\ a_f &\equiv \left( A_f - \mu \frac{\tan \beta}{\cot \beta} \right) \quad \text{for } f = \begin{matrix} e, \mu, \tau, d, s, b \\ u, c, t \end{matrix} \end{aligned} \quad (1.10)$$

where  $I_3$  is the third component of weak isospin,  $\sin^2 \theta_W = 0.23$  and  $A_f$  are the trilinear Higgs-sfermion-sfermion couplings arising from soft SUSY breaking. The off-diagonal terms depend on  $m_f$ , so it is clear that there will be more mixing for  $\tilde{t}_{L,R}$ , and if  $\tan \beta$  is large also for  $\tilde{b}_{L,R}$  and  $\tilde{\tau}_{L,R}$ . The mass eigenstates can be obtained by diagonalisation.

$$\begin{pmatrix} \tilde{f}_1 \\ \tilde{f}_2 \end{pmatrix} = \begin{pmatrix} \cos \theta_{\tilde{f}} & \sin \theta_{\tilde{f}} \\ \sin \theta_{\tilde{f}} & \cos \theta_{\tilde{f}} \end{pmatrix} \begin{pmatrix} \tilde{f}_L \\ \tilde{f}_R \end{pmatrix} \quad (1.11)$$

where  $\theta_{\tilde{f}}$  is the mixing angle. For example, in the case of stau mixing, Eqs. 1.9 and 1.11 are then related by:

$$\frac{m_{\tilde{\tau}_R}^2 - m_{\tilde{\tau}_L}^2}{m_\tau} = \frac{2(A_\tau - \mu \tan \beta)}{\tan 2\theta_{\tilde{\tau}}} \quad (1.12)$$

In general, the lighter mass eigenstate  $\tilde{\tau}_1$  will correspond to the right handed  $\tilde{\tau}_R$  state if there is no mixing ( $\theta_{\tilde{\tau}} = 0$  and  $A_\tau = \mu \tan \beta$ ). As the mixing increases (i.e. for increasing values of the mixing angle) the lighter  $\tilde{\tau}_1$  becomes an admixture of right- and left-handed staus, until  $\theta_{\tilde{\tau}} = 45^\circ$  which corresponds to maximal mixing. In this case the right- and left-handed components of the lightest stau are equal. Mixing is therefore more relevant in the third family: the lightest stau can be lighter than selectrons and smuons, and the lightest stop will generally be the lightest squark. Mixing will also occur between the massive fermionic companions of the electroweak gauge bosons. The photino  $\tilde{\gamma}$ , zino  $\tilde{Z}$  and neutral higgsinos  $\tilde{H}_{1,2}^0$  will mix to form the ‘neutralinos’:  $\chi_{1,2,3,4}^0$ , where the lower the index the lighter the particle. Similarly, the charged wino  $\tilde{W}^\pm$  and higgsino  $\tilde{H}^\pm$  give four charged mass eigenstates: the ‘charginos’  $\chi_{1,2}^\pm$ . The corresponding mixing matrices for neutralinos and charginos can be found in Ref. [28].

## 1.2.2 Super-Higgs mechanism and the gravitino

Returning to the problem of SUSY breaking, it turns out to be impossible to break SUSY in a phenomenological acceptable way if the only particles and interactions are those of the MSSM. In the SM, the Higgs vacuum expectation value determines the scale of electroweak breaking. But the specific masses of the bosons and fermions are dictated by the coupling of the forces that communicate the information of electroweak breaking: gauge and Yukawa couplings, respectively. In the MSSM, to give masses to the gauginos, for example, soft terms in the Lagrangian should contain tree level interactions of the type scalar-gaungino-gaungino, but these are not allowed in supersymmetry [28]. Similarly, squarks would be unacceptably light if their mass was generated at tree level as is the case in the SM [20].

Thus the soft mass terms must arise indirectly or radiatively: from the coupling of new particles to the particles in the MSSM. Supersymmetry breaking must therefore occur in a ‘hidden’ sector at a large energy scale. There the spontaneous breaking of local supersymmetry occurs and as a result some field  $F$  condensates, acquiring a non-zero expectation value  $F_0$ . Similarly to the Higgs mechanism, a Goldstone degree of freedom must now appear, but in this case it is a fermion since SUSY is a fermionic symmetry. This massless particle is the so-called ‘goldstino’, and its two polarisation states are ‘eaten’ by the massless gravitino, giving it a total of four polarisation states to become a massive spin- $\frac{3}{2}$  particle. The end result is then a massive gravitino and a massless graviton: local supersymmetry is thus successfully broken.

This *super-Higgs mechanism* is actually the only consistent way of breaking SUSY, as the Higgs mechanism was the only consistent way of breaking gauge symmetry [20]. The gravitino mass is then given by:

$$m_{\tilde{G}} = \frac{F_0}{\sqrt{3}M_{\text{P}}} \quad (1.13)$$

where  $F_0$  is the energy scale at which SUSY breaking occurs in the hidden sector (like  $v^2$  in the Higgs mechanism) and  $M_{\text{P}}$  is the reduced Planck mass:  $M_{\text{P}} = (8\pi G_{\text{N}})^{-1/2} = 2.4 \times 10^{18} \text{ GeV}/c^2$ . By dimensional analysis, it is intuitively clear that the gravitino should be massless in unbroken SUSY ( $F_0 \rightarrow 0$ ) or if gravity becomes irrelevant ( $M_{\text{P}} \rightarrow \infty$  or  $G_{\text{N}} \rightarrow 0$ ).

Now MSSM particles still have to be informed of the SUSY breaking. This can be achieved in different ways. Since all massive particles feel gravity, a natural candidate to communicate the hidden sector with the ‘visible’ sector where all MSSM particles sit, is the gravitational force. Thus *gravity mediated SUSY breaking* or supergravity (SUGRA) models, postulate the coupling between Planck-scale physics and the MSSM particles via gravity (exchanging gravitons). These weak couplings (of the order  $1/M_{\text{P}}$ ) generate acceptable soft mass terms and a definite MSSM spectrum. Another possibility is that the SUSY breaking is transmitted to the MSSM particles by the usual gauge  $SU(3)_{\text{C}} \otimes SU(2)_{\text{L}} \otimes U(1)_{\text{Y}}$  interactions. This case is referred to as *gauge mediated SUSY breaking* (GMSB) models and they imply the existence of an intermediate energy sector of particles, called ‘messengers’  $\Phi$  which will directly feel the SUSY breaking and then transmit it to the MSSM particles by radiative corrections, giving rise to a given MSSM mass spectrum. This last type of mediation is the framework of this thesis. A schematic drawing of the structure of SUSY breaking and mediation for these two scenarios is presented in Fig. 1.4. Both alternatives are discussed in the next sections.

A very nice feature of the super-Higgs mechanism is that it naturally induces electroweak symmetry breaking. If one assumes, as the unification of couplings suggests, that all fermion and boson masses unify at the GUT-scale with values  $m_0$  and  $m_{1/2}$  respectively, one can calculate all MSSM masses in terms of these GUT-scale input values. It turns out that  $m_0$  evolves with energy in such a way that drives the squared mass of the up-type Higgs negative due to the large (negative) radiative corrections from the top-quark Yukawa coupling and the stop mass. Indeed, electroweak symmetry breaking is generated radiatively and a link between the SUSY breaking Higgs masses and the electroweak scale  $m_Z$  can be obtained [29]:

$$\mu^2 = -\frac{m_Z}{2} + \frac{m_{H_1}^2 - m_{H_2}^2 \tan^2 \beta}{\tan^2 \beta - 1} \quad (1.14)$$

This again expresses the hierarchy problem in a different format: the  $\mu$  parameter on the left can be as big as the highest energy in the theory (it does not break any SM symmetry), but both  $m_Z$  and the Higgs masses on the right have to be of the order the electroweak scale. What makes  $\mu$  then lie in a physically acceptable region?

## 1.3 Gravity mediated SUSY breaking

If gravitational interactions are responsible for the soft mass terms, Planck-scale physics is the messenger of SUSY breaking [30]. A simplifying assumption, although not inevitable, is to consider the *universality* of masses and couplings. First, since the gauge couplings seem to unify at  $Q_{\text{U}} = 10^{16} \text{ GeV}$  (see Fig. 1.3), the gaugino masses  $M_1$ ,  $M_2$  and  $M_3$  for the photino, wino and gluinos respectively are also assumed to unify with a common value of:  $m_{1/2} \equiv M_i \sim m_{\tilde{G}}$  [20]. Secondly, the scalar masses-squared and the trilinear couplings are taken to be flavour-diagonal

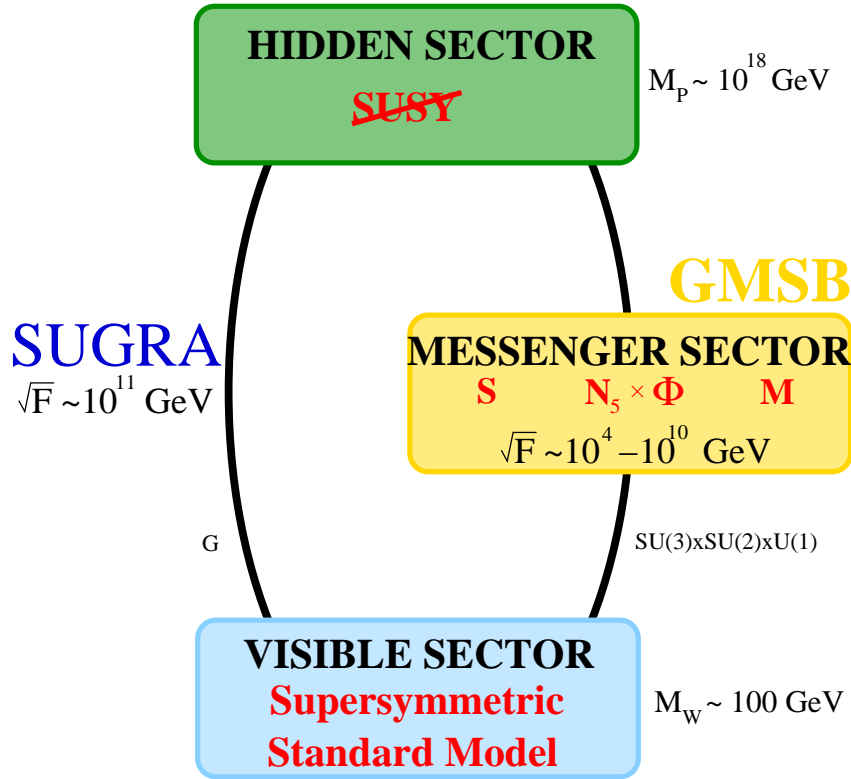


Figure 1.4: Supersymmetry breaking and its mediation. SUSY is broken (spontaneously) in a high-energy ‘hidden’ sector and its effects are transmitted radiatively to the ‘visible’ sector where all MSSM particles reside. The mediation can occur via gravity or gauge interactions.

and universal at  $m_0^2 \sim m_{\tilde{G}}^2$  and  $A_f = A_0 Y_f \sim m_{\tilde{G}}$ , where  $Y_f$  are the Higgs-fermion Yukawa coupling matrices. All the above relations are evaluated at the unification scale  $Q_U$  or  $M_P$ , and all of them are of the order  $F_0/M_P$  set by gravitational interactions. To calculate the mass of each particle in the visible sector, one runs the energy down from the known energy dependence of these parameters [28]. This set of assumptions lead to a very predictive model, called minimal supergravity (or mSUGRA), where only five parameters are needed to fully calculate the mass spectrum in the MSSM:

$$m_{1/2}, m_0, A_0, \tan \beta, \text{sign}(\mu) \quad (1.15)$$

where the absolute value of  $\mu$  can be calculated with Eq. 1.14 and only its sign remains a free parameter.

Since the soft masses have to be of the order of  $100 \text{ GeV}/c^2$ , and these are determined by parameters proportional to  $F_0/M_P$ , the scale of SUSY breaking  $\sqrt{F_0}$  in these type of models is predicted to be of the order of  $10^{11}$  GeV. In this type of models the gravitino is then expected to be heavy, comparable to the MSSM particles with  $m_{\tilde{G}} \sim 100 \text{ GeV}/c^2$  or so.

It is then found that the gaugino masses at any scale satisfy the relation [28]:

$$M_3 = \frac{\alpha_3}{\alpha} \sin^2 \theta_W M_2 = \frac{3\alpha_3}{5\alpha} \cos^2 \theta_W M_1 \quad (1.16)$$

which at the electroweak scale ( $\alpha_3 = 0.118$  and  $\alpha = 1/128$ ) becomes:  $M_3 : M_2 : M_1 \simeq 7 : 2 : 1$ .

It can also be derived that in mSUGRA the neutralino  $\chi_1^0$  is usually the lightest supersymmetric particle (LSP) [28]. If R-parity is conserved, signatures for SUSY in colliders will consist of missing energy carried away by the heavy, stable and very weakly interacting neutralino.

## 1.4 Gauge mediated SUSY breaking

In GMSB models [29] the splitting of masses in the MSSM is generated not at the Planck scale, but at some lower energy scale where pairs of very heavy messenger quarks and leptons exist. The gravitational interaction is still responsible for the communication between the hidden sector and this messenger sector, but its effects are now negligible in the MSSM. Gravity will couple to a singlet  $S$  in the messenger sector which will acquire a vacuum expectation value  $\sqrt{F_m}$ . This singlet breaks supersymmetry in the messenger sector and gives mass to all other messenger superfields  $\Phi$  there. In turn, these messengers are able to communicate with the MSSM via gauge interactions, but now from a much lower scale than  $M_P$ .

The key element in these models is then the structure of the messenger sector. The heavy messengers can be generally described as supermultiplets of  $SU(5) \supset SU(3) \otimes SU(2) \otimes U(1)$ , for which the parameter  $N_5$  is introduced and represents the number of families of  $\Phi$ . To a good approximation, once SUSY is broken in the messenger sector, the fields  $\Phi$  will share a common mass  $M_m$ .

The MSSM masses are then generated at one loop in the case of gauginos  $\lambda_i$  and two loops in the case of scalars  $\tilde{f}$ , taking into account that couplings are in both cases given by gauge  $\alpha_i$  strengths. Examples of the Feynman diagrams contributing to the MSSM masses are shown in Fig. 1.5.

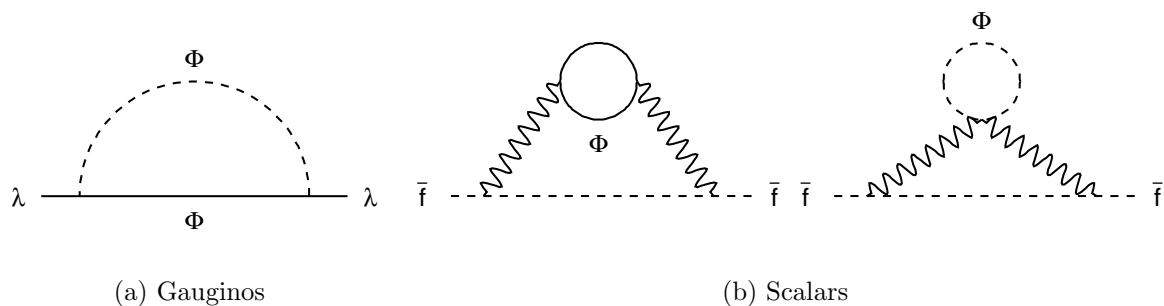


Figure 1.5: In GMSB, the (fermionic and bosonic) messengers  $\Phi$  give supersymmetry breaking masses to (a) gauginos  $\lambda$  at one loop and to (b) sfermions  $\tilde{f}$  at two loops. The coupling is via gauge interactions.

The masses can then be calculated at the messenger mass scale  $M_m$ , as [29]:

$$m_{\lambda_i} = \frac{\alpha_i}{4\pi} \Lambda N_5 \quad (1.17)$$

$$m_{\tilde{f}}^2 \simeq \left(\frac{\alpha_i}{4\pi}\right)^2 \Lambda^2 N_5 \quad (1.18)$$

where the parameter  $\Lambda \equiv F_m/M_m$  represents the universal mass scale of SUSY particles (like  $m_0$  or  $m_{1/2}$  in SUGRA). The most noticeable consequence is the degeneracy between squark and slepton masses. In SUGRA models the different flavour masses arise directly from a high energy  $M_P$  where flavour symmetry is respected. There is no control then on the mass

difference between squarks and sleptons, which could be in principle very large. These possible flavour-breaking soft mass terms are very dangerous, because they lead to flavour changing neutral currents (FCNC) and large CP violation. Both of which are strongly constrained by observations [5]. Measurements of the  $\bar{K}^0$ - $K^0$  mass difference and  $\mu \rightarrow e\gamma$  decays set stringent bounds on the possible mass difference between squarks and sleptons [29]. In GMSB models instead, sfermion masses arise at a lower energy  $\Lambda$ , much below the scale at which flavour symmetry is expected to be valid. Thus the SM Yukawa couplings are already present when the mass generation takes place, and FCNC are then automatically suppressed. Also, the trilinear couplings  $A_f$  are negligible at the  $M_m$  scale, since they are generated at two loops and are further reduced by a factor  $\alpha_i/4\pi$ . They will be in any case very small at the electroweak scale and are not considered as a relevant parameter.

Another important characteristic of these models is the gravitino mass. Since soft masses are proportional to the coupling constants, the LSP will be the gravitino, the least interacting sparticle. By reducing the energy scale at which soft mass terms are generated from  $M_P$  to  $M_m$ , the ‘effective’ SUSY breaking scale (in the messenger sector)  $\sqrt{F_m}$  is now much lower. The messenger mass could be  $\sim 100 \text{ TeV}/c^2$ , thus to produce MSSM particles with the right mass ( $m \sim F_m/M_m \sim 100 \text{ GeV}/c^2$ ),  $\sqrt{F_m}$  can be as low as  $10^4 \text{ GeV}/c^2$ . From this ‘effective’ SUSY breaking scale the gravitino mass is derived now as [29]:

$$m_{\tilde{G}} = \frac{F_m}{k\sqrt{3}M_P} = \frac{2.4}{k} \left( \frac{\sqrt{F_m}}{100 \text{ TeV}} \right)^2 \text{ eV}/c^2 \quad (1.19)$$

where  $F_m = kF_0$  and  $k$  is a model dependent parameter describing how SUSY breaking is communicated from the hidden sector to the messenger sector.

If the gravitino is the LSP all MSSM particles will eventually decay into it, and since it couples gravitationally one would naively expect those decays to be extremely slow. But the gravitino contains two longitudinal components from the goldstino it absorbed by means of the super-Higgs mechanism. And these components with helicity  $\pm\frac{1}{2}$  and gauge couplings may lead to decay rates high enough to be of experimental importance.

Finally, to completely specify the MSSM spectrum and its phenomenology, it is only necessary to use six parameters:  $M_m$ ,  $m_{\tilde{G}}$ ,  $\Lambda$ ,  $N_5$ ,  $\tan\beta$  and  $\text{sign}(\mu)$ . Hence, GMSB models are highly predictive as will be discussed in Chapter 5.

## 1.5 Collider signatures

The best probe for supersymmetry is naturally direct production of superpartners at high energy colliders. Figure 1.6 shows the Feynman diagrams for the production of all relevant SUSY particles at LEP, where electrons and positrons collide head-on.

In Gauge Mediated SUSY Breaking models, experimental signatures differ significantly from models with a neutralino LSP. If R-parity is conserved, as is assumed throughout this work, all SUSY decay reactions will terminate in the next-to-lightest supersymmetric particle (or NLSP) decaying to its SM partner and the gravitino LSP. The identity of the NLSP, therefore, is central to the phenomenology. Furthermore, the NLSP may be long lived and thus very striking signatures are possible. The NLSP decay length is controlled by the SUSY

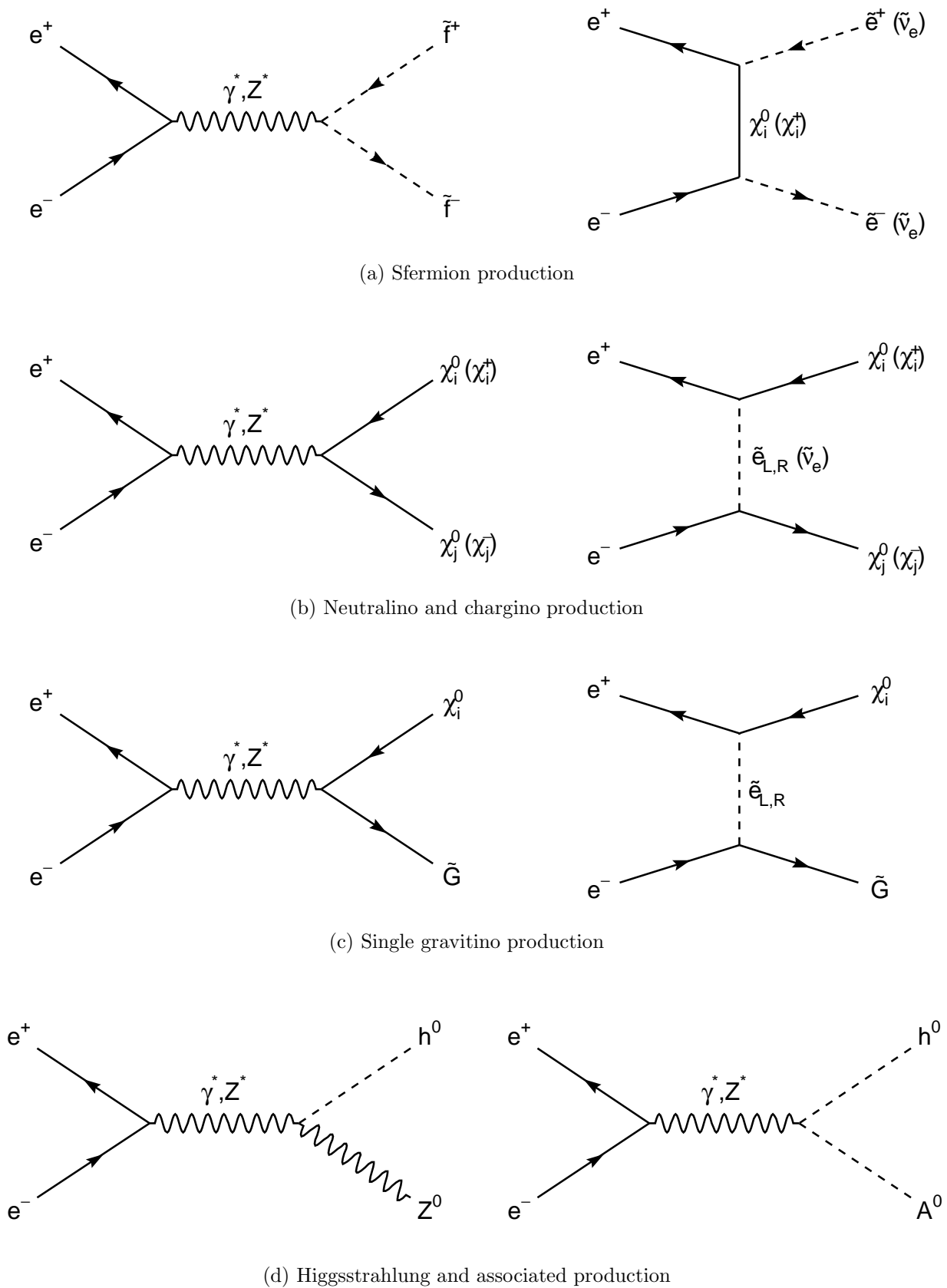
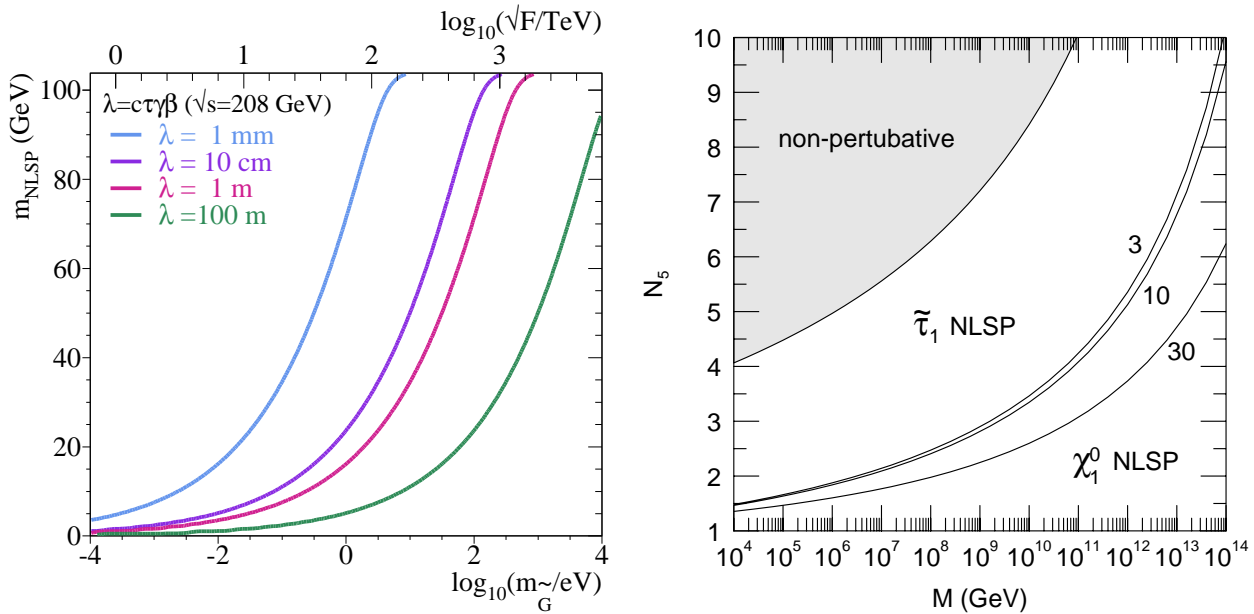


Figure 1.6: Production of SUSY particles and MSSM Higgs neutral bosons at LEP when R-parity is conserved.



(a) Contours of the NLSP decay length (Eq. 1.20 with  $\kappa_\gamma = 1$ ) as a function of the NLSP mass and the gravitino mass, for pair-produced particles at  $E = 104$  GeV.

(b) Domains of stau NLSP and lightest neutralino NLSP as a function of the number of messenger families and the messenger mass. The solid lines represent different values of  $\tan \beta = 3, 10, 30$ . From Ref. [31]

Figure 1.7: The NLSP nature as a function of parameters.

breaking scale or equivalently (Eq. 1.13) by the gravitino mass:

$$\lambda_{\text{NLSP}} = c\tau_{\text{NLSP}}\gamma\beta = \frac{0.01}{\kappa_\gamma} \left( \frac{100 \text{ GeV}/c^2}{m_{\text{NLSP}}} \right)^{-5} \left( \frac{m_{\tilde{G}}}{2.4 \text{ eV}/c^2} \right)^2 \sqrt{\frac{E^2}{m_{\text{NLSP}}^2} - 1} \text{ cm} \quad (1.20)$$

where  $\kappa_\gamma$  is the photino component of the neutralino NLSP, or one in all other cases (see Fig. 1.7a). If  $m_{\tilde{G}}$  is large enough and the NLSP decay length is measured as a vertex displacement, it provides a unique method to probe the value of  $\sqrt{F_0}$ , the scale of SUSY breaking, as opposed to other measurements which in general are only sensitive to  $\Lambda$ . Searches for NLSP's decaying in the middle of the detector also benefit from lower background rates, hence the interest in studying these signatures.

As regards the NLSP type, depending on the GMSB parameters it will generally be either the neutralino or the lightest stau (see Fig. 1.7b. This can be deduced from Eqs. 1.17 and 1.18 where sparticles with only  $U(1)_Y$  interactions will be lighter than the rest since  $\alpha_1 < \alpha_2 \ll \alpha_3$ . The tiny selectron and smuon mixing factors (Eq. 1.10) allows one to generally treat them as degenerate, unmixed mass eigenstates, thus  $m_{\tilde{e}} = m_{\tilde{\mu}}$  will be assumed for the rest of this work. In some cases, specially for low  $\tan \beta$ , the three right handed sleptons are degenerate in mass and act as co-NLSP. Also possible in a much more restricted corner of parameter space is the neutralino-stau co-NLSP where the mass difference between the neutralino and the sleptons is less than the tau mass. Table 1.4 lists the conditions in the mass hierarchy for each type of NLSP scenario and its decay [32]. A neutralino NLSP will predominantly decay to  $\gamma\tilde{G}$  and not  $Z\tilde{G}$  for  $m_\chi \lesssim 100 \text{ GeV}/c^2$  [33]. From now on, references to the slepton NLSP case or

Case	Condition	Final decay
neutralino NLSP	$m_\chi < m_{\tilde{\tau}_1} - m_\tau$	$\chi \rightarrow \gamma \tilde{G}$
stau NLSP	$m_{\tilde{\tau}_1} < \min(m_\chi, m_{\tilde{l}_R}) - m_\tau$	$\tilde{\tau}_1 \rightarrow \tau \tilde{G}$
slepton co-NLSP	$m_{\tilde{l}_R} < \min(m_\chi, m_{\tilde{\tau}_1} + m_\tau)$	$\tilde{l}_R \rightarrow l \tilde{G}; \tilde{\tau}_1 \rightarrow \tau \tilde{G}$
neutralino-stau co-NLSP	$ m_{\tilde{\tau}_1} - m_\chi  < m_\tau; m_\chi < m_{\tilde{l}_R}$	$\chi \rightarrow \gamma \tilde{G}; \tilde{\tau}_1 \rightarrow \tau \tilde{G}$

Table 1.4: The four possible NLSP scenarios, with the corresponding NLSP decay, neglecting the electron and muon masses.

scenario, should be understood as corresponding to the stau NLSP region, including also the more restricted case of sleptons as co-NLSP.

The superpartner mass spectrum in GMSB models will ultimately determine which SUSY particles can be produced at LEP and their subsequent decay chains. The strongly interacting states, including the generally lighter stops, are usually too heavy to be produced at LEP. Only the lightest neutralino  $\chi_1^0$ , slepton  $\tilde{\ell}_R^\pm$  or Higgs  $h^0$  will in general be accessible at LEP2. The charginos, heavier neutralinos and left-handed sleptons are too heavy to be relevant to discovery at these energies<sup>2</sup>. A typical mass spectrum of GMSB models is shown in Figure 1.8.

In the following, the lightest neutralino  $\chi_1^0$  will be abbreviated to  $\chi$  and referred to as ‘the’ neutralino, when no other heavier neutralino or chargino is present. The symbol  $\ell$  will stand for the three charged leptons,  $e$ ,  $\mu$  or  $\tau$ ; and  $l$  will only refer to the electron or muon.

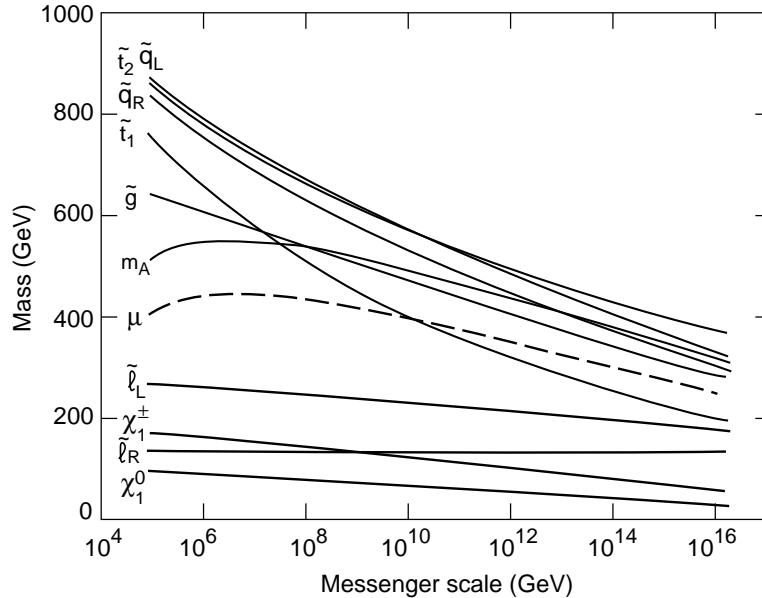


Figure 1.8: Sparticle masses dependence with  $M_m$  in a GMSB model with  $N_5 = 1$ ,  $\tan \beta = 3$  and a messenger scale bino mass of  $115 \text{ GeV}/c^2$ . From Ref. [33].

<sup>2</sup> Even if no other SUSY particle is accessible at LEP, direct production of gravitinos is still possible. The cross section for  $e^+e^- \rightarrow \tilde{G}\tilde{G}\gamma$  scales with  $1/m_{\tilde{G}}^4$ , so only ultra light gravitinos could be observed through direct production. ALEPH has searched for this process and derives an upper limit on the gravitino mass of  $1.3 \times 10^{-5} \text{ eV}/c^2$  [34].



# Chapter 2

## Experimental Overview

The Large Electron Positron collider (LEP) started operation in 1989 and ended in the fall of 2000. The largest accelerator of its kind in the world, it was built to study in detail the Z and W massive vector bosons. From 1989 to 1995 it ran with a centre-of-mass energy ( $\sqrt{s}$ ) close to the Z mass, scanning the electroweak sector and the properties of the Z particle. This phase is known as LEP1. From 1996 onwards, LEP increased in energy through the 161 GeV threshold, for the W boson pair-production, and reached 209 GeV in 2000. This phase, referred to as LEP2, continued the precision measurements, enlarging our understanding of the Standard Model, probing the theory to a high level of accuracy.

The LEP programme has thus set a milestone in the experimental determination of the parameters of the SM and has confirmed the theoretical predictions with extremely high precision. Once the detectors and the accelerator have been dismantled, the LEP tunnel will house the Large Hadron Collider (LHC), a proton-proton accelerator with  $\sqrt{s} = 14$  TeV, which is expected to begin operation in 2007. This chapter describes briefly the LEP collider and, in more detail, the ALEPH detector and its performance.

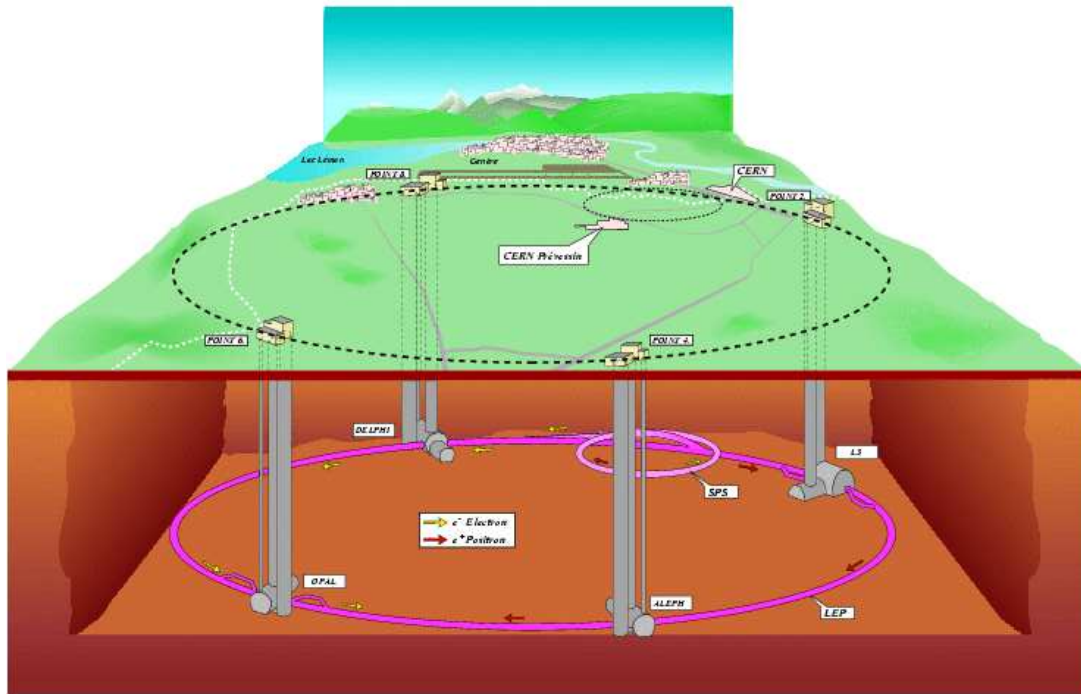


Figure 2.1: An overview of the LEP accelerator. From Ref. [37].

## 2.1 The LEP collider

The Large Electron Positron collider (LEP) lay between 100 and 150 m underground on the Swiss-French border, near Geneva. It was a 26.7 km long storage ring designed to accelerate electrons and positrons and produce collisions at four points where general-purpose detectors were placed to observe and record the resulting new particles. These detectors were ALEPH, DELPHI, OPAL and L3. Figure 2.1 shows the LEP accelerator complex along with the detectors. For a detailed description of LEP see Refs. [35, 36], here only an overview is given.

Beams of counter-rotating electrons and positrons were injected into LEP at an energy of 22 GeV from the Super Proton Synchrotron (SPS). Once the particles were in the highly evacuated beam-pipe, they were accelerated by superconducting NbTi radio frequency (RF) cavities and normal Cu cavities operating at a frequency of 352 MHz. To maintain a circular orbit, the beams were bent by 3368 dipole magnets and focused by 816 quadrupole and sextupole magnets. When particles follow a circular trajectory, they lose some of their energy by emitting synchrotron radiation. Since this effect is inversely proportional to the square of the accelerator radius, it is necessary to build very large accelerators. Hence the large radius of LEP helped to minimise the amount of energy that cavities had to give back to the particles to attain the nominal  $\sqrt{s}$ .

The normal mode of operation consisted of four equally spaced *bunches* of electrons and positrons which crossed each other every  $89 \mu\text{s}$  (the collision frequency was thus  $f \sim 11 \text{ kHz}$ ). With approximately  $10^{11}$  particles per bunch, typical total beam current values were 6 mA, or  $750 \mu\text{A}$  per bunch. At the interaction points (IPs), where collisions are produced and the dimensions of the bunches have to be as small as possible to enhance the collision rate, each bunch was approximately 1 cm long,  $200 \mu\text{m}$  wide horizontally ( $\delta_x$ ) and  $8 \mu\text{m}$  vertically ( $\delta_y$ ). This yielded a typical LEP2 *instantaneous luminosity* of  $10^{31} \text{ cm}^{-2} \text{ s}^{-1}$ . The instantaneous

luminosity parameter contains all the accelerator capabilities and is proportional to the rate of interactions (collisions). It is defined as:

$$\mathcal{L} = \frac{N_{\text{bunch}} N_{e^+} N_{e^-} f}{4\pi\delta_x\delta_y} \quad (2.1)$$

where  $N_{\text{bunch}}$  is the number of bunches and  $N_{e^\pm}$  is the number of electrons/positrons per bunch. The luminosity was measured independently by LEP and the four experiments with dedicated subdetectors.

## 2.2 The ALEPH detector

The ALEPH (Apparatus for LEp PHysics) detector was designed to cover as much solid angle as possible around the point where the beams were made to collide, with high granularity and hermeticity. This is to ensure that all particles emerging from the  $e^+e^-$  collisions are measured and identified. In practice, a coverage of  $\sim 3.9$ sr was achieved, allowing the detailed study of Standard Model physics at LEP and searches for new physics. Its shape was cylindrical, built around the interaction point, with 12 m in diameter and 12 m in length, weighing over 3000 tons and having some 700 000 readout channels.

Particles originating at the IP and traveling outwards traversed through several subdetectors arranged in cylindrical layers. They first passed through a series of three low-density tracking devices, designed to measure the trajectory of charged particles, and then encountered high-density calorimeters where all but muons and neutrinos were completely stopped depositing all their energy. Only muons could penetrate to the last subdetector, the muon chambers, being therefore tagged as such. The tracking subdetectors were immersed in a highly uniform 1.5 T magnetic field created by a 6.4 m long and 5.3 m diameter superconducting solenoid. The trajectories of charged particles are curved in the strong magnetic field, describing a helix which spirals around the beam axis. This curvature provides a measurement of their momentum.

Figure 2.2 shows all the subdetectors forming the ALEPH detector. Moving radially away from the beam-pipe, there is the Microvertex Detector (VDET), the Inner Tracking Chamber (ITC) and the Time Projection Chamber forming the tracking volume of the detector. They are followed by the Electromagnetic Calorimeter (ECAL) and then the magnet so as not to degrade the ECAL energy resolution. The iron return yoke for the magnet was segmented into layers and instrumented with streamer tubes acting as a Hadron Calorimeter (HCAL). Finally, surrounding the HCAL, two additional double layers of streamer tubes formed the muon chambers. Another three pairs of detectors LCAL, SiCAL and BCAL provided low angle coverage and measured Bhabha scattered electrons and positrons. They were located very close to the beam-pipe, BCAL giving measurements of instantaneous luminosity from outside the detector, while LCAL and SiCAL measured integrated luminosity. The ALEPH detector is described in Refs. [39, 40, 41] and its performance is described in Ref. [42].

The coordinate system is defined as follows: the origin is the geometrical centre of the detector, also the nominal IP; the  $x$ -axis is horizontal and points to the centre of the LEP ring; the  $z$ -axis is along the electron beam direction and makes an angle of 3.59 mrad upwards with the local horizontal; the  $y$ -axis then makes an angle of 3.59 mrad with the local vertical. This small displacement with respect to the local vertical is due to the fact that the LEP tunnel was tilted by 1.4% for geological reasons. Given the detector and event geometry, it is often

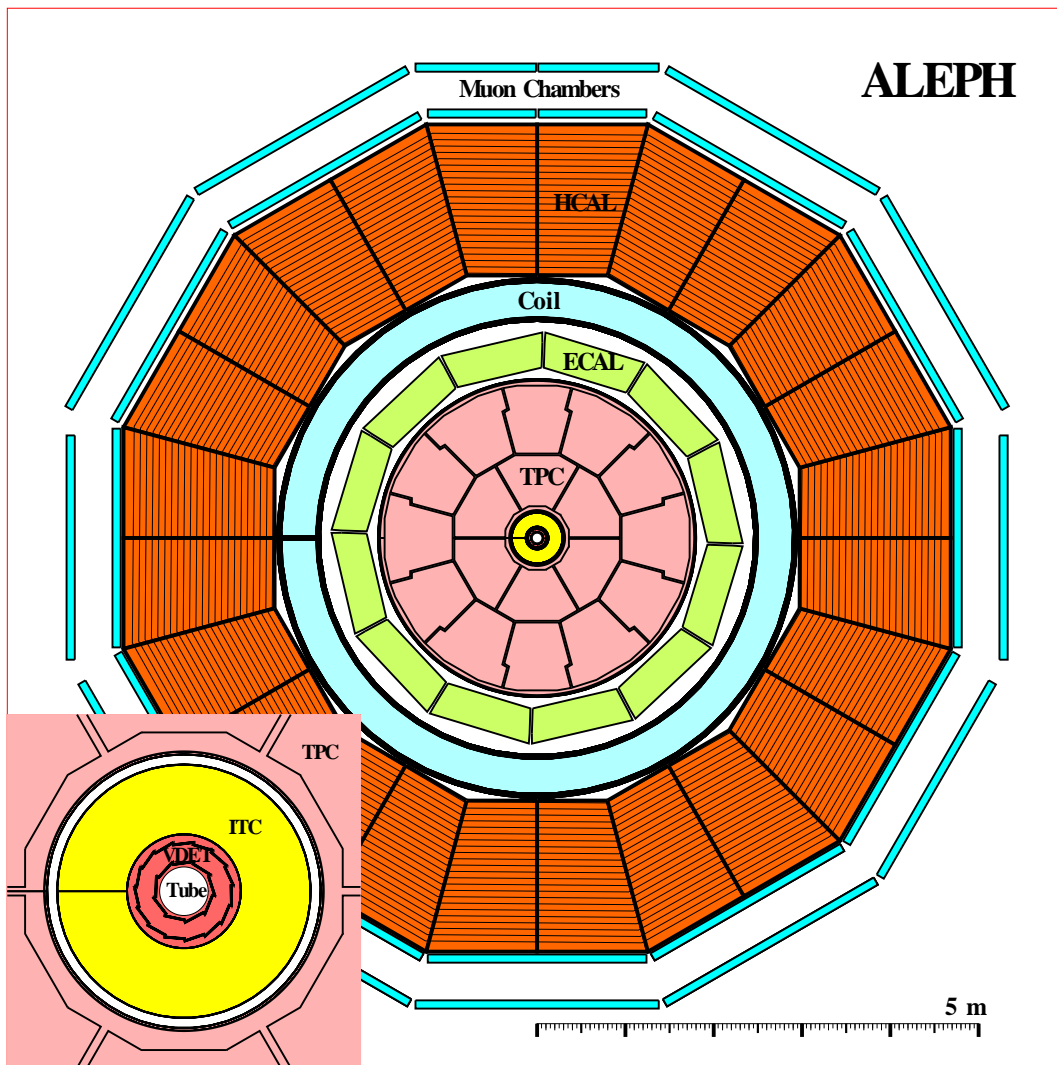


Figure 2.2: End-on view of the ALEPH detector showing all its subdetectors [38].

more useful to use spherical  $(r, \theta, \phi)$  or cylindrical coordinates  $(\rho, \phi, z)$ , defined as:

$$\begin{aligned}
 x &= r \sin \theta \cos \phi = \rho \cos \phi \\
 y &= r \sin \theta \sin \phi = \rho \sin \phi \\
 z &= r \cos \theta = z
 \end{aligned}
 \tag{2.2}$$

where the polar angle  $\theta$  is measured with respect to the  $+z$ -axis and extends between 0 and  $\pi$ . The azimuthal angle  $\phi$  is measured in the  $(x, y)$  plane starting at the  $x$ -axis. The coordinate system is depicted in Fig. 2.3.

## 2.3 Charged Particle Tracking

### 2.3.1 Vertex Detector

The Vertex Detector (VDET) [43] was the innermost subdetector of ALEPH. It was very close to the IP to provide highly accurate measurements of charged particles' trajectories. It specially served to identify very short-lived particles, such as  $B$ -mesons, made of  $b$ -quarks,

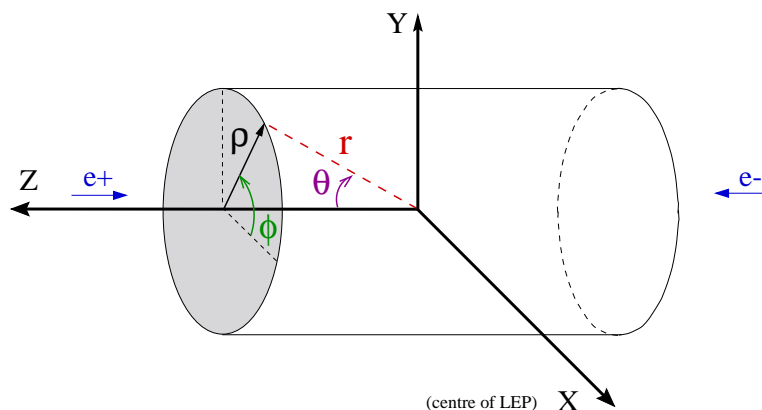


Figure 2.3: The ALEPH coordinate system.

which travel a very small distance before decaying (typically  $\sim 400 \mu\text{m}$ ). Its principal aim was to determine whether a particle came from the IP or rather originated from a displaced vertex. It was upgraded in 1995 to prepare for LEP2. With respect to the original VDET, it had improved radiation hardness, covered a wider angle and introduced less passive material. The main physics purpose of the upgrade was to improve the efficiency of  $b$ -tagging. At LEP2 energies, the Higgs boson is expected to decay mainly to  $b$ -quarks ( $\text{BR}(H \rightarrow b\bar{b}) > 70\%$ ), hence  $b$ -tagging is crucial in Higgs boson searches.

The final VDET consisted of two approximately cylindrical layers. The inner layer, resting on the beam-pipe at 6.3 cm from the beam, was made of 9 ‘faces’, each face measuring 40 cm in length along the  $z$ -axis and formed by six double-sided silicon microstrip detectors, or ‘wafers’. The outer layer, at 11.0 cm from the beam, had 15 faces and ensured a maximal lever-arm between the beam-pipe and the Inner Tracking Chamber. Figure 2.4 shows a full view of the VDET and the geometry of the faces from an end-on view.

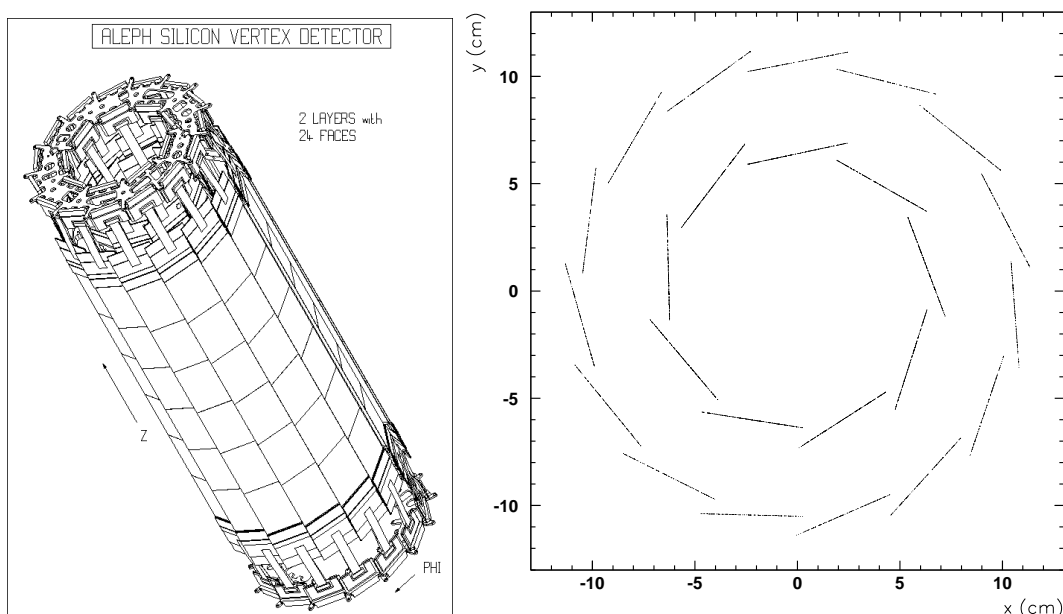


Figure 2.4: Left, full view of VDET. Right, end view showing the position of the faces [41].

The two sides of each wafer had readout strips arranged orthogonally to each other. When a charged particle passed through the wafer, a VDET hit was formed giving a two dimensional measurement: the  $r\phi$  side provided a  $\phi$  measurement while the  $z$  side recorded  $z$ . The readout pitch on the  $r\phi$  side was  $50\ \mu\text{m}$  and  $100\ \mu\text{m}$  on  $z$ . However, the spatial resolution was improved by using the signal recorded on several strips to determine the position of each hit down to  $10\ \mu\text{m}$  in  $r\phi$  and  $15\ \mu\text{m}$  in  $z$ . This precision allowed very precise measurements of particle lifetimes, as short as 300 fs. The angular acceptance was such that a particle with  $|\cos\theta| < 0.95$  hit at least one layer of the VDET.

### 2.3.2 Inner Tracking Chamber

The ITC [44] was a 2 m long cylindrical multiwire drift chamber. There were eight concentric layers of wires running parallel to the beam ( $z$ ) direction. Its inner radius was  $r = 16\ \text{cm}$ , where it supported the outer layer of the VDET, and its outer radius extended to  $r = 26\ \text{cm}$ . Its full volume was filled with a mixture of argon (80%) and carbon dioxide (20%) at atmospheric pressure. Each of the 960 sense wires, arranged in eight layers, was held at a positive potential of  $\sim 2\ \text{kV}$  and was surrounded by five field wires and a calibration wire all held at ground potential. This formed an hexagonal ‘drift cell’. The cell structure is shown in Fig. 2.5.

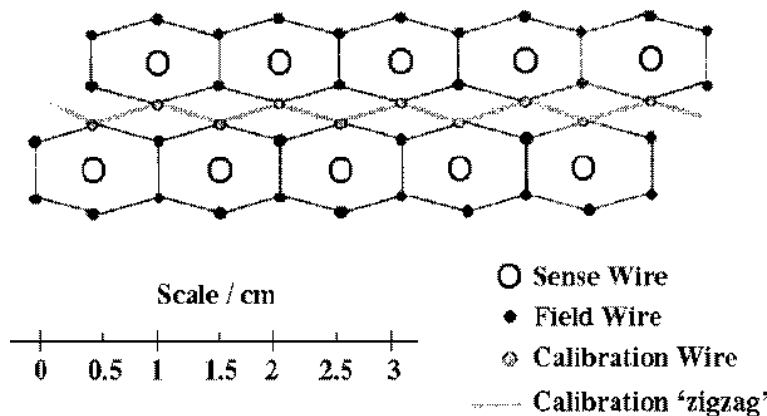


Figure 2.5: Drift cell geometry of the ITC [40].

When a charged particle traversed an ITC cell it ionised the gas and produced electrons which were attracted to the sense wires. The ionisation charge drifted to the sense wire with an average velocity across the cell of  $50\ \mu\text{m}/\text{ns}$ . This negative current pulse was detected at both ends of the sense wire. The  $z$  coordinate was thus obtained by the difference in arrival time of the signal at each end. The  $r\phi$  coordinate was deduced by converting the drift time into a drift distance using a parametrisation of the non-linear relationship between the two. The spatial resolution was around  $150\ \mu\text{m}$  in the  $r\phi$  coordinate and only 5 cm in the  $z$  coordinate. Each wire could only produce one hit per event, and therefore there were a maximum of eight hits per track.

The drift cells were small so that they could provide information extremely quickly: the cell size determines the maximum drift time. This was achieved at the cost of having many wires, readout channels and the consequent problem of fitting more electronics. But then, the ITC was able to provide the only tracking information for the first-level trigger (see Sec. 2.5) in less than  $3\ \mu\text{s}$  after a beam crossing.

### 2.3.3 Time Projection Chamber

The Time Projection Chamber (TPC) [45] was the main tracking detector in ALEPH providing three-dimensional points for track reconstruction. It was a 4.4 m long cylindrical drift chamber with its axis parallel to the beam, an inner radius of 31 cm and an outer radius of 180 cm. There were three main components: the field cage, made up by two cylinders (inner and outer), two circular end-plates, and eight ‘feet’ which supported the TPC weight, attaching it to the magnet. A diagram of the TPC is shown in Fig. 2.6.

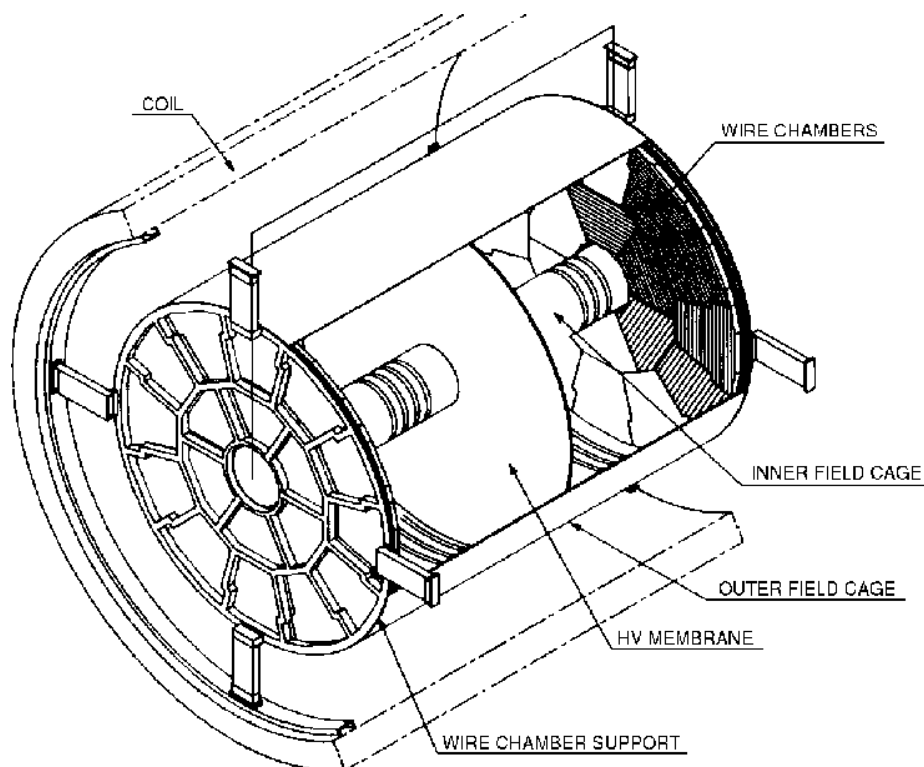


Figure 2.6: TPC overall view. From Ref. [40].

The chamber was divided into two halves by a central membrane kept at high potential ( $-27$  kV). This membrane, along with the cathode planes of the end-caps (held at a potential near ground) and the inner and outer field cages, produced a uniform electric field in the  $\pm z$  direction. The passage of a charged particle ionised the gas ( $\text{ArCH}_4$ ) and the electron cloud drifted towards the nearest end-cap following the  $11$  kV/m electric field. The parallel magnetic field within the tracking volume ensured that drift electrons did not diffuse radially and had tight helix trajectories (the clouds were contained in the  $r\phi$  plane).

The TPC end-plates were formed by three consecutive wire grids. See Fig. 2.7 for a diagram of an end-plate edge. The first one was the *gating grid* which will be discussed shortly. Next was the *cathode grid*, which was grounded and was responsible for the drift of the ionisation cloud. And finally, electrons were collected on the *sense grid*. It consisted of alternating sense wires, held at ground potential, and field wires, held at a high positive potential, which formed conventional proportional multiwire chambers with cathode ‘pads’ to read out the pulses. There were 21 rows of cathode pads precisely positioned behind the wires and capacitively coupled to them. Hence the  $z$  coordinate was calculated from the arrival time of the signal on the pad and the known drift velocity of electrons in the drift volume. The drift velocity

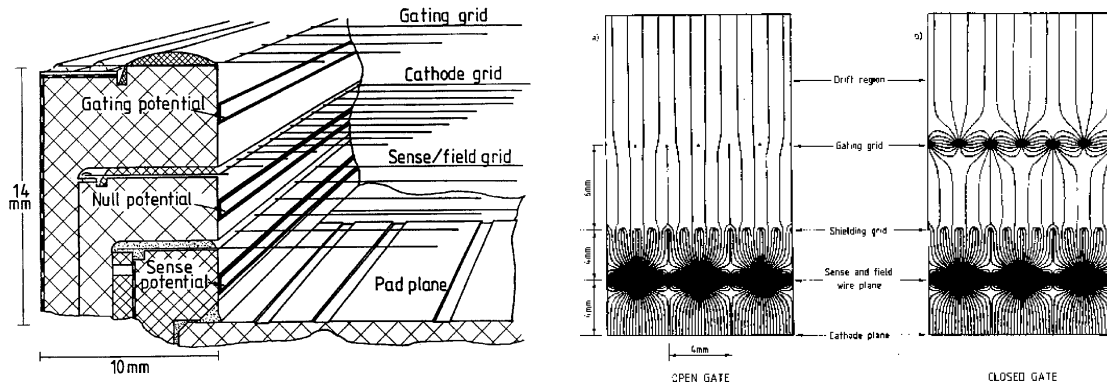


Figure 2.7: Schematic view of a TPC sector edge (left) showing wire grids, pad plane and potential strips. On the right, the gating grid of the TPC showing electric field lines in the (a) open and (b) close gate states. From Ref. [40].

was constantly measured by laser calibration. The  $r$  and  $\phi$  coordinates were obtained from the position of the pads involved in the measurement. Hits could overlap in  $r\phi$ , e.g. if two particles ionised the same  $r\phi$  region at different  $z$ , producing two pulses in the same pad. The pad recognised the different pulses by their different time profile allowing separation of the hits. Thus the TPC could measure up to 21 three-dimensional points for a track at polar angle  $\theta$  of  $90^\circ$  with a resolution of  $180\ \mu\text{m}$  in  $r\phi$  and  $800\ \mu\text{m}$  in  $z$ . The average resolution decreased with particle momentum and  $\theta$ . Events with low momentum and low polar angle, like two-photon processes, have the worst resolution.

If an ionisation avalanche was produced close to the sense wires, positive ions could drift back to the main TPC volume and distort the local electric field leading to track distortion. The *gating grid* in the end-caps was used to prevent charge build-up in the drift volume of the TPC. It was thus located between the drift volume and the cathode wires so that if the gating grid was in the ‘closed’ state, positive ions did not enter the drift volume. In the ‘open’ state, a negative potential was applied to the gating wires and the gate was transparent to the passage of drifting charged particles. In the closed state, alternate gate wires were kept at positive and negative potentials creating dipole fields which prevented the passage of charged particles. See Fig. 2.7 for a diagram of the gate electrostatic configuration in both open and closed states. The gate was open  $2\ \mu\text{s}$  before a beam-crossing and stayed open for  $45\ \mu\text{s}$  if the Level-1 trigger reached a ‘yes’ decision (Sec. 2.5). This allowed the ionisation electrons to be collected. A negative decision from the Level-1 trigger closed the gate until the next beam-crossing.

Furthermore, the TPC wires were also used to measure the specific ionisation of charged tracks since the pulse height on the sense wires is proportional to the specific ionisation energy loss ( $dE/dx$ ). The coordinates  $(r, \phi, z)$  along a particle trajectory provide a measurement of its momentum. The  $dE/dx$  for each particle depends only on its velocity in a certain material, so by combining the  $dE/dx$  and the momentum measurements the mass of the particle can be inferred and thus its identity derived. There were a total of 338 possible measurements of  $dE/dx$  for tracks within the angular acceptance of the TPC. A typical resolution of 7.2% was achieved in hadronic events. Not all tracks had  $dE/dx$  information since a minimum of 50 wire samples were required to obtain a reasonably accurate measurement. Thus particles with polar angles near 0 or  $\pi$  did not have identification information from the TPC. Figure 2.8 shows how the  $dE/dx$  information from the TPC is used to obtain particle identification.



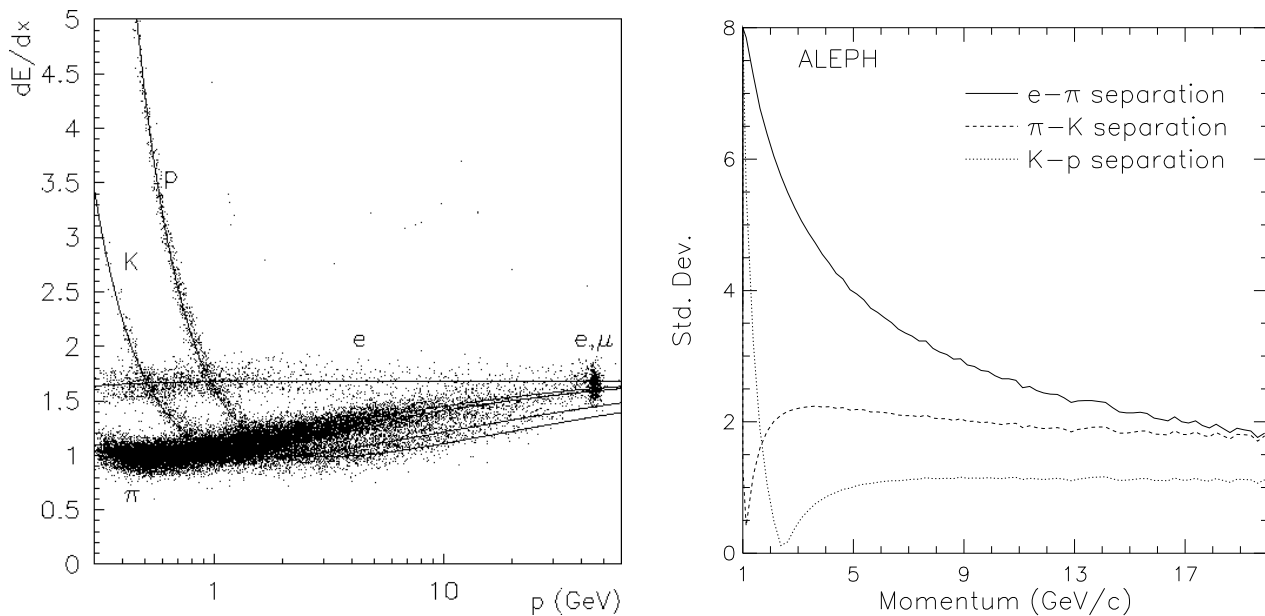


Figure 2.8: On the left, the measured  $dE/dx$  as a function of particle momentum for a sample of about 40 000 tracks. Lines are the fitted parametrisation to a modified Bethe-Bloch formula for electrons, muons, pions, kaons and protons. On the right, the average separation in standard deviations between different particle types as a function of momentum. It has been computed using all tracks in hadronic Z decays which have at least 50  $dE/dx$  measurements. From Ref. [42].

## 2.4 Calorimetry and Luminosity Monitors

### 2.4.1 Electromagnetic Calorimeter

The main purpose of the Electromagnetic Calorimeter (ECAL) [40] was to measure the energy of photons, electrons and positrons in an event. The ECAL covered polar angles of  $|\cos\theta| < 0.98$  and was capable of measuring tracks throughout the polar angle range of the TPC. It was inside the superconducting solenoid to avoid a degradation of its performance resulting from particles decaying in the uninstrumented coil.

The ECAL was composed of a 4.7 m long barrel and two end-caps, all with similar properties. The calorimeter consisted of 45 layers of lead with a proportional wire chamber in between each layer. The signals from the wire chambers were read out by cathode planes arranged into towers pointing to the interaction point. There were more than 73 000 such towers, each subdivided into three ‘storeys’ which each yielded an energy measurement.

An incoming electron, positron or photon interacted in one of the 2 mm lead sheets and generated an electromagnetic shower by *bremsstrahlung* in the case of electrons and by  $e^+e^-$  pair-production in the case of photons. When the particles from the shower traversed the wire chambers, they ionised the gas and the cathode pads collected the pulses from the wires. This allowed a position measurement of the shower development to be made from the readout of the cathode pads. The information from the wires with their faster readout was used to make a trigger decision. The choice of lead as absorber was due to its short radiation length ( $X_0 = 6.4 \text{ g/cm}^2$  [5]). The total thickness of lead was about  $22X_0$ , or  $\sim 40 \text{ cm}$ , which ensured that over 98% of the energy of a 50 GeV electron was contained in the lead sheets. Hadrons

and muons traversed the ECAL and could deposit some energy inside it since it was about one interaction length thick.

The large number of towers provided high granularity which was needed for spatial separation of the electromagnetic showers and helped to improve particle identification. Since each tower gave three energy measurements, the shower profile could also be studied, adding more information to discriminate between electromagnetic and hadronic showers. An ECAL layer is illustrated in Fig. 2.9.

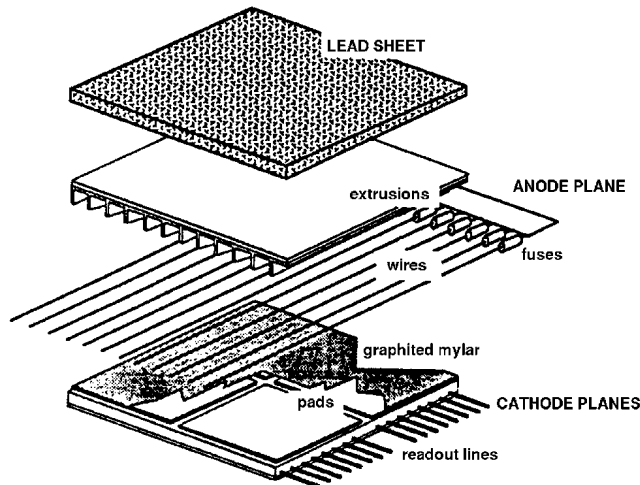


Figure 2.9: Detail of an ECAL layer. There are 45 such layers [40].

The ECAL had an angular resolution of [42]:

$$\sigma_\phi = \frac{\sigma_\theta}{\sin \theta} = 0.25 + \frac{2.5}{\sqrt{E(\text{GeV})}} \text{ mrad} \quad (2.3)$$

and the energy resolution was parametrised using Bhabha scattered electrons as:

$$\frac{\sigma_E}{E} = 0.009 + \frac{0.18}{\sqrt{E(\text{GeV})}} \quad (2.4)$$

The end-caps met the barrel at polar angles of  $\sim 40^\circ$ . There were a number of cables in this region which reduced the total depth in radiation lengths. The energy resolution was degraded by around 30% in this region as a result.

### 2.4.2 Hadron Calorimeter

The Hadronic Calorimeter (HCAL) [40] was used to finally stop and measure the energy of hadrons as well as tag the trajectories of muons. Its structure was very similar to that of the ECAL, comprised of a barrel and two end-caps. However, it was slightly rotated with respect to the ECAL to avoid an overlap between the inactive ‘cracks’ of both detectors. This can be seen in Fig. 2.10, which offers a view of both ECAL and HCAL.

The HCAL was made of 23 iron layers separated by plastic streamer tubes. It weighed in excess of 2500 tons and particles at normal incidence encountered 1.2 m of iron, equivalent to

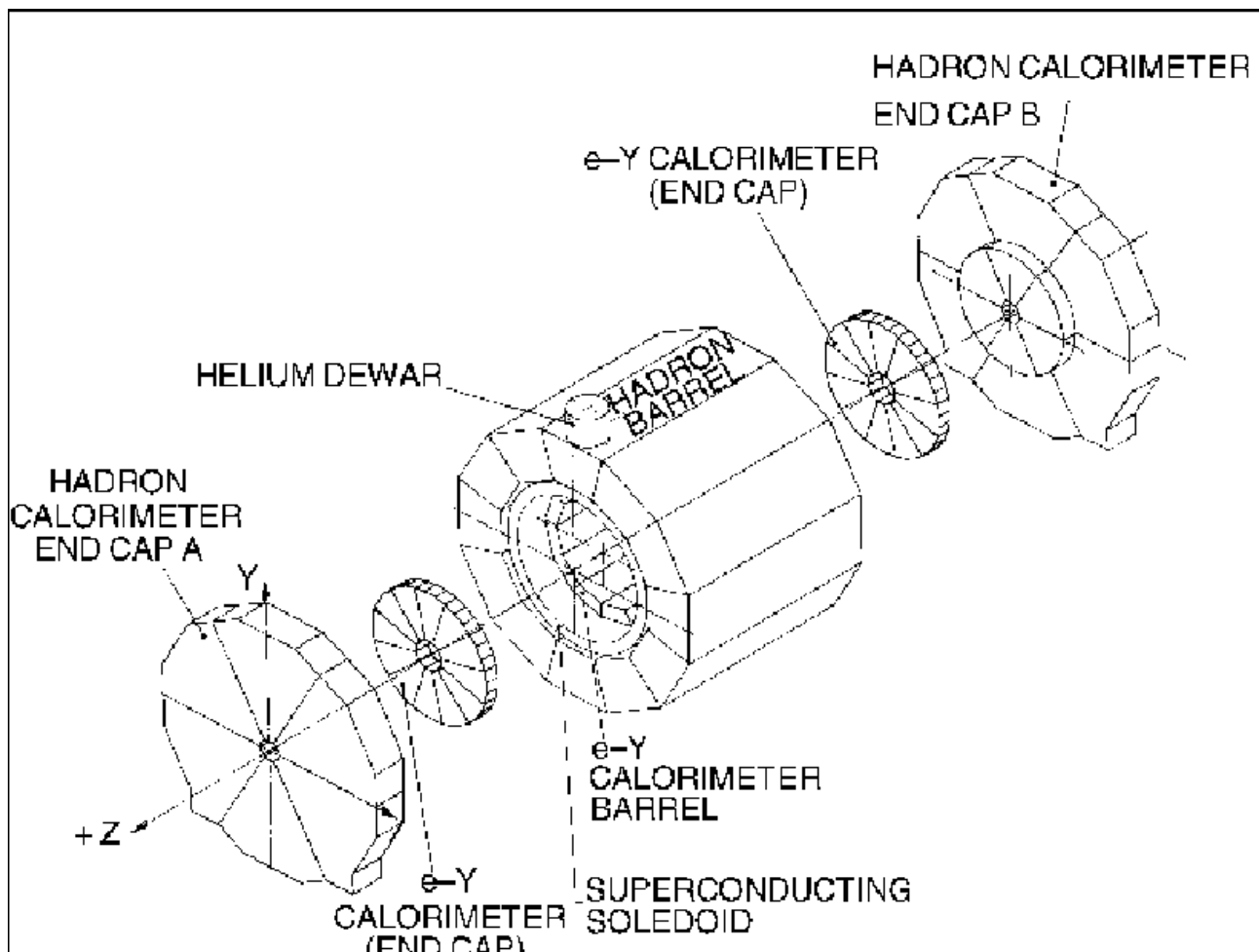


Figure 2.10: The ALEPH calorimeters. The HCAL end-caps measure about 9 m in diameter [40].

7.2 interaction lengths for hadrons. The iron acted as the return yoke of the magnetic flux from the solenoid and also as the main mechanical support for the ALEPH detector.

A hadron reaching the iron layers interacted through the strong force with the nucleons of iron and decayed into a shower of low energy particles. Hadronic showers are broader and deeper than electromagnetic showers which explains why the HCAL needed to be thicker than the ECAL. The ionisation caused by the shower in the tubes was collected by cathode pads which were grouped into 4068 projective towers pointing to the IP, like the ECAL. The pad electrodes gave a measurement of the integrated energy from each tower, but did not provide any information on the  $r$  coordinate, the depth of the shower, which is very important to determine the hadronic shower profile. A digitised cathode strip running along each streamer tube provided the necessary  $r\phi$  measurements by indicating which plane of the HCAL had recorded a hit. This enabled a better discrimination between muons and hadrons by their different hit pattern (see Sec. 2.6.3).

For pions at normal incidence the energy resolution is parametrised by [42]:

$$\frac{\sigma_E}{E} = \frac{0.85}{\sqrt{E(\text{GeV})}} \quad (2.5)$$

### 2.4.3 Muon Chambers

Muons traversed both calorimeters with a characteristic trail of hits with no shower development. Surrounding the HCAL there were two further double-layers of streamer tubes known as muon chambers. Only muons could penetrate that far after the HCAL and these chambers acted as a muon tracking detector. The two layers were separated by more than 40 cm to enable a measurement of the track angle with an accuracy of  $\sim 15$  mrad.

### 2.4.4 Luminosity Monitors

The luminosity delivered by LEP was determined by using three pairs of specific detectors. An accurate measurement of the luminosity  $\mathcal{L}$  is necessary in order to obtain precise reaction cross sections from the event count rates. Cross sections, giving the probability of an interaction to occur, are usually given in *barns*, defined as  $1 \text{ b} = 10^{-28} \text{ m}^{-2}$ .

These detectors measured the number of small angle Bhabha events, coming from the QED process  $e^+e^- \rightarrow \gamma^* \rightarrow e^+e^-$ , whose cross section is known very accurately, to calculate the luminosity<sup>1</sup>.

For  $N$  events and cross section  $\sigma$ :

$$\int \mathcal{L} dt = \frac{N}{\sigma} \quad \text{with} \quad \sigma = \frac{1040}{s} \left( \frac{1}{\theta_{\min}^2} - \frac{1}{\theta_{\max}^2} \right) \text{ nb} \quad (2.6)$$

where  $s$  in GeV is the centre-of-mass energy and  $\theta_{\min/\max}$  are the angular bounds which define the acceptance cone subtended by the monitors.

Each luminosity monitor consisted of two units on either side of the interaction point to detect the outgoing back-to-back  $e^-$  and  $e^+$ . LCAL and SiCAL were inside ALEPH itself, both at about 2.5 m away from the IP. BCAL, with 12 layers of tungsten and scintillator counters, was about 7 m away, outside ALEPH.

SiCAL had 12 annular tungsten-sheets sandwiched between silicon detectors. The active region covers polar angles from 24 to 58 mrad. LCAL was similar in construction to the ECAL —lead sheets interspersed with multiwire proportional chambers—, covering angles just beyond SiCAL, from 45 to 190 mrad. LCAL can be thought of as a low angle extension of the ECAL. LCAL and SiCAL had low event rates so they provided an integrated luminosity measurement. However, for LEP2, additional background shielding was required close to the beam-pipe which reduced the angular acceptance of SiCAL to 34 mrad. So, at high energies, SiCAL lacked enough data to provide an accurate measurement of  $\int \mathcal{L} dt$  and was used only to extend the calorimeter hermeticity in ALEPH. LCAL was therefore the only source of integrated luminosity.

BCAL, on the contrary, having a much lower angular acceptance ( $\theta_{\min} \sim 7$  mrad) due to its position, could detect a larger number of Bhabha events and had high enough statistical precision to provide an instantaneous luminosity value. BCAL was therefore used as an online luminosity monitor of the background conditions.

---

<sup>1</sup>The same process, via exchange of a Z boson, introduces some corrections in the total cross section which were poorly known at the start of LEP. By restricting the measurements to low  $\theta$ , the contribution from Z production is effectively reduced, and the rate of events is much larger. This is why these detectors sit very close to the beam-pipe.

## 2.5 Trigger System

At LEP, there was approximately one beam crossing every  $89\mu\text{s}$  but the detectors could not possibly record all those events at such an enormous rate. A decision on whether the event was ‘interesting’ was required to activate the readout system and record and store the event. However, of all the beam crossings, most resulted in ‘uninteresting’ events, like beam interactions with gas molecules in the accelerator, or off-momentum beam particles scattered by a collimator close to the IP. Only a small fraction of the beam crossings actually consisted of electron-positron interactions. The *trigger* system was designed to accept these events and reject the others. It also reduced the dead-time of the detector that results from readout.

The trigger system was built in three stages, the first two were hardwired logic to achieve a very fast response and the third one implemented in off-line software. Each one based their ‘yes’ or ‘no’ decision on different subdetectors depending on their capability to produce fast information about an event. Table 2.1 summarises the subdetectors used and the decision time.

Stage	Decision Time	Max. Rate (Hz)	Information Used
LEP beam crossing		$\sim 11000$	—
Level-1	$5\mu\text{s}$	$\sim 10$	Hit Patterns in ITC Pad/wire readout from ECAL+HCAL+LCAL
Level-2	$50\mu\text{s}$	$\sim 5$	Hit Patterns in TPC
Level-3	$62\text{ms}$	1-3	All subdetectors

Table 2.1: Summary of the ALEPH trigger system.

The first level trigger (Level-1) delivered a positive decision within  $5\mu\text{s}$ , much less than the beams crossing, if a good charged track had been registered by the ITC and/or the calorimeters had an energy deposit. This positive decision allowed the TPC to collect the drift electrons and partially reconstruct the tracks. If the Level-1 gave a ‘no’ decision, the TPC gate grid was closed and all the subdetectors reset for the next beam crossing, avoiding any dead time. The Level-2 needed around  $50\mu\text{s}$  to form a decision based on the TPC tracks: it required good tracks (exceeding a hit threshold) pointing to the interaction region. If the event satisfied the Level-2 conditions, the whole detector output was read out.

The Level-1 and Level-2 criteria valid for the 1999 and 2000 run periods is the following, with only minor modifications on the threshold values for previous years:

- Single Electron/Photon Triggers. Drift chamber (ITC for Level-1, TPC for Level-2) track segment pointing at an energy deposit in the ECAL of 200 MeV for electrons or a 2 GeV energy deposit for photons (with no track).
- Total Energy Trigger. ECAL energy deposits should exceed certain thresholds: 5.5 GeV in the barrel or 4.5 GeV in either end-cap or 1.7 GeV in both end-caps.
- Back-to-Back Track Trigger. Two ITC (or TPC for Level-2) tracks pointing in opposite directions from the IP.
- Single Muon Trigger. ITC or TPC track with at least 4 HCAL hits.

- Bhabha Luminosity Triggers. Hits in the LCAL with opposite azimuth.

In fact, the trigger achieved an efficiency greater than 99% in accepting the ‘interesting’ events, such as  $Z \rightarrow q\bar{q}$ ,  $Z \rightarrow \ell^+\ell^-$ , Bhabha scattering, or two-photon events.

## 2.6 Event reconstruction

Event reconstruction is the process by which raw data from the different subdetectors is transformed and correlated to form physically meaningful final data. It mainly consists of *track reconstruction*, which assigns each hit in the tracking chambers to a particle track, and *energy flow analysis*, which associates charged particle tracks with energy deposits in the calorimeters, enabling particle identification and improving the overall energy resolution. Event reconstruction begins just after the data is stored on tape and is run by JULIA (Job to Understand Lep Interactions in Aleph) [46]. Particle identification, as well as the rest of the user analysis of the events is performed by the computer program ALPHA (ALepH PHysics Analysis package) [47].

### 2.6.1 Track reconstruction

The information from all three tracking detectors is used to reconstruct a charged particle trajectory, or track. The reconstruction algorithm starts in the TPC. It links nearby hits to form segments. Several segments will be connected to form a track if the hypothesis that a helix is described is satisfied. This TPC track will then be extrapolated down to the ITC and VDET where matching hits will be assigned to the track. This solves any ambiguities that could arise from the two-dimensional ( $r\phi$  and  $z$ ) hits in the VDET.

A final track fit is then performed taking into account the segment errors by means of a Kalman filter technique [48] to provide a fully reconstructed track. Table 2.2 shows the momentum resolution achieved by incorporating the different subdetector segments into the track for a  $Z \rightarrow \mu^+\mu^-$  sample of events.

Tracking Detectors	Max. Hits	$\sigma_{p_t}/p_t^2$ (GeV/c) <sup>-1</sup>
TPC	21	$1.2 \times 10^{-3}$
TPC+ITC	21+8	$0.8 \times 10^{-3}$
TPC+ITC+VDET	21+8+2	$0.6 \times 10^{-3}$

Table 2.2: Transverse momentum resolution  $\sigma_{p_t}/p_t^2$  for  $p_t$  in GeV/c when the information from the different subdetectors is incorporated into the track reconstruction [42]. The number of maximum hits available for each subdetector corresponds to a track with 90° polar angle.

A ‘good’ track, as applied to the analysis described here, is defined as follows:

- A minimum of four hits in the TPC, which restricts good tracks to the range in polar angle:  $|\cos\theta| < 0.96$
- Transverse impact parameter:  $|d_0| < 1$  cm
- Longitudinal impact parameter:  $|z_0| < 5$  cm
- Transverse momentum:  $p_t > 2$  MeV/c

## 2.6.2 Energy Flow

The energy flow algorithms are designed to provide an accurate calculation of the total visible energy and momentum of an event. The energy resolution is fundamental in SUSY searches since their characteristic signature is large missing energy or momentum.

The event is first of all ‘cleaned’ by removing possible cosmics (the muons from cosmic showers initiated in the upper atmosphere) and electronic noise. Clusters of energy deposition are built in the calorimeters by adding together ‘storeys’ (in the ECAL) or towers (in the HCAL) which have energies above 30 MeV and share a common edge or corner. Good tracks, as defined in the previous section, are then extrapolated to these calorimeter clusters. This forms the so-called *energy flow objects*, which are groups of topologically connected tracks and clusters. Several such objects are defined:

- Electrons. They are identified using the ECAL shower profile. Their energy is calculated using their track momenta and mass. If the associated calorimeter cluster energy is greater than 3 times the expected energy, that extra energy is associated with a photon from bremsstrahlung.
- Muons. Identified by 400 MeV energy deposits per HCAL plane and up to 1 GeV in an ECAL cluster.
- Photons. Neutral energy clusters in the ECAL. If the invariant mass of two photons matches the mass of a  $\pi^0$ , a neutral pion is assumed.
- Charged and Neutral Hadrons. The remaining charged tracks are attributed to charged hadrons, and the remaining energy to neutral hadrons.

Finally, this analysis provides a list of objects which is expected to be an accurate representation of the true particles involved. The kinematic variables calculated from energy flow objects provide the basis for any further analysis of the event. For example, the visible mass of an event ( $M_{\text{vis}}$ ) is the invariant mass of all energy flow objects in that event; or the transverse momentum ( $p_t$ ) is the transverse component of the vector sum of momenta of all energy flow objects.

The energy flow resolution as a function of the polar angle is shown by the lower set of markers in Fig. 2.11, calculated for hadronic events  $Z \rightarrow q\bar{q}$ . The distribution of the reconstructed energy is fitted to a Gaussian giving an average relative resolution of  $\sim 7\%$ , reaching a maximum of 15% for  $\cos\theta \gtrsim 0.98$ . The ALEPH hermeticity is also shown in that figure, as a measurement of the reconstructed energy normalised to  $\sqrt{s}$ . The gradual decrease with  $\cos\theta$  in the measured energy for hadronic events arises from the high multiplicity of such events. Events with  $\cos\theta \gtrsim 0.9$  are more likely to have objects going down the beam-pipe, leading to a decrease in the measured energy. Otherwise, Bhabha and muon-pair events have low multiplicity and are very well reconstructed. However, there is a sudden drop in the measured energy for Bhabha events at  $\cos\theta \sim 0.98$ . This corresponds to the insensitive region where the LCAL meets the ECAL end-cap.

The high hermeticity of the detector and the precise measurements of the energy contained in the events, permit searches for new physics to be carried out successfully in ALEPH.

## 2.6.3 Lepton Identification

Lepton identification has a major role in the analysis described here, and needs to be described in some detail.

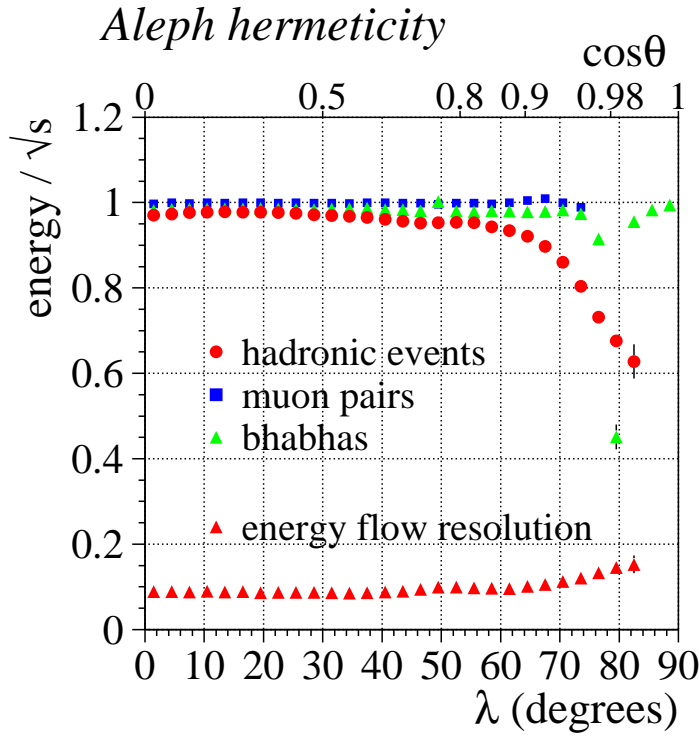


Figure 2.11: Energy flow resolution normalised to one as a function of the polar angle  $\theta$  ( $\lambda = \pi/2 - \theta$ ). An average energy flow resolution of 7% is achieved. The three sets of markers at the top of the plot show the reconstructed energy as a fraction of the total input energy ( $\sqrt{s}$ ). The sharp drop at  $\cos \theta \sim 0.98$  for Bhabha events is due to the gap region between the LCAL and ECAL. From Ref. [49].

## Electron Identification

Electron identification, as described in the previous section, relies on the energy profile deposited in the ECAL and additionally on the  $dE/dx$  information from the TPC. Three quantities, called *estimators*, are defined such that the measured value of a variable ( $q$ ) is compared to the mean expected value ( $\langle q \rangle$ ), taking the resolution ( $\sigma_q$ ) into account. The estimator ( $Q$ ) will have a standard Gaussian distribution:  $Q = \frac{q - \langle q \rangle}{\sigma_q}$ , centered at zero and with width unity. The estimators are: the transverse shower shape  $R_T$ , based on the compactness of the shower; the longitudinal shower shape  $R_L$ ; and  $R_I$ , based on the ionisation energy loss in the TPC.

The electron shower in the ECAL tends to be more compact in the transverse direction than that of a hadron like the pion. This leads to the definition of the  $R_T$  estimator, based on the compactness of the shower. The momentum  $p$  of the electron track is known from the TPC data. That track is extrapolated to the ECAL and the energy in the four towers closest to the extrapolated point is summed, giving  $E_4$ . The energy fraction  $E_4/p$  is the variable used in the  $R_T$  estimator:

$$R_T = \frac{E_4/p(\text{meas}) - E_4/p(\text{exp})}{\sigma_{E_4/p}} \quad (2.7)$$

The second estimator  $R_L$  is defined to take into account the longitudinal development of the electron shower, using the inverse of the mean depth of the energy deposition in the ECAL ( $X_L$ ):

$$X_L = \frac{E_4}{\sum_{i=1}^4 \sum_{j=1}^3 E_i^j S_j} \quad \implies \quad R_L = \frac{X_L(\text{meas}) - X_L(\text{exp})}{\sigma_{X_L}} \quad (2.8)$$



where the energy is summed over  $i$  storeys and  $j$  segments,  $S$  is the mean depth of energy deposition on that segment.

The estimator  $R_I$  is similarly defined, by comparing the measured  $dE/dx$  to what is expected for a particle with the mass and charge of an electron.

It is also important not to misidentify electrons produced originally in the IP with *photon conversions*, i.e. photons which interact with the VDET, ITC or TPC material and produce an  $e^+e^-$  pair. This  $e^+e^-$  pair does not have to be symmetric, and sometimes only one particle is energetic enough to be registered. Since there are many SM backgrounds involving photons, it is important not to take a conversion for a ‘genuine’ electron coming from the signal SUSY process. This is achieved by trying to identify pairs of tracks coming from a single displaced vertex. To tag conversions it is required that:

- the distance between the two tracks in  $xy$  plane at the point where they are parallel and closest together, is less than 2 cm,
- the distance between the two tracks in the  $z$  direction at that same point is less than 3 cm,
- the invariant mass of the two tracks at that point assuming they are both electrons is less than 40 MeV.

Finally, for an object to be identified as an electron it must pass the following criteria:

- It must be a ‘good’ track and not compatible with a photon conversion
- $p \geq 2 \text{ GeV}/c$
- $R_T \geq -3$
- $|R_L| \leq 3$
- $|R_I| \leq 3$

The average efficiency of the procedure has been evaluated to be 65% in hadronic events [42]. See Figs. 2.12a and b for the dependence of the efficiency with the transverse momentum and the polar angle. No evidence for a strong correlation between the two is found.

## Muon Identification

Muons have a different hit pattern in the HCAL than hadrons; they only interact with HCAL material by ionisation, not nuclear interactions, following a very narrow path, rather than extensive transverse areas. Muons are also expected to reach the outer regions of the HCAL, which means that planes further away from the IP are more likely to be fired by a muon than a hadron. Finally, the track extrapolated from the TPC, the narrow hits in the HCAL and the possible hits in the muon chambers aid in the correct identification of tracks as muons. Furthermore, these patterns are independent of the muon momentum for muons in the range  $5 - 50 \text{ GeV}/c$ . All muons above  $3 \text{ GeV}/c$  are able to penetrate out to the muon chambers.

Tracks are extrapolated from the TPC assuming they are muons defining a ‘road’ through the HCAL with a width of three times the uncertainty due to multiple scattering. A plane in the HCAL is expected to fire if the road intersects it. A plane is said to have fired if a digital hit lies within the width of the road. A hit in the muon chambers is assigned to the extrapolated track if it lies within four times the uncertainty due to multiple scattering. The

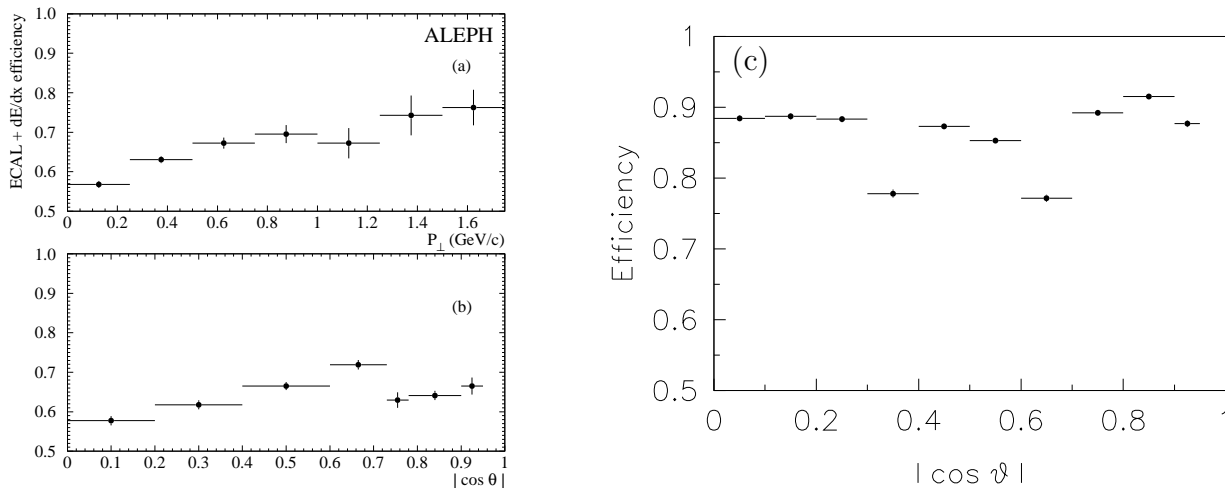


Figure 2.12: The efficiencies of the electron identification procedure as a function of (a) the transverse momentum and (b) the polar angle. The electron sample used comes from real data at the Z peak selecting photon conversions with high purity. (c) The efficiency of muon identification using both the HCAL and muon chambers information as function of the polar angle. The sample used is again real data  $Z \rightarrow \mu^+ \mu^-$  where high purity is obtained by selecting muons with TPC and ECAL information only. From Ref. [42].

depth of penetration of the track can be assessed by looking at the last ten planes, out of the total expected to be fired, that actually register a hit. Thus, a track can be identified as a muon if it satisfies the following conditions:

- $N_{\text{fire}}/N_{\text{exp}} \geq 0.4$
- $N_{\text{exp}} \geq 10$
- $N_{10} > 4$
- $X_{\text{mult}} \leq 1.5$
- At least one associated hit in the muon chambers

where  $N_{\text{fire}}$ ,  $N_{\text{exp}}$ ,  $N_{10}$  and  $X_{\text{mult}}$  are, respectively, the number of actually firing planes, the number of expected planes, the number of firing planes within the last ten expected and the average hit multiplicity per fired plane.

Applying these constraints on a dimuon events sample, an average efficiency of 86% is found. Figure 2.12c shows the muon identification efficiency as a function of the polar angle. The two dips are due to the magnet supporting legs, which are not instrumented with muon chambers.

## Tau Identification

The tau particle, the heaviest known lepton, can decay both leptonically or hadronically via the exchange of a W boson. This happens with a mean lifetime of 290 fs, or  $87 \mu\text{m}$ , just enough to be measured at ALEPH for boosted taus. The main decay modes are listed in Tab. 2.3. If the final state consists of one charged particle it is referred to as *one-prong*. This is the most likely decay mode with 85% probability and gives some relatively clean signal in the leptonic

Mode	$X$	Main Decay	BR(%)
One-prong	$e\bar{\nu}_e$	$\tau^- \rightarrow e^- \bar{\nu}_e \bar{\nu}_\tau$	18
	$\mu\bar{\nu}_\mu$	$\tau^- \rightarrow \mu^- \bar{\nu}_\mu \bar{\nu}_\tau$	17
	$h$	$\tau^- \rightarrow \pi^- \bar{\nu}_\tau$	13
	$h + \pi^0$	$\tau^- \rightarrow \pi^- \pi^0 \bar{\nu}_\tau$	25
	$h + 2\pi^0$	$\tau^- \rightarrow \pi^- 2\pi^0 \bar{\nu}_\tau$	10
	$h + 3\pi^0$	$\tau^- \rightarrow \pi^- 3\pi^0 \bar{\nu}_\tau$	1.5
3-prong	$3h$	$\tau^- \rightarrow \pi^- \pi^+ \pi^- \bar{\nu}_\tau$	9.5
	$3h + (\geq 1\pi^0)$	$\tau^- \rightarrow \pi^- \pi^+ \pi^- \pi^0 \bar{\nu}_\tau$	5
5-prong	$5h + (\geq 0\pi^0)$	$\tau^- \rightarrow 3h^- 2h^+ \bar{\nu}_\tau$	0.1

Table 2.3: Tau lepton main decay modes with the corresponding branching ratio (BR), rounded to nearest integer.  $X$  is the final state for  $\tau \rightarrow X\bar{\nu}_\tau$ .  $h$  stands for charged hadron and in general means a  $\pi^\pm$ , although  $K^\pm$  is also possible. Neutral pions decay promptly to two photons and charged pions are detected in the HCAL. The one-prong decay modes add up to 85%, the three-prong to 15% and the five-prong to  $\sim 0.1\%$ . Adapted from Ref. [5].

mode. On the other hand, for Lorentz-boosted taus decaying in the *three-prong* mode, it is usually very difficult to reconstruct the final particles ( $\pi^\pm$  and  $\pi^0$  in general) due to the small opening angle between the three.

Tau identification is performed by clustering the energy flow particles into two or four jets, depending on the analysis, with the Durham algorithm [50]. A jet will be a tau-jet candidate if it contains one or three good tracks (or two if it contains an identified electron, to allow for asymmetric photon conversions) and if the jet invariant mass is less than 2 GeV. A cut on the cluster-radius as a function of the momentum is also available.

It is important to define well the structure of jets, be it in Higgs, W or  $\tau$  decays. Several algorithms exist that operate by joining adjacent energy flow objects to form a jet. The Durham jet clustering algorithm used here, described in Ref. [50], uses the *invariant mass*  $M_{ij}$  of two objects  $i$  and  $j$  as a proximity measure. The procedure is as follows:

1. all possible pairs between particles are formed and the quantity

$$M_{ij}^2 = 2[\min(E_i, E_j)]^2(1 - \cos \theta_{ij}) \quad (2.9)$$

is evaluated, where  $E_i$  and  $E_j$  are the energies of the objects and  $\theta_{ij}$  is the angle between them.

2. the pair with the minimum value of  $M_{ij}^2$  is replaced by a pseudo-particle with energy  $E_i + E_j$  and momentum  $\vec{p}_i + \vec{p}_j$
3. steps 1 and 2 are iterated over the set of pseudo-particles and remaining objects until

$$y_{ij} \equiv \frac{M_{ij}^2}{E_{\text{vis}}^2} > y_{\text{cut}} \quad (2.10)$$

Thus the parameter  $y_{\text{cut}}$  sets the proximity condition for two tracks to be grouped together. The higher the value of  $y_{\text{cut}}$ , the easier it is to form jets with the available particles: so a larger

$y_{\text{cut}}$  will give fewer jets. The definition of  $M_{ij}$  is such that while the separation  $\theta_{ij}$  is important, the association of two objects is still possible if the value  $\min(E_i, E_j)$  is sufficiently low.

For instance, if we want to force the event into four jets, the value  $y_{\text{cut}}$  for which the event is grouped from three into four jets receives the name of  $y_{34}$ . A genuine four jet event will generally have a large value of  $y_{34}$ , thus tightening the value of  $y_{34}$  will reject processes that do not generally produce four jets.

## 2.7 Event Simulation

Any analysis in searches for new particles requires two event samples to be generated. One is the signal process we are interested in, for example slepton pair-production, and the other is the set of all known Standard Model processes that could mimic the signal process in the detector, the background. Finally, of course, there is the actual data collected with the detector which will decide if the signal has been found in the data and is distinguishable from background. Monte Carlo (MC) event samples for signal and background are generated with specific physics generators and processed in ALEPH in four stages.

1. The physics generator emulates  $e^+e^-$  collisions and produces the final state particles and four-momenta of the process or processes in question. The output is compliant with a set of kinematic rules imposed by KINGAL, an ALEPH program that will generate the kinematics of all particles in the final state to simplify further processing. This information is then passed onto the next stage,
2. GALEPH, the ALEPH detector simulation program, based on GEANT3 [51], which simulates the response of the ALEPH detector to the final state particles. GALEPH [52] contains a detailed and updated description of the geometry and composition of the detector and simulates the interactions of the generated particles with the sub-detectors on their passage through the different materials. The output format of GALEPH is the same as a real event.
3. As for real data, the next stage is the reconstruction program, JULIA [46], which facilitates the later analysis by forming physical objects. Unlike data, the reconstructed Monte Carlo files contain information on the true simulated event, thus enabling useful comparisons to be performed.
4. The final stage is the analysis itself where, based on the process under study, a set of variables is calculated for each event to try and make it distinguishable from the background and provide any necessary measurement. This is done with ALPHA, the ALepH PHysics Analysis package [47].

Usually, background files are generated and made available for the collaboration. In the analysis described here, background files were not generated by the author.

# Chapter 3

## Searches for six-lepton final state topologies in GMSB

The  $\tilde{\tau}_1$  NLSP scenario is favoured in GMSB models with the number of messenger families greater than one. In this case, pairs of selectrons and smuons may be produced at LEP2 and decay immediately to final states with two leptons and four taus and missing energy. This type of decay depends crucially on the mass difference between the sleptons and staus, but no less important is the neutralino mass, which enters the process as a mediating particle either on shell (two-body decays:  $\tilde{l}_R \rightarrow l\chi \rightarrow l\tau\tilde{\tau}_1$ ) or off-shell (three-body decays:  $\tilde{l}_R \rightarrow l\tau\tilde{\tau}_1$ ). Both processes are studied in this chapter. Up to now, only evidence for two-body decays has been looked for at colliders. The analysis described in this thesis is the first experimental search for the three-body process.

This final state topology is interesting because it covers a very sensitive area of parameter space, specially in the low gravitino mass range, i.e. for negligible stau lifetimes. Other searches, for cascade decays of neutralinos or direct slepton decays, are unable to cover this region of parameter space and thus the appeal to see if Nature has realised SUSY in this region.

After an introduction to the decays and the motivation for the search, the experimental searches are described in detail and since no evidence for this process has been found in the highest energy ALEPH data, limits on the cross section and sparticle masses are set.

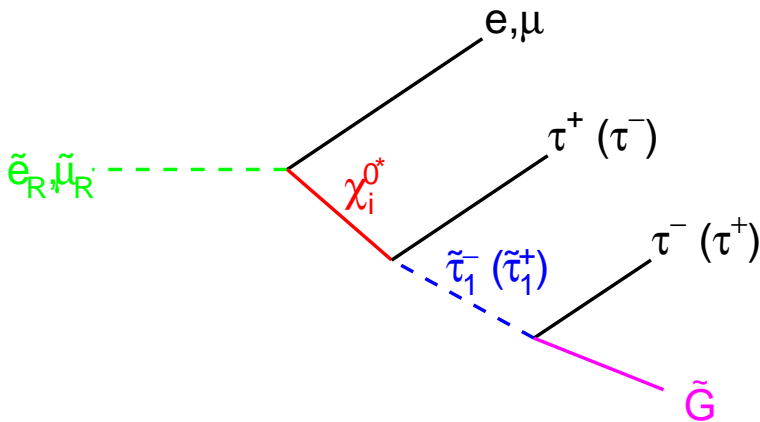


Figure 3.1: The decay of selectrons and smuons when the lightest stau is the NLSP, can occur via a two-body decay to an on-shell neutralino, or via a three-body decay directly to the NLSP through a virtual neutralino. Both cases are addressed in this work.

### 3.1 Phenomenology

In the context of Gauge Mediated SUSY Breaking (GMSB) models, final states with six leptons may appear when the lightest stau  $\tilde{\tau}_1$  is the NLSP and pairs of lightest selectrons  $\tilde{e}_R$  or smuons  $\tilde{\mu}_R$  are produced. The pair-production of sleptons at LEP is shown in Fig. 1.6a. The decay chain under study in this thesis is shown in Fig. 3.1.

The final state is thus two leptons  $l$ , either electrons or muons with opposite sign, four taus, and missing energy carried away by the undetected gravitinos. In the case of a light gravitino,  $m_{\tilde{G}} < 10 \text{ eV}/c^2$ , the NLSP will decay promptly after production. The analysis presented here will be restricted to this case. If the gravitino mass is between 10 and around  $500 \text{ eV}/c^2$ , the  $\tilde{\tau}_1$  will present some sizeable decay length in the detector and the topology would then have kinks or large impact parameters from the  $\tilde{\tau}_1$  decays. This analysis ‘with lifetime’ has been performed by OPAL in Ref. [53].

The decay of the selectron or smuon  $\tilde{l}_R$ , occurs via a neutralino. It has usually been assumed in experimental searches that the neutralino would be on-shell with a mass range between:

$$\boxed{m_{\tilde{l}_R} - m_l > m_\chi > m_{\tilde{\tau}_1} + m_\tau} \quad (3.1)$$

where,  $l$  stands for  $e$  or  $\mu$ . And hence the decay would follow two-body kinematics:

$$\text{Two - body : } e^+e^- \rightarrow \tilde{l}_R \tilde{l}_R \rightarrow l_\chi l_\chi \rightarrow l\tau\tilde{\tau}_1 l\tau\tilde{\tau}_1 \rightarrow l\tau\tau\tilde{G} l\tau\tau\tilde{G} \quad (3.2)$$

But specially important is the fact that this decay can proceed through an off-shell neutralino with the special kinematics of three-body decays:

$$\boxed{m_\chi > m_{\tilde{l}_R} - m_l > m_{\tilde{\tau}_1} + m_\tau} \quad (3.3)$$

$$\text{Three - body : } e^+e^- \rightarrow \tilde{l}_R \tilde{l}_R \rightarrow l\tau\tilde{\tau}_1 l\tau\tilde{\tau}_1 \rightarrow l\tau\tau\tilde{G} l\tau\tau\tilde{G} \quad (3.4)$$

Three-body decays of selectrons or smuons into the lepton, tau and stau have been theoretically studied in Ref. [54] and this thesis is the first experimental search for this particular

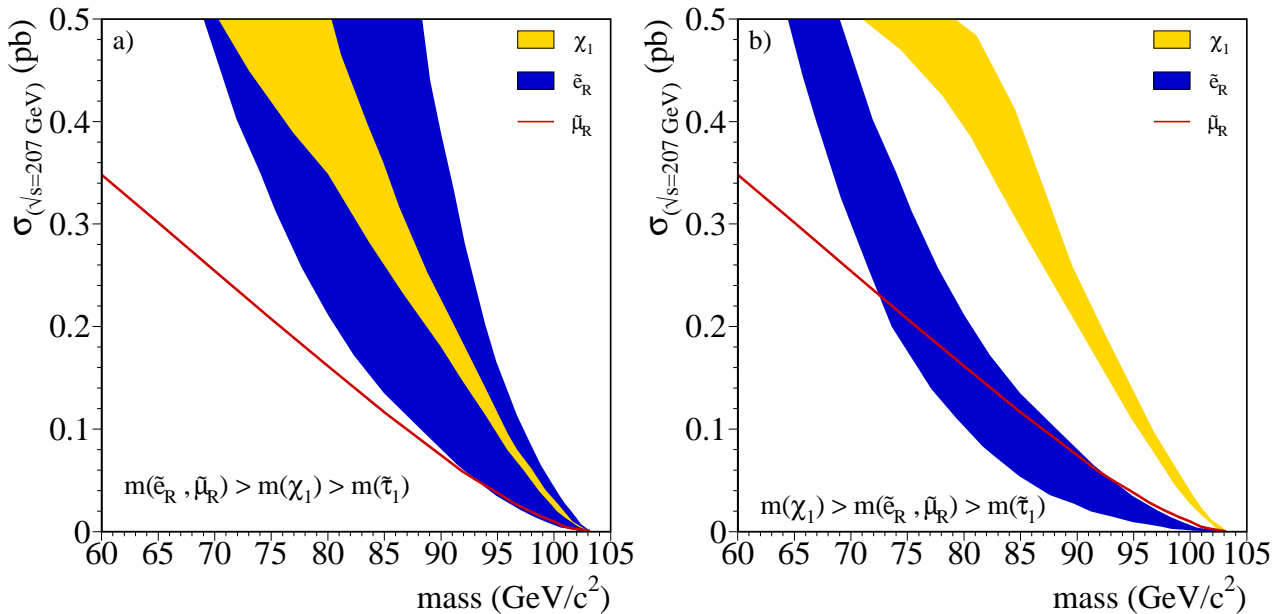


Figure 3.2: Pair-production cross sections at  $\sqrt{s} = 207 \text{ GeV}$  for the lightest neutralino, selectron and smuon in the (a) two-body and (b) three-body scenarios. Selectrons (dark shaded area) may have larger production cross sections than neutralinos (light shaded area) in the two-body case, but never in the three-body case. The lightest stau production cross section, not relevant for six-lepton topologies, is very similar to the smuon cross section since they do not have  $t$ -channel contributions.

type of decay. In this case, there is the advantage of eliminating the upper constraint on the neutralino mass (left hand side in Eq. 3.1), which can now lie well above the  $\tilde{l}_R$  mass or the beam energy at LEP. This search is therefore sensitive to an unexplored range of neutralino masses at LEP2.

Figure 3.2 shows the production cross section as a function of particle mass for neutralinos, selectrons and smuons in the two-body and three-body scenarios. The  $\tilde{\mu}_R^+ \tilde{\mu}_R^-$  production cross section is only larger than that of  $\tilde{e}_R^+ \tilde{e}_R^-$  for masses greater than  $\sim 90 \text{ GeV}/c^2$  in the three-body scenario. So one may expect more  $\mu^+ \mu^- \tau \tau \tilde{\tau}_1 \tilde{\tau}_1$  events than  $e^+ e^- \tau \tau \tilde{\tau}_1 \tilde{\tau}_1$  with three-body kinematics, although this is not guaranteed. Smuons are only produced via  $s$ -channel exchange of a  $\gamma$  or  $Z$ , while selectron and neutralino pair-productions are model dependent via the additional  $t$ -channel exchange of a neutralino and a selectron respectively, see Fig. 1.6. The  $t$ -channel contribution to the neutralino cross section is constructive, hence the generally higher neutralino cross section in the three-body case with respect to the two-body case, where the exchanged selectron is heavier than the neutralino. On the contrary, the interference between  $s$  and  $t$  diagrams is destructive in the selectron production, so that light neutralinos cause the  $t$ -channel to dominate and reduce the total cross section.

As a result, three-body  $\tilde{l}_R$  decays are disfavoured at the production level with respect to neutralino production with a slepton NLSP. The decay of selectrons and smuons with a stau NLSP has to compete in the available parameter space with direct slepton NLSP production ( $\tilde{\ell} \rightarrow \ell \tilde{G}$ ) and neutralino production with a slepton NLSP ( $\chi \rightarrow \tilde{\ell} \ell \rightarrow \ell \ell \tilde{G}$ ). However, the six-lepton final state topology offers a complementary channel for the discovery of supersymmetry in GMSB models and is sensitive to exclusive areas of parameter space. A discussion on the available parameter space in GMSB models for this type of topology follows.

### 3.1.1 Available parameter space

In GMSB models with  $N_5 > 1$  the  $\tilde{\tau}_1$  NLSP scenario dominates. This can be clearly seen in Fig. 3.3, where Region 1, corresponding to a  $\chi$  NLSP is only dominant for  $N_5 < 2$ . Regions 2 and 4 correspond to a  $\tilde{\tau}_1$  NLSP scenario, where the six-lepton final state topology is possible. Three-body decays of  $\tilde{l}_R$  have more parameter space available (Region 4) than two-body decays (Region 2) for  $N_5 > 1$ . It is also noticeable how Region 4 extends down to relatively low values of  $\tan\beta \sim 5$  independently of  $\Lambda$ . For even lower values of  $\tan\beta$ , the  $\tilde{l}_R - \tilde{\tau}_1$  mass difference becomes less than the tau mass and the three sleptons coexist as co-NLSP (Region 3).

In the stau NLSP scenario, if the mass ordering is  $m_{\tilde{l}_R} - m_l > m_\chi$ , then the two-body decay  $\tilde{l}_R \rightarrow l\chi$  dominates over  $\tilde{l}_R \rightarrow l\tilde{G}$ . The latter decay is suppressed by the gravitational nature of the gravitino. If the mass order is  $m_\chi > m_{\tilde{l}_R} - m_l > m_{\tilde{\tau}_1} + m_\tau$  the three-body modes  $\tilde{l}_R \rightarrow l\tau\tilde{\tau}_1$  will dominate<sup>1</sup> as shown in Fig. 3.4. The decay to  $\tilde{l}_R \rightarrow l\chi$  is impossible in this region of masses, and only  $\tilde{l}_R \rightarrow l\tilde{G}$  may become available in pathological cases where the slepton mass is very close to the stau mass and the decay to the stau is thus not possible. Only then the direct decays from sleptons to gravitinos may be realised overcoming the very low gravitational coupling. Once  $\tan\beta$  is greater than  $\sim 10$  the stau mass becomes much lighter than the slepton masses due to mixing effects and the three-body decay modes are restored. It is found that all slepton decays proceed through  $\tilde{l}_R \rightarrow l\tau\tilde{\tau}_1$  and  $\tilde{l}_R \rightarrow l\tilde{G}$  is avoided if the difference between the slepton and the stau masses is greater than  $5 \text{ GeV}/c^2$ .

### 3.1.2 Kinematics of two- and three-body $\tilde{l}_R$ decays

In the two-body scenario (Eq. 3.1) the mediating neutralino decays independently into  $\tau^-\tilde{\tau}_1^+$  or  $\tau^+\tilde{\tau}_1^-$  with equal probability. One expects therefore no asymmetry in the charges of the two staus: there will be equal numbers of like-signed staus and opposite-signed staus. But in the three-body scenario, it is important to distinguish between the different charge channels, since the decay widths  $\Gamma(\tilde{l}_R^- \rightarrow l^-\tau^+\tilde{\tau}_1^-)$  and  $\Gamma(\tilde{l}_R^- \rightarrow l^-\tau^-\tilde{\tau}_1^+)$  can actually be quite different. This asymmetry is caused by the different coupling of the neutralino to the stau depending on the stau mixing. If the lightest stau is purely right-handed, there is no asymmetry and the largest hypercharge states  $\tau_R^-$  and  $\tau_L^+$  are predominantly produced in equal amounts as primary taus. But if the left-handed stau content of the lightest stau increases, i.e. the mixing angle  $\theta_{\tilde{\tau}}$  increases, then the wino ( $\tilde{W}_3$ ) nature of the neutralino will prefer the state with more  $\tau_L^-$  content and the asymmetry will be created.

Assuming a fully bino neutralino, which is generally almost true in GMSB models, and a near threshold production (small  $\tilde{l}_R$  momenta), one can deduce the following relations<sup>2</sup>:

$$\Gamma(\tilde{l}_R^- \rightarrow l^-\tau^+\tilde{\tau}_1^-) \sim \frac{m_{\tilde{l}_R}^5}{(m_\chi^2 - m_{\tilde{l}_R}^2)^2} \left[ \sin\theta_{\tilde{\tau}} + \frac{m_\chi}{m_{\tilde{l}_R}} \cos\theta_{\tilde{\tau}} \right]^2 \quad (3.5)$$

$$\Gamma(\tilde{l}_R^- \rightarrow l^-\tau^-\tilde{\tau}_1^+) \sim \frac{m_{\tilde{l}_R}^5}{(m_\chi^2 - m_{\tilde{l}_R}^2)^2} \left[ \cos\theta_{\tilde{\tau}} + \frac{m_\chi}{m_{\tilde{l}_R}} \sin\theta_{\tilde{\tau}} \right]^2 \quad (3.6)$$

Both the ‘slepton-charge flipping’ channel (Eq. 3.5) and the ‘slepton-charge preserving’ decay (Eq. 3.6) are suppressed for increasing neutralino mass, with other parameters held

<sup>1</sup>There could also be three-body decays  $\tilde{l}_R \rightarrow \nu_l \bar{\nu}_\tau \tilde{\tau}_1$  through off-shell charginos  $\chi_1^\pm$ , although they are strongly suppressed due to the large chargino mass and the very small coupling of  $\tilde{l}_R$  to  $\nu_l \chi^\pm$ .

<sup>2</sup>After some algebra from the calculations in Ref. [54]



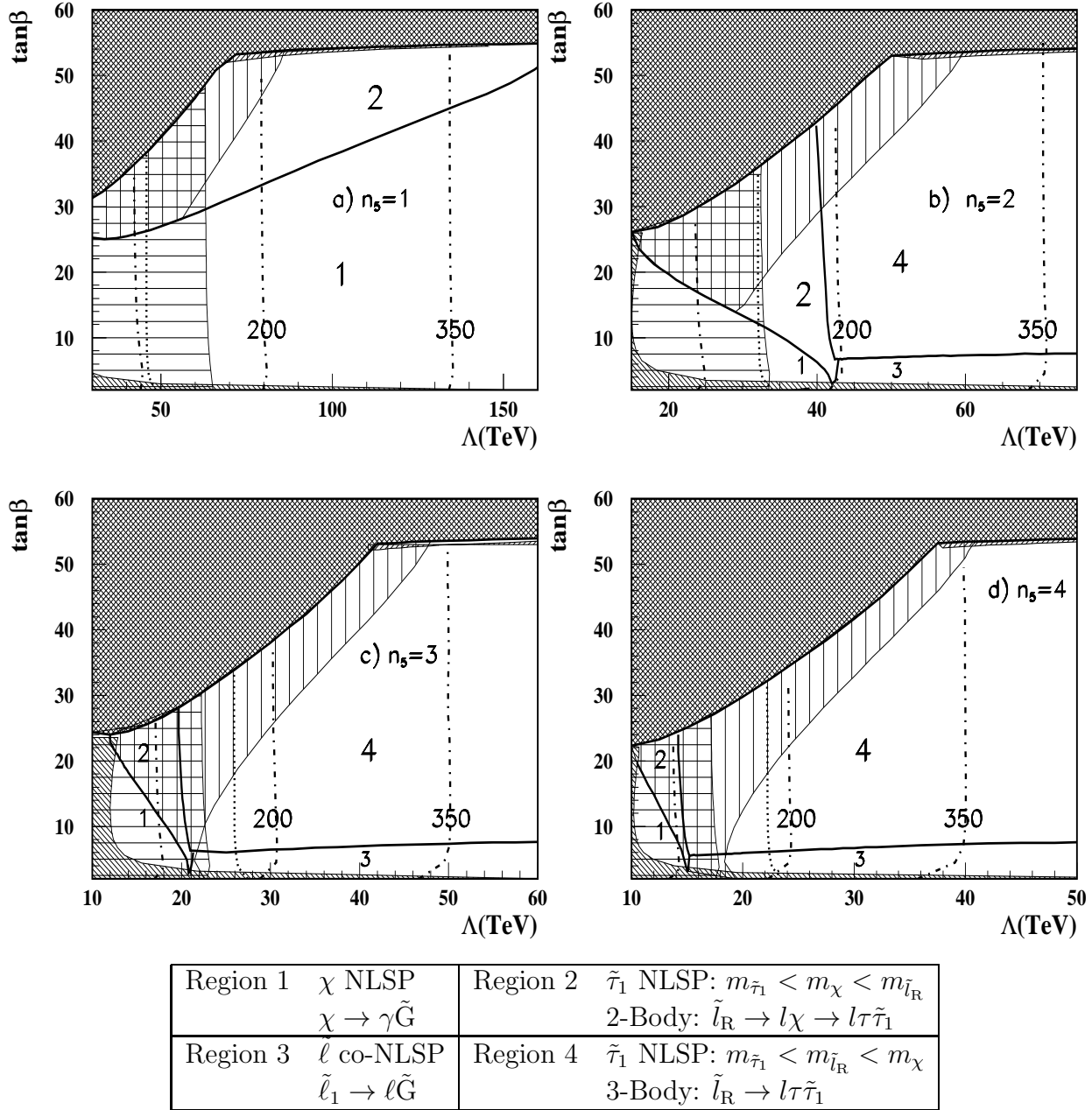


Figure 3.3: In the plane  $(\Lambda, \tan\beta)$  and for  $N_5 = 1, 2, 3, 4$  (a, b, c and d respectively), regions of  $\chi$  NLSP (1),  $\tilde{\ell}$  co-NLSP (3) and  $\tilde{\tau}_1$  NLSP with  $m_\chi < m_{\tilde{l}_R}$  (2) and  $m_\chi > m_{\tilde{l}_R}$  (4).  $M_m$  has been fixed at  $3\Lambda$  and  $\mu$  is positive. The heavy solid lines denote the boundaries between these regions. Regions 2 and 4 are those relevant for the six-lepton final state topology, where it has to compete with  $\chi \rightarrow \tau\tilde{\tau}_1$  and direct production processes. The cross-hatched region at high  $\tan\beta$  is excluded because electroweak symmetry is not correctly broken. The shaded regions are excluded because  $m_{\tilde{\tau}} \leq 76 \text{ GeV}/c^2$  (vertical shading),  $m_\chi \leq 84 \text{ GeV}/c^2$  (horizontal shading) or  $m_h \leq 95 \text{ GeV}/c^2$  (or  $m_A \leq 83 \text{ GeV}/c^2$ ) (diagonal shading). The dot-dashed contours are where the chargino mass is 95, 200 or 350  $\text{GeV}/c^2$ , while the dotted line is the contour of  $m_{\tilde{e}_R} = 90 \text{ GeV}/c^2$ . From Ref. [55].

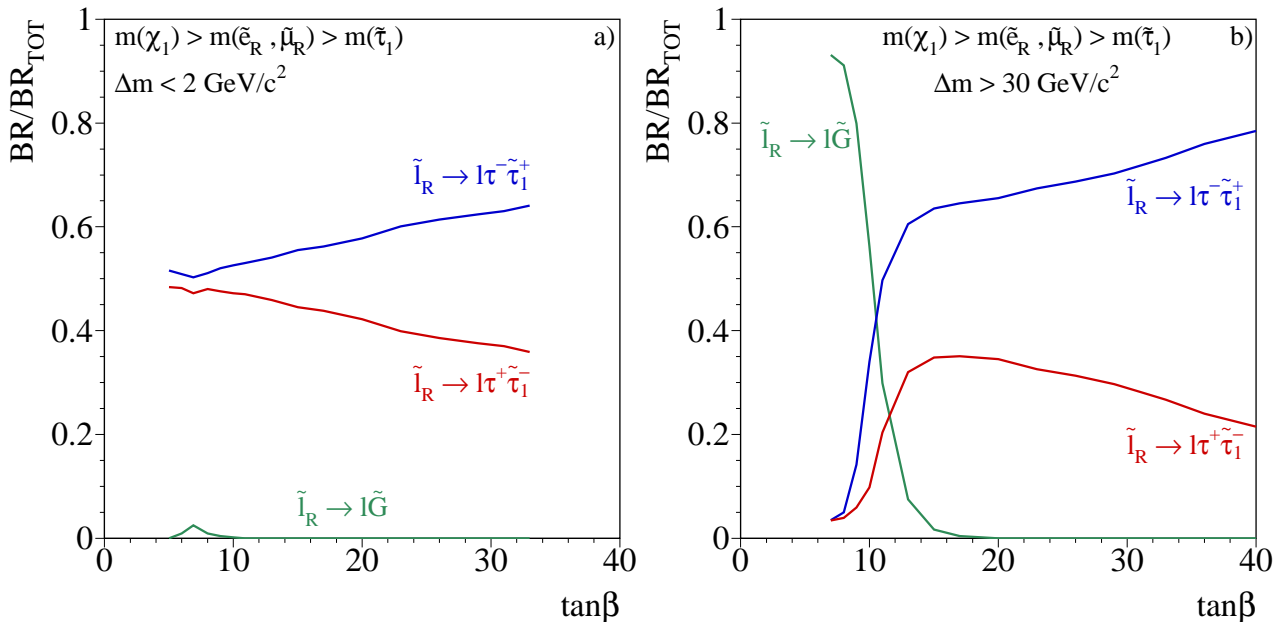


Figure 3.4: Slepton branching fractions as a function of  $\tan\beta$  in the three-body scenario for two ranges in  $\Delta m_{\chi\tilde{l}} = m_\chi - m_{\tilde{l}_R}$ . Only for highly virtual neutralinos ( $\Delta m_{\chi\tilde{l}} > 30 \text{ GeV}/c^2$ ) and  $\tan\beta \leq 10$  (or  $m_{\tilde{l}_R} - m_{\tilde{\tau}_1} < 5 \text{ GeV}/c^2$ ) may the channel  $\tilde{l}_R \rightarrow l\tilde{G}$  be open and dominate. Otherwise the three-body decay modes dominate. The asymmetry between  $\Gamma(\tilde{l}_R^- \rightarrow l^-\tau^-\tilde{\tau}_1^+)$  and  $\Gamma(\tilde{l}_R^- \rightarrow l^-\tau^+\tilde{\tau}_1^-)$  is explained in Sec. 3.1.2. The condition  $m_\chi > m_{\tilde{l}_R} - m_l > m_{\tilde{\tau}_1} + m_\tau$  is only possible for  $\tan\beta \geq 5$  and  $N_5 \geq 2$ .

fixed. Figure 3.4 shows the asymmetry between the two decay modes as a function of  $\tan\beta$ , which is roughly inversely proportional to the stau mixing angle  $\theta_{\tilde{\tau}}$ , and as a function of  $\Delta m_{\chi\tilde{l}} = m_\chi - m_{\tilde{l}_R}$ . It is clear from the plots that:

$$\Gamma(\tilde{l}_R^- \rightarrow l^-\tau^-\tilde{\tau}_1^+) \geq \Gamma(\tilde{l}_R^- \rightarrow l^-\tau^+\tilde{\tau}_1^-) \quad (3.7)$$

so that same-sign  $\tau^\pm\tau^\pm\tilde{\tau}_1^\mp\tilde{\tau}_1^\mp$  states are suppressed compared to opposite-sign states  $\tau^+\tau^-\tilde{\tau}_1^+\tilde{\tau}_1^-$ . This effect will be most significant for large  $m_\chi/m_{\tilde{l}_R}$  and for small negative values of  $\cos\theta_{\tilde{\tau}}$ . For  $m_{\tilde{l}_R} - m_{\tilde{\tau}_1} < 10 \text{ GeV}/c^2$ ,  $|\cos\theta_{\tilde{\tau}}|$  usually ranges between 0.1 and 0.3 (small mixings).

The kinematics of the event will ultimately depend upon the mass differences:  $m_{\tilde{l}_R} - m_{\tilde{\tau}_1}$ ,  $|m_{\tilde{l}_R} - m_\chi|$  and  $m_\chi - m_{\tilde{\tau}_1}$ , neglecting lepton masses. Figure 3.5 shows the energy distributions for the lepton and the primary tau in both two- and three-body decays with  $m_{\tilde{l}_R} - m_{\tilde{\tau}_1}$  fixed at  $\sim 11 \text{ GeV}/c^2$ . In the two-body scenario, as one would expect, the energy of the primary lepton is fully dependent on the  $\tilde{l}_R - \chi$  mass difference whereas the energy of the tau lepton depends on  $m_\chi - m_{\tilde{\tau}_1}$ . But in the three-body scenario, these energy distributions prove to be completely independent of the neutralino mass: i.e., no matter how virtual ( $m_\chi - m_{\tilde{l}_R}$ ) the neutralino is, the lepton and primary tau energies are determined only by the total available energy  $\sim E_{\text{beam}} - m_{\tilde{\tau}}$ .

The analysis described here will assume negligible stau lifetime ( $m_{\tilde{G}} < 10 \text{ eV}/c^2$ ). Could the sleptons nevertheless have a long lifetime? The probability that a slepton  $\tilde{l}_R$  with energy

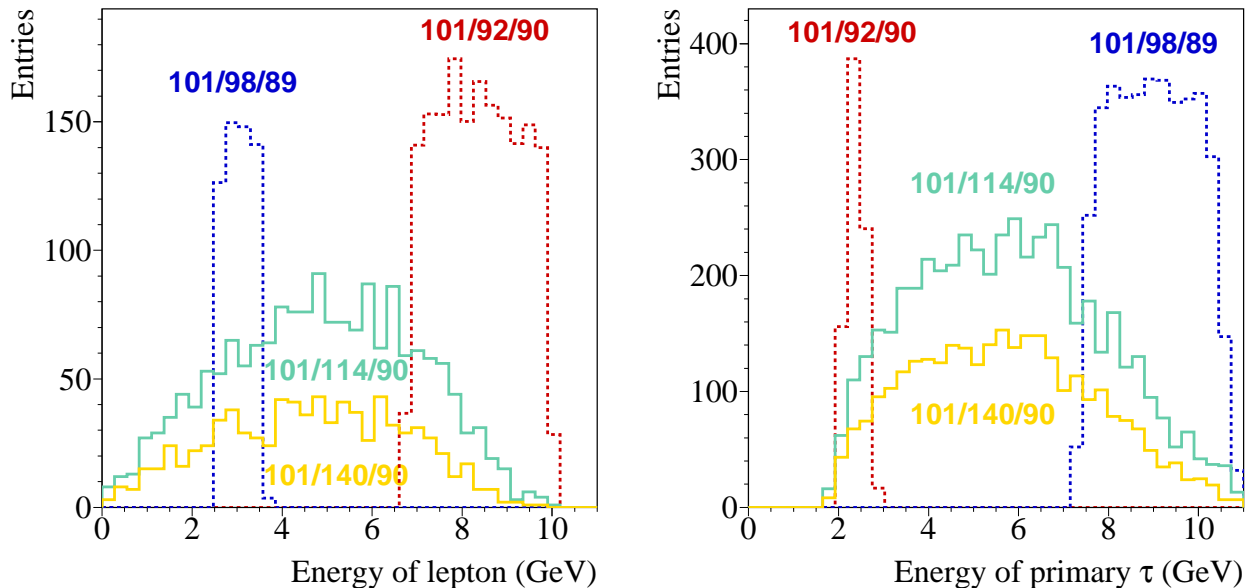


Figure 3.5: Energy distributions, with arbitrary vertical axis, for lepton (electron or muon) and primary tau at the generation level. The dotted histograms represent the two-body decay modes  $\tilde{l}_R \rightarrow l\chi$  and the full histograms, the three-body decays  $\tilde{l}_R \rightarrow l\tau\tilde{\tau}_1$ . Signal points are denoted by:  $m_{\tilde{l}_R}/m_\chi/m_{\tilde{\tau}_1}$ . In both cases  $\Delta m = m_{\tilde{l}_R} - m_{\tilde{\tau}_1}$  is fixed at  $\sim 11 \text{ GeV}/c^2$  and the neutralino mass is changed to see the effect.

$E$  will travel a distance  $x$  in the lab frame before decaying is given by:

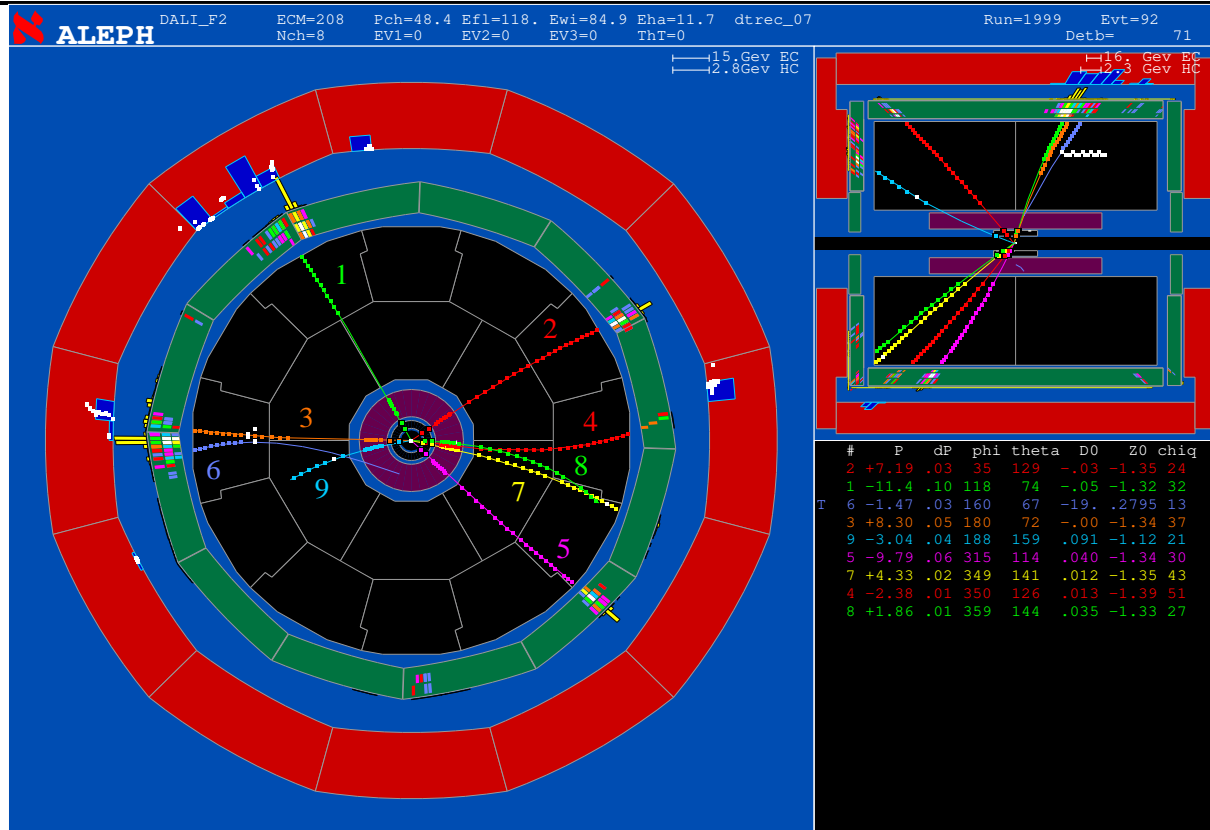
$$P(x) = e^{-x/\lambda} \quad \text{with} \quad \lambda = c\tau\gamma\beta = 0.2 \left( \frac{1 \text{ meV}}{\Gamma_{\tilde{l}_R}} \right) \sqrt{\frac{E^2}{m_{\tilde{l}_R}^2} - 1} \text{ mm} \quad (3.8)$$

It can be shown [54] that the decay length for sleptons produced at LEP2 (where  $E$  is the beam energy, and thus the Lorentz factor is not much greater than 1) is only measurable if  $\Delta m = m_{\tilde{l}_R} - m_{\tilde{\tau}_1}$  is less than one GeV. It is therefore assumed in this analysis, without loss of generality, that the sleptons will not have a sizeable decay length.

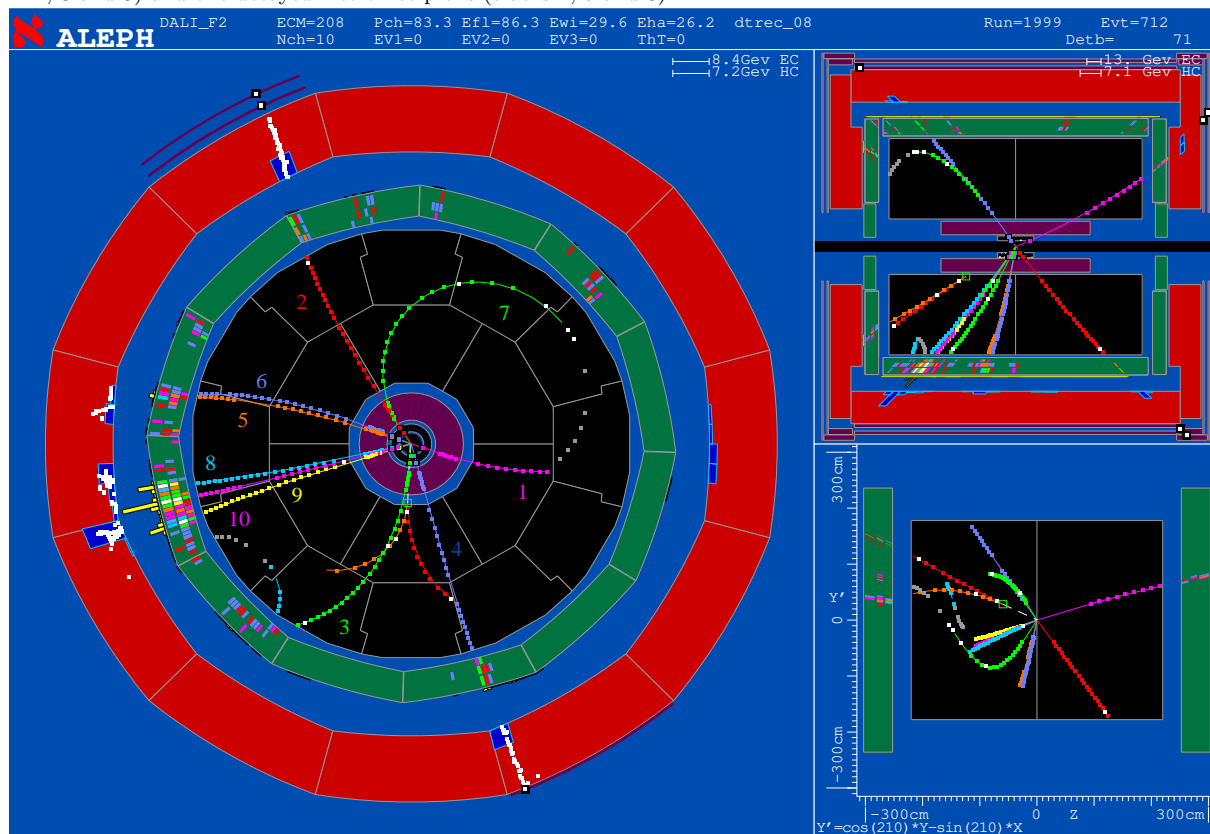
Examples of how selectron and smuon production with six-lepton final states might look are shown in Fig. 3.6.

## 3.2 Data sample and Monte Carlo simulation

Six-lepton events with missing energy in GMSB scenarios constitute the events of interest in this analysis, and they are called ‘signal’ events. Once they have been described and the new physics behind them is understood, it is necessary to know how would they look were they to be produced in a collision in the ALEPH detector. This is performed by means of Monte Carlo simulation. The same technique is utilised in generating Standard Model processes that could mimic or fake the signal events we are interested in. These processes, arising from known physics, are called ‘background’ events. A ‘selection’ procedure to distinguish between the two will be devised such that it retains the maximum number of signal events and rejects as many unwanted background events as possible. Finally, the selection is applied to the real data



(a) Two selectrons were produced with  $99 \text{ GeV}/c^2$  which then decayed to two electrons (tracks 2 and 5) and two neutralinos with mass  $90 \text{ GeV}/c^2$ . Of the four produced taus, three underwent a one-prong decay into pions (tracks 1, 3 and 9) and one decayed into three pions (tracks 4, 7 and 8).



(b) Two smuons decaying via a three-body process. The two corresponding muons are tracks 1 and 2. One of the primary taus decayed into a  $\pi^+$  (track 3) and the other into three pions (tracks 5, 6 and 7). The secondary taus coming from the staus decayed into a muon (track 4) and into three pions (tracks 8, 9 and 10). There is a photon conversion in the inner wall of the TPC, between tracks 3 and 4.

Figure 3.6: Signal Monte Carlo events at  $\sqrt{s} = 208 \text{ GeV}$ . The detector is shown in the ‘fish-eye’ view to magnify the tracking relative to the calorimeters.

collected by ALEPH. A measurement of the degree of evidence for the signal process under investigation can then be obtained by comparing the selected number of events in the data and the expected number of events from the background simulation.

### 3.2.1 Data sample

The data analysed in this thesis were collected with the ALEPH detector between 1998 and 2000 with a total integrated luminosity of  $628 \text{ pb}^{-1}$  at centre-of-mass energies between 189 and 209 GeV. Table. 3.1 gives the detailed luminosity at each energy. The LEP accelerator was pushed to its limits during year 2000 and ALEPH collected  $11.6 \text{ pb}^{-1}$  of data between 200 and 204 GeV,  $197.3 \text{ pb}^{-1}$  between 205 and 207 GeV and  $7.3 \text{ pb}^{-1}$  at more than 208 GeV. The excellent performance of both the accelerator and the detector must be acknowledged.

Year	1998	1999				2000	
$\langle\sqrt{s}\rangle$ (GeV)	188.6	191.6	195.5	199.5	201.6	205.0	206.7
$\int \mathcal{L} dt$ ( $\text{pb}^{-1}$ )	173.6	28.9	79.9	87.0	44.4	79.5	134.3

Table 3.1: Average centre-of-mass energy and corresponding luminosities of the analysed data sample for data collected by the ALEPH detector from 1998 to 2000.

### 3.2.2 Signal

The ALEPH SUSY Task Force generally uses SUSYGEN [56] as the signal Monte Carlo program for the generation of supersymmetric events in the simulation. All searches described in this thesis were performed using SUSYGEN, except the six-lepton search described in this chapter. SUSYGEN is unable to produce the type of events where selectrons and smuons are heavier than the stau and the decay is a three-body mode. Instead, ISAJET 7.51 [57] which has the full capability to generate  $\tilde{l}_R \rightarrow l\tau\tilde{\tau}_1$  events was used. ISAJET had to be interfaced with KINGAL to allow the generated events to be processed by the standard ALEPH reconstruction routines.

In the GMSB framework, the minimum number of parameters to describe a complete sparticle spectrum is six:  $\Lambda$ ,  $M_m$ ,  $m_{\tilde{G}}$  (or  $\sqrt{F_0}$ ),  $N_5$ ,  $\tan\beta$  and  $\text{sign}(\mu)$ . But phenomenologically there are only three relevant parameters in the search for slepton decays: the masses of the SUSY particles involved,  $m_{\tilde{l}_R}$ ,  $m_\chi$  and  $m_{\tilde{\tau}_1}$ , which will completely determine the kinematics of the event. Instead of an artificial grid with values for the three masses, the scan over the six theoretical parameters described in Sec. 5.1 was used to obtain the interesting values for the masses. Thus having scanned millions of possible GMSB models, the chosen signal points were obtained by imposing the appropriate hierarchy in masses (Eqs. 3.1 and 3.3) and the zero lifetime condition  $m_{\tilde{G}} < 10 \text{ eV}/c^2$  for the stau NLSP.

Some reduction was needed in the number of selected signal points, and this was performed in the three mass-planes involved  $(m_\chi, m_{\tilde{\tau}_1})$ ,  $(m_\chi, m_{\tilde{l}_R})$  and  $(m_{\tilde{l}_R}, m_{\tilde{\tau}_1})$  by requiring a separation between the points of more than  $2 \text{ GeV}/c^2$  in any one plane. A high density of points was achieved without unnecessary overlapping. Only stau NLSP masses greater than  $70 \text{ GeV}/c^2$  were used. In Fig. 3.7 the signal points are ordered with decreasing  $m_{\tilde{l}_R}$  in the horizontal axis and the values of their three defining masses are shown in the vertical axis to illustrate the fine coverage of all possible kinematical regions.

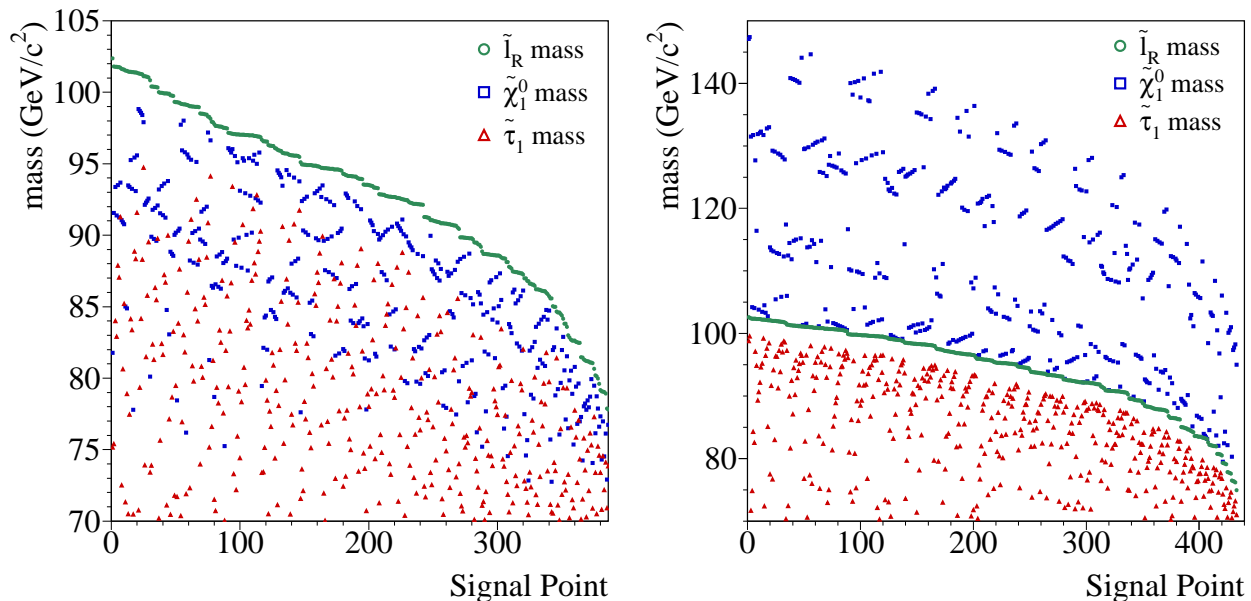


Figure 3.7: The signal points in GMSB parameter space were obtained from the scan described in Sec. 5.1. The relevant kinematical parameters, the mass of sleptons, neutralino and stau, are shown here for each signal point in the two-body scenario (left) and three-body scenario (right). In the three body scenario  $\Delta m = m_{\tilde{l}_R} - m_{\tilde{\tau}_1} > 5 \text{ GeV}/c^2$  to ensure that no slepton decays into  $l\tilde{G}$ .

A total of 385 and 457 points in the minimal GMSB parameter space were used as signal for the two-body and the three-body scenarios respectively. For each point, a total of 1000 events were produced at  $\sqrt{s} = 189, 206$  and  $208 \text{ GeV}$ . Taking into account the beam energy limit in the production of sleptons, this represents a total of 2 million reconstructed signal events.

Finally, the simulated signal points in the two- and three- body scenarios are shown in Fig. 3.8 in the  $(m_\chi, m_{\tilde{\tau}_1})$  plane. Also shown are the present limits derived from other GMSB searches (described in Chapter 4). This plot demonstrates the reach of three-body slepton decays over an area in parameter space where the neutralino is heavier than the beam energy and is not excluded by existing limits. This is the main motivation to use this topology and cover that region of parameter space. In the case of two-body decays, one is limited by the kinematical conditions and is further constrained by the suppressed slepton production cross section with respect to neutralino production.

### 3.2.3 Background

Standard Model processes have to be simulated and reconstructed in ALEPH in order to compare data and ‘known physics’ predictions; only when the first shows disagreement with the latter does the possibility for new physics arise. It is therefore very important to understand and be able to simulate correctly all possible processes that could resemble the one sought. Table 3.2 lists for each centre-of-mass energy the cross section, number of reconstructed events and MC generator for each of the analysed backgrounds. The background generation was performed by other members of the ALEPH collaboration, corresponding to at least 20 times the collected luminosity in the data.

Cross sections for some of these processes at LEP2 energies are shown in Fig. 3.9. For comparison, typical SUSY particle cross sections are  $\sim 0.1 \text{ pb}$  or less if the particles are produced at threshold ( $m \sim \sqrt{s}/2$ ), as can be seen in Fig. 3.2.

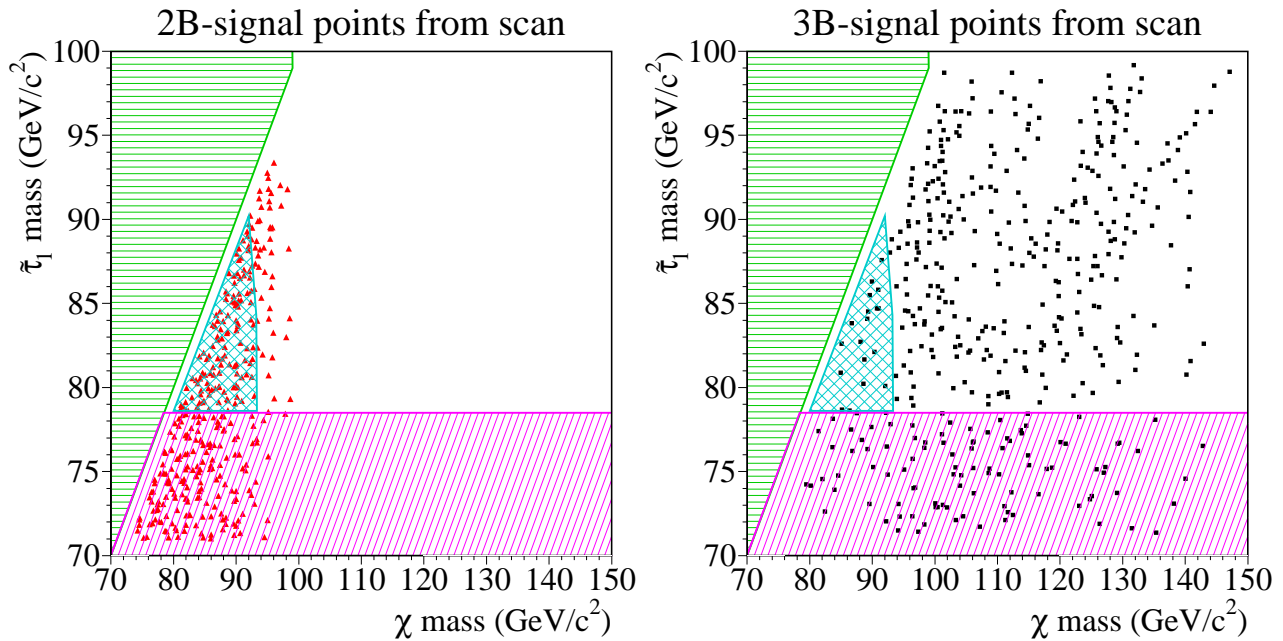


Figure 3.8: Signal events were generated at each one of the two-body (left) and three-body (right) points displayed here in the neutralino-stau mass plane. The hatched areas mark the present exclusion from GMSB searches in that plane for  $m_{\tilde{G}} < 10 \text{ eV}/c^2$ , as explained in Fig. 5.3.

### Two-fermion processes

These are  $e^+e^- \rightarrow Z/\gamma \rightarrow f\bar{f}$  processes, where  $f$  is a quark or lepton (Fig. 3.10a). They were the dominant background at LEP1 when the centre-of-mass energy was the  $Z$  mass, and thus the cross section was maximal. As LEP energies have increased away from the  $Z$  peak and above the  $WW$  threshold, the dominant background has become four fermion processes. At LEP2,  $e^+e^- \rightarrow Z$  will often be produced with an ISR (initial state radiation) photon at low angle. This is the so called *radiative return to the Z* and leads to missing momentum signatures. Only  $\tau^+\tau^-$  and  $q\bar{q}$  events could resemble the six-lepton final state topology and constitute a relevant background to the signal.

### Four-fermion processes

$W$  pair-production  $e^+e^- \rightarrow W^+W^-$  such as shown in Figs. 3.10c and d, constitutes a source for jets and leptons since  $W$  can decay into  $q\bar{q}$  (70%) and  $\ell\nu$  (30%). Similarly,  $e^+e^- \rightarrow ZZ^*$  (with  $Z^* = Z$  or  $\gamma$ ) is a major background for SUSY processes. The possible decay modes of the  $Z$  boson  $q\bar{q}$  (70%),  $\ell^+\ell^-$  (10%) and  $\nu\bar{\nu}$  (20%) form final states which overlap with different SUSY signals. Also possible are  $e^+e^- \rightarrow We\nu$  and  $e^+e^- \rightarrow Zee$ , see Figs. 3.10e and f, which both involve photon radiation from one of the initial beam particles. The photon propagator contributes to the cross section with weight  $1/q^2$ :

$$\frac{1}{E_{\text{beam}}E_e(1 - \cos\theta_{\text{tag}})} \quad (3.9)$$

where  $E_e$  and  $\theta_{\text{tag}}$  are the scattered electron energy and polar angle. Thus events with low values of  $\theta_{\text{tag}}$  will have larger cross sections. The scattered electron is then more likely to go undetected down the beam-pipe leaving its characteristic missing transverse momentum.

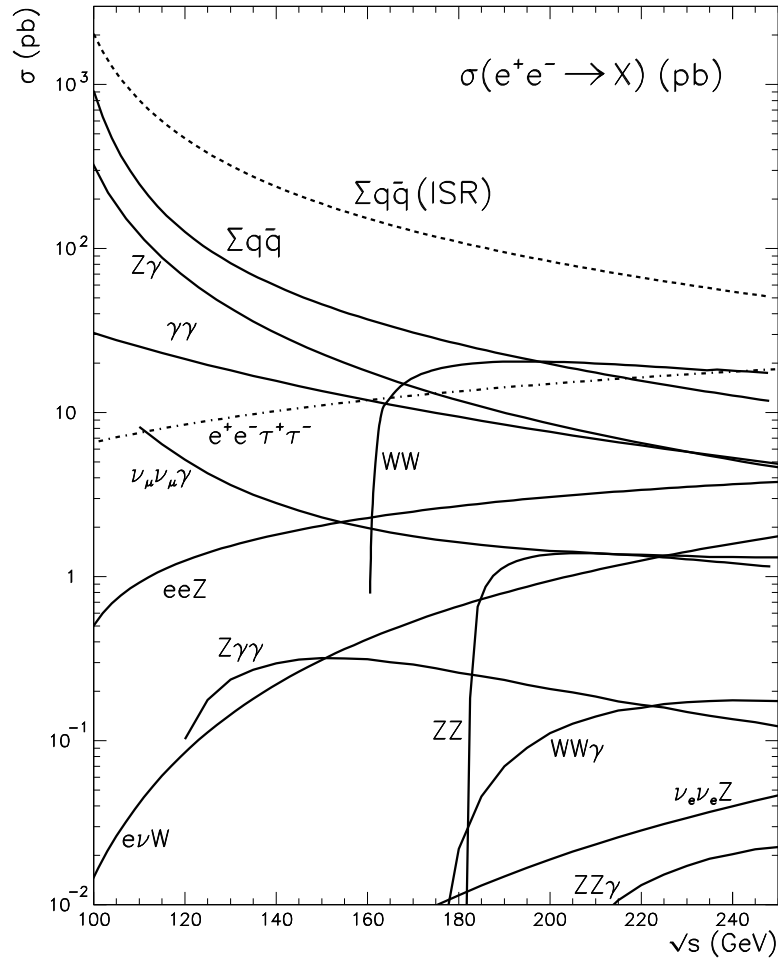


Figure 3.9: Cross sections for Standard Model processes as a function of the centre-of-mass energy. Taken from Boudjema and Mele in Ref. [36].

Conversely, the neutrino produced in  $We\nu$  processes arises from a virtual  $W$  whose propagator is given by

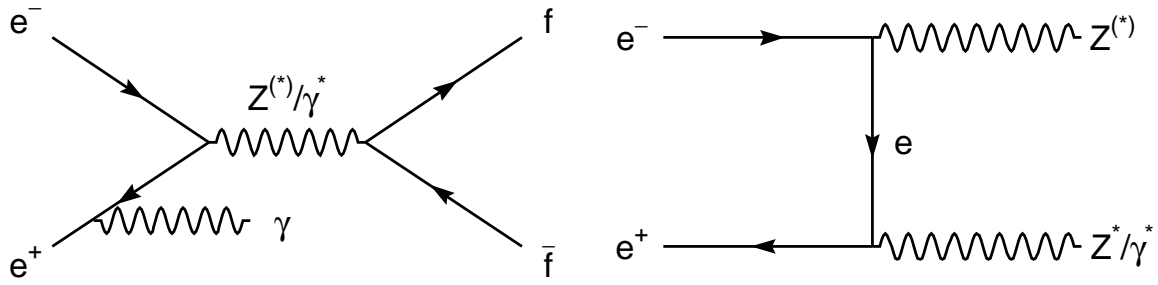
$$\frac{1}{E_{\text{beam}}E_{\nu}(1 - \cos\theta_{\nu}) - M_W^2} \quad (3.10)$$

This expression resonates for large neutrino scattering angles. So that characteristic  $We\nu$  events will have large missing momentum and a visible mass close to the  $W$  mass. Although the cross section for this type of process is around one pb, they constitute a difficult background to reject because six-lepton final states can be quite similar. For the same reasons,  $Zee$  events are typically identified by a very energetic electron, visible mass close to the  $Z$  mass and missing momentum.

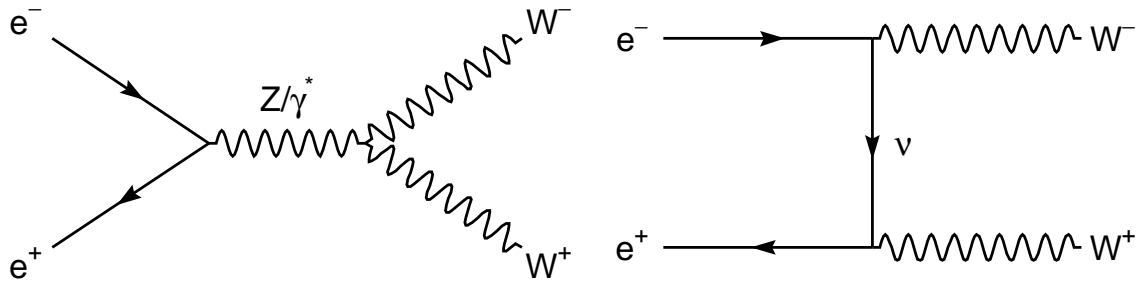
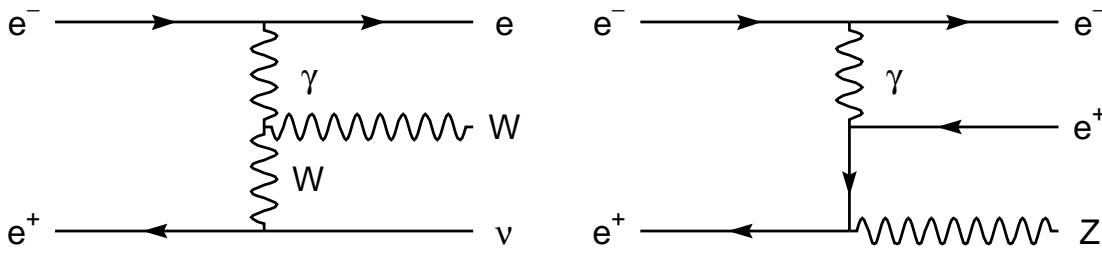
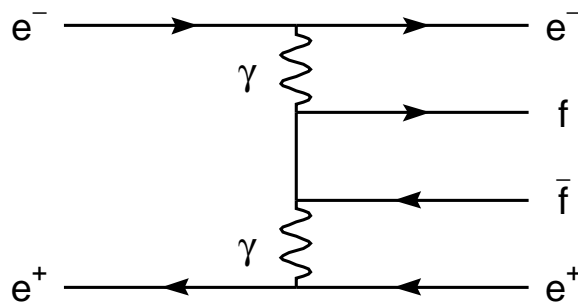
### Two-photon processes

LEP is not only an  $e^+e^-$  collider but also a high energy photon collider. Beam particles are constantly radiating photons which may interact with one another with high probability. The cross section for these  $e^+e^- \rightarrow e^+e^- ff$  processes is of the order of a nb. Figure 3.10g shows the relevant Feynman diagram. As discussed above, the majority of these radiative events are





(a) Two-fermion with ISR

(b)  $ZZ^*$  dominant contribution(c)  $WW$   $s$ -channel(d)  $WW$   $t$ -channel(e)  $We\nu$ (f)  $Zee$ 

(g) Two-photon

Figure 3.10: Feynman diagrams of SM background processes: (a) two-fermion, (b-f) four-fermion and (g) two-photon .

Process	189 GeV		196 GeV		202 GeV		206 GeV		MC
	N	$\sigma(\text{pb})$	N	$\sigma(\text{pb})$	N	$\sigma(\text{pb})$	N	$\sigma(\text{pb})$	Generator
ee	2000	966	1700	894	400	842	480	811	BHWIDE
$\mu\mu$	75	8.27	50	7.57	50	7.08	50	6.80	KORALZ
$\tau\tau$	75	8.21	50	7.54	50	7.04	50	6.74	KORALZ
$q\bar{q}$	400	99.40	600	89.74	125	84.54	125	80.60	KORALZ
WW	108	16.59	100	7.61	100	17.46	100	17.54	KORALW
$W e\nu$	15	0.66	20	0.75	20	0.83	20	0.88	PYTHIA
ZZ	40	2.76	50	2.85	50	2.84	50	2.81	PYTHIA
Zee	450	99.11	250	99.04	210	98.94	400	98.72	PYTHIA
$\gamma\gamma \rightarrow ee$	1200	3800	2000	3840	2000	3970	600	190 <sup>†</sup>	PHOT02
$\gamma\gamma \rightarrow \mu\mu$	1293	3550	2000	3620	2000	3660	600	185 <sup>†</sup>	PHOT02
$\gamma\gamma \rightarrow \tau\tau$	210	431	300	441	500	454	300	90.00 <sup>†</sup>	PHOT02
$\gamma\gamma \rightarrow q\bar{q}$	-	-	520	585	606	592	602	630	PHOT02

Table 3.2: Standard Model background processes analysed in the six-lepton topologies search. At each centre-of-mass energy, the number of produced events N in units of  $10^3$  and the corresponding cross section is given for each process. In the ‘tagged’ two-photon event generation it is required that the visible mass is greater than  $2.5 \text{ GeV}/c^2$  and the scattering polar angle greater than 5 mrad. The  $\gamma\gamma \rightarrow \ell\ell$  subsample at  $\sqrt{s} = 206 \text{ GeV}$  was required to have visible masses greater than  $10 \text{ GeV}/c^2$ , hence the lower cross sections (marked with <sup>†</sup>). The MC generators are BHWIDE [58], KORALZ [59], KORALW [60], PYTHIA [61] and PHOT02 [62].

produced when the two final state  $e^+e^-$  continue through the beam-pipe and are not detected (referred to as ‘untagged’ events). They can be distinguished by their low visible mass and particle multiplicity. Nevertheless if one of the final state electrons does appear in the detector, generally at very low angles, these events can fake SUSY signals with large missing energy.

### 3.3 Signal Selection

Two analyses have been designed to search for  $\tilde{l}_R \rightarrow l\chi$  and  $\tilde{l}_R \rightarrow l\tau\tilde{\tau}_1$  in the  $\tilde{\tau}_1$  NLSP scenario. No independent search has been made for either two- or three-body decay modes since both decays ultimately depend on the mass difference between the produced sleptons and the stau:  $\Delta m = m_{\tilde{l}_R} - m_{\tilde{\tau}_1}$ .

The case of large  $\Delta m$ , when  $\Delta m \gtrsim 10 \text{ GeV}/c^2$ , is the most favourable since the primary leptons are energetic, multiplicity is somewhat larger and these events contain large visible mass. When  $\Delta m$  is small,  $\Delta m \lesssim 10 \text{ GeV}/c^2$ , there are fewer identified leptons, greater missing momentum and much less visible mass.

#### 3.3.1 Description of the selections

The final state topology consists of four taus, two of them very energetic, and two leptons (electrons or muons) which might be soft if the mass difference between the sleptons and the stau is small. Only in the large  $\Delta m$  case is it possible to reject events containing fewer than two identified leptons, which is a very successful cut against two-fermion backgrounds. In the case of small  $\Delta m$  a more detailed study of the event is required and a procedure was devised in which the event is clustered into four tau jets using the Durham algorithm.

Six-lepton Selection for large $\Delta m$		
Preselection	Charged tracks	$4 < N_{\text{ch}} < 12$
	Identified leptons	$N_l \geq 2$
	Visible mass	$M_{\text{vis}} < 0.85\sqrt{s}$
Anti- $\gamma\gamma$	Visible mass	$M_{\text{vis}} > 25$
	Missing $p_t$	$\cancel{p}_t > 0.02\sqrt{s}$
Anti-4f	Hadronic mass	$M_{\text{vis}-2\ell} < 120$
	Neutral hadronic energy	$E_{\text{had}^0} < 0.17E_{\text{ch}}$ $E_{\text{had}^0} < 0.06\sqrt{s}$
Anti-2f,ZZ	Jet clustering	$y_{23} > 2 \times 10^{-3}$
		$y_{34} > 1 \times 10^{-4}$
Anti-WW	$q\bar{q}\ell\nu$ kinematics	$\chi_{\text{WW}} \geq 4.5$

Table 3.3: Selection criteria for six-lepton final states with large  $\Delta m = m_{\tilde{l}_R} - m_{\tilde{\tau}_1}$ . Masses are in  $\text{GeV}/c^2$ , momenta in  $\text{GeV}/c$ .

The selection criteria for the large  $\Delta m$  case are summarised in Tab. 3.3 and for small  $\Delta m$  in Tab. 3.4. The principal rejected background is cited beside the cut, although there are usually various backgrounds affected simultaneously.

The variables used in both the small and large  $\Delta m$  analyses are described below.

- The number of charged tracks  $N_{\text{ch}}$  and good tracks  $N_{\text{good}}$

The number of charged tracks, also known as *event multiplicity*, peaks at around 20 for four-fermion events. Signal events have much lower multiplicity. The number of good tracks (as defined in Sec. 2.6.1) restricts  $N_{\text{ch}}$  to tracks with a minimum of four TPC hits, small impact parameter and  $p_t > 2 \text{ MeV}/c$ .

- Number of identified leptons  $N_l$

Total number of electrons and muons in the event. Lepton identification was described in Sec. 2.6.3. This is a very sensitive parameter to  $\Delta m$ . In the large  $\Delta m$  case it helps in rejecting  $W\nu$ ,  $ZZ$ ,  $\gamma\gamma$ , and two-fermion processes which all peak at zero  $N_l$  if taus are involved.

- Variables  $M_{\text{vis}}$ ,  $\cancel{p}_t$ ,  $E_{\text{ch}}$ ,  $E_{\text{had}^0}$ ,  $M_{\text{had}}$ , and  $M_{\text{had}-2\ell}$

The visible mass  $M_{\text{vis}}$  is calculated by adding the energies and momenta of all energy flow particles in the event. The missing momentum is identical in magnitude and opposite in direction to the total momentum. Its projection onto the transverse plane defines  $\cancel{p}_t$ . Two-photon events have very small values of  $M_{\text{vis}}$  and  $\cancel{p}_t$  and these variables are very effective against such processes.  $E_{\text{ch}}$  is the contribution to the visible energy coming from charged particles,  $E_{\text{had}}$  from all hadrons and  $E_{\text{had}^0}$  from neutral hadrons. To cut against four-fermion events, the  $M_{\text{had}-2\ell}$  variable is defined as the total hadronic mass with the energy of the two most energetic leptons subtracted. The normalised  $M_{\text{vis}}$  against  $M_{\text{had}}$  distribution for the WW background is displayed in Fig. 3.11a. The small  $\Delta m$  signal is shown to have much less hadronic energy than four-fermion events and significantly less visible mass.

Six-lepton Selection for small $\Delta m$		
Preselection	Good tracks	$2 < N_{\text{good}} < 10$
	Visible mass	$M_{\text{vis}} < 0.10\sqrt{s}$
Anti- $\gamma\gamma$	Visible mass	$M_{\text{vis}} > 0.05\sqrt{s}$
	Missing $p_t$	$p_t^{\text{miss}} > 0.10\sqrt{s}$
Anti-4f	Hadronic mass	$M_{\text{had}} < 50$
	Hadronic mass	$M_{\text{had}-2\ell} < 0.25\sqrt{s}$
	Charged tracks in two tau jets	$N_{\text{ch}}^{\tau_1+\tau_2} < 6$
Anti- $\tau\tau$	$\tau$ jets with good tracks	$N_{\tau}^{\text{good}} > 2$
	Charged tracks not in tau jets	$N_{\text{ch}}^{\text{no}2\tau} \geq 2$
	Thrust	Thrust $< 0.95$

Table 3.4: Selection criteria for six-lepton final states with small  $\Delta m = m_{\tilde{l}_R} - m_{\tilde{\tau}_1}$ . Energies are in  $\text{GeV}/c^2$ , momenta in  $\text{GeV}/c$ .

- Cut values of the jet clustering algorithm  $y_{23}$  and  $y_{34}$

The Durham jet clustering algorithm [50] was described in Sec. 2.6.3. Here, the sensitive variables are  $y_{23}$  and  $y_{34}$ , which are the  $y_{\text{cut}}$  values (from Eq. 2.10) necessary to force the event from two to three jets and from three to four jets respectively. An example of the distribution of the  $\tau\tau$  and  $ZZ$  background along with the signal for the large  $\Delta m$  case is shown in Fig. 3.11b in the plane  $(y_{23}, y_{34})$ .

- $WW \rightarrow q\bar{q}\ell\nu$  chi-squared  $\chi_{\text{WW}}^2$

The kinematics of these events can be exploited to suppress the background by defining:

$$\chi_{\text{WW}}^2 = \left( \frac{m_{q\bar{q}} - m_{\text{W}}}{10 \text{ GeV}/c^2} \right)^2 + \left( \frac{m_{l\nu} - m_{\text{W}}}{10 \text{ GeV}/c^2} \right)^2 + \left( \frac{p_l + E_{\text{miss}} - 94 \text{ GeV}/c}{10 \text{ GeV}/c} \right)^2 \quad (3.11)$$

where  $m_{q\bar{q}}$  is the hadronic mass, i.e. the mass of the event after removing the leading lepton,  $m_{l\nu}$  is the mass of the leading lepton and the missing momentum,  $p_l$  is the momentum of the leading lepton and  $E_{\text{miss}} = \sqrt{s} - E_{\text{vis}}$  is the missing mass.  $WW$  events are likely to occur at small  $\chi_{\text{WW}}^2$ , and can therefore be rejected by requiring a minimum  $\chi_{\text{WW}}^2$  for events to be selected. See Fig. 3.12.

- Four-tau jets variables  $N_{\text{ch}}^{\tau_1+\tau_2}$ ,  $N_{\tau}^{\text{good}}$  and  $N_{\text{ch}}^{\text{no}2\tau}$

These variables are defined by forcing the event into four tau jets.  $N_{\text{ch}}^{\tau_1+\tau_2}$  is the number of charged tracks inside the two most energetic tau jets. It is used against  $W\ell\nu$  and  $ZZ$  backgrounds. Two very effective anti- $\tau\tau$  variables are:  $N_{\tau}^{\text{good}}$ , which is the number of tau jets that contain *good* tracks; and  $N_{\text{ch}}^{\text{no}2\tau}$ , the number of charged tracks not associated with any of the two most energetic tau jets.

- Thrust

The thrust is defined as:

$$\text{Thrust} = \max_{\hat{n}} \frac{\sum_i |\vec{p}_i \cdot \hat{n}|}{\sum_i |\vec{p}_i|} \quad (3.12)$$

where the sum runs over all reconstructed particles. The thrust ranges from 0.5 for ‘open’ (spherical) events to one for events with two well collimated jets. It is helpful in rejecting  $\tau\tau$  events with thrust values very close to one.

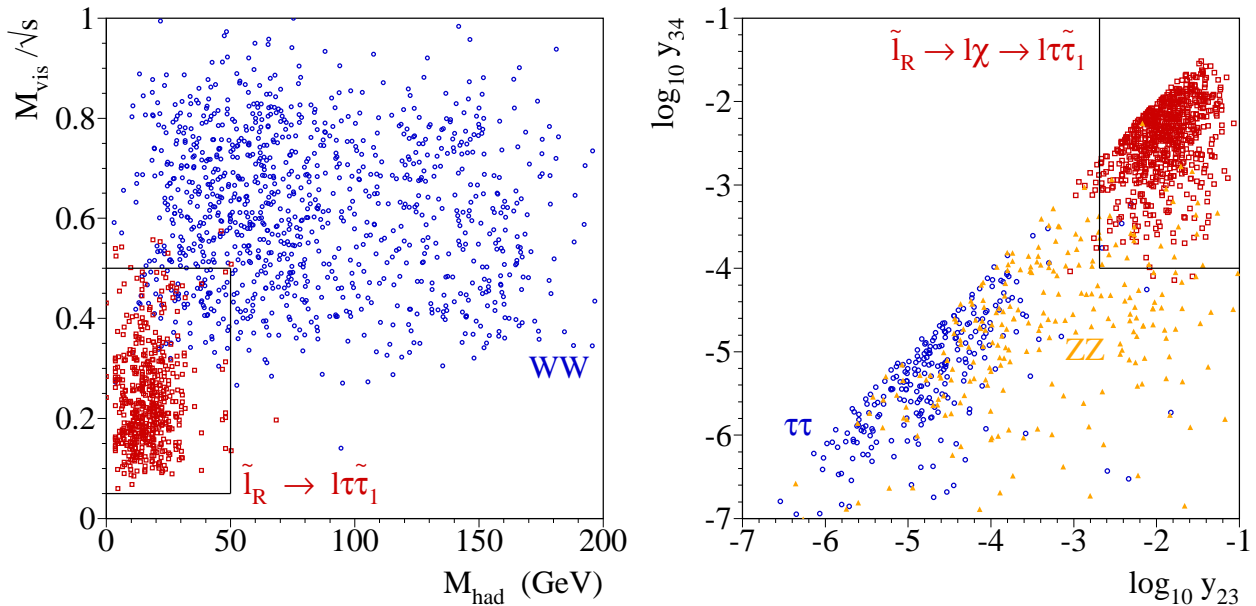


Figure 3.11: (a) Visible and hadronic mass distributions for WW background (open circles) and six-lepton signal points (three-body decay mode  $m_{\tilde{l}_R}:m_\chi:m_{\tilde{\tau}_1} = 97:123:94 \text{ GeV}/c^2$ ) in the small  $\Delta m$  selection after a subset of cuts has been applied. (b) Background distributions of  $\tau\tau$  (open circles) and ZZ (triangles) events in the  $(y_{23}, y_{34})$  plane before the cuts on those variables in the large  $\Delta m$  selection. The six-lepton signal is shown as empty squares, in a two-body decay mode:  $m_{\tilde{l}_R}:m_\chi:m_{\tilde{\tau}_1} = 95:87:73 \text{ GeV}/c^2$ .

The distributions of total background, data and signal after the preselection and anti- $\gamma\gamma$  cuts for the large and small  $\Delta m$  selections are shown in Figs. 3.12 and 3.13 for  $\sqrt{s} = 206 \text{ GeV}$  with an integrated luminosity of  $\mathcal{L} = 126.5 \text{ pb}^{-1}$ .

### 3.3.2 Optimisation

As can be seen in Fig. 3.12, to decide where to place the cut, one has to reach a compromise between the number of accepted background events, which should be small, and the efficiency in selecting signal events, which should be kept high. Such a compromise can be obtained analytically by means of the ‘ $\bar{\sigma}_{95}$  prescription’, described in Ref. [63].

The number  $N$  of expected events from any given process with production cross section  $\sigma$  if the experiment records  $\mathcal{L}$  integrated luminosity and the selection efficiency is  $\varepsilon$ , is given by

$$N = \varepsilon\sigma\mathcal{L} \quad (3.13)$$

Nevertheless, in a search experiment there are two independent contributions to the number of observed events: the expected background  $b$  and the expected signal  $s$ . The number of ‘candidate’ events  $n$  selected in the data after the selection has been applied can be described by Poisson statistics [64]:

$$P(n; s + b) = \frac{(s + b)^n}{n!} e^{-(s+b)} \quad (3.14)$$

which gives the probability to observe  $n$  events in the data if we expect  $s + b$ . If  $b$  is small

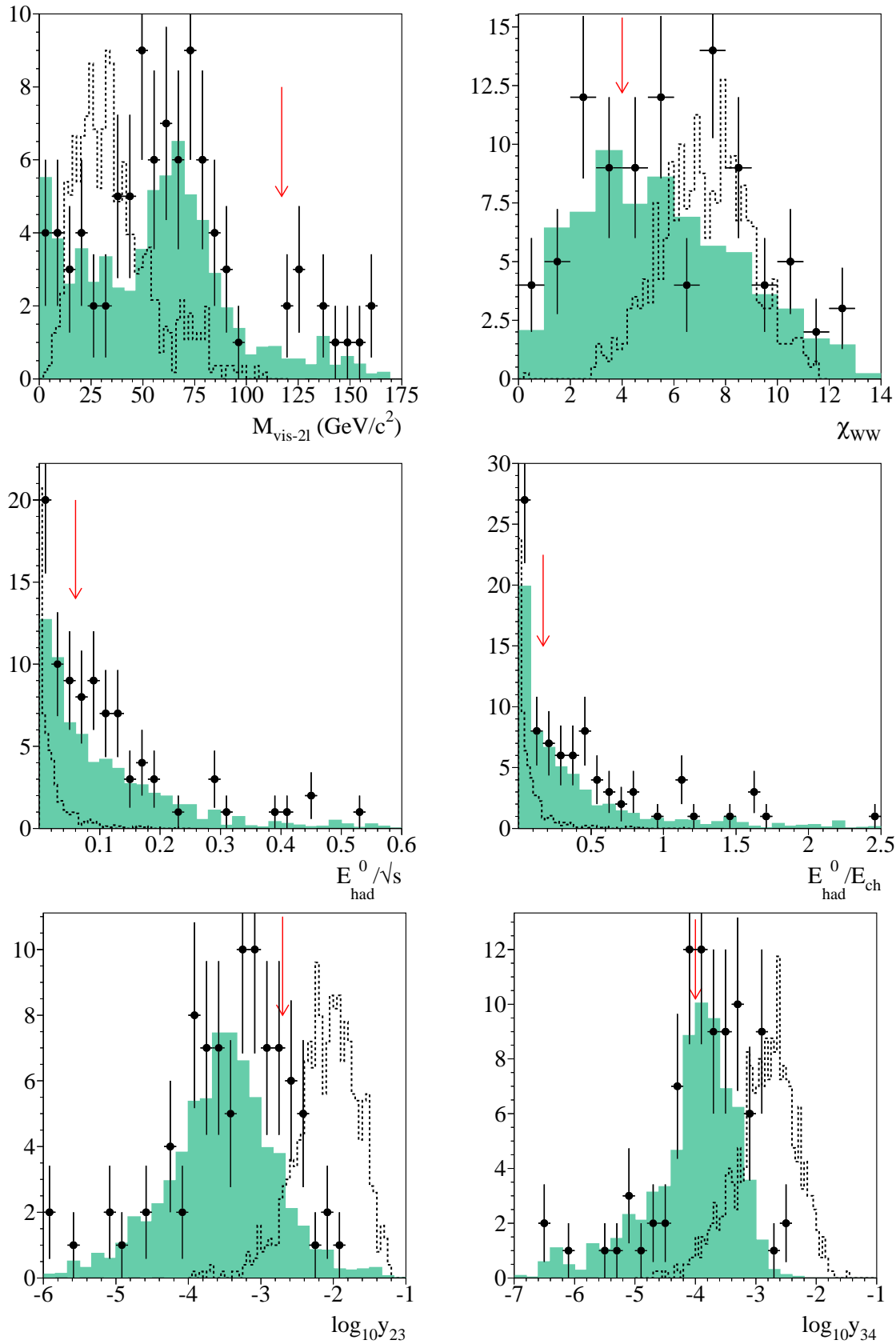


Figure 3.12: After applying the preselection and anti- $\gamma\gamma$  cuts, the distributions of the remaining variables used in the large  $\Delta m$  selection. The data (dots) at  $\sqrt{s} = 206 \text{ GeV}$  are compared to the background Monte Carlo (filled histograms). The dashed histograms show the signal distributions (for the values  $m_{\tilde{l}_R} : m_\chi : m_{\tilde{\tau}_1} = 95 : 87 : 73 \text{ GeV}/c^2$ ) in an arbitrary normalisation. The location of the cut is indicated with an arrow. The cut values were optimised and fixed before analysing the data, as described in Sec. 3.3.2.

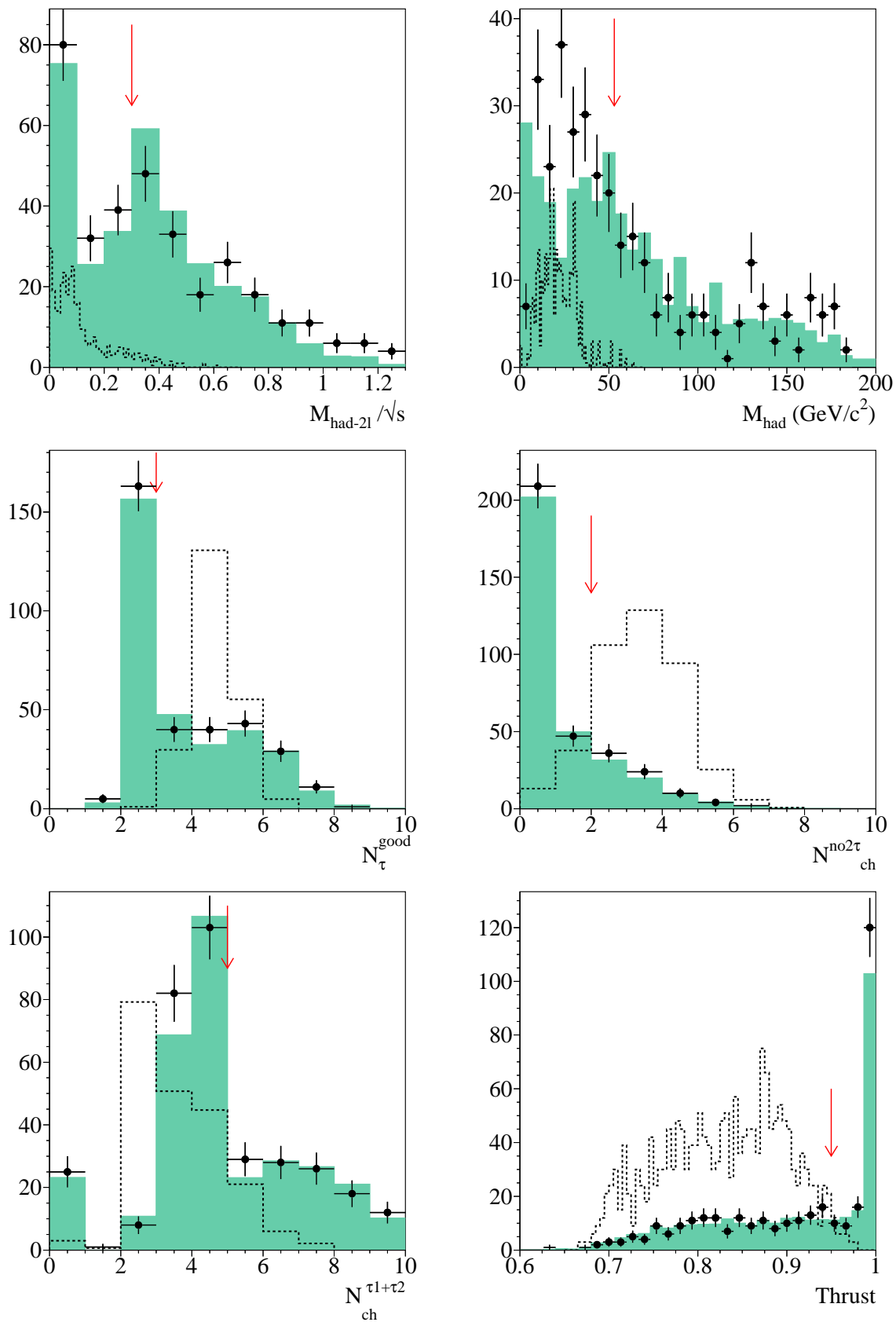


Figure 3.13: After applying the preselection and anti- $\gamma\gamma$  cuts, the distributions of the remaining variables used in the small  $\Delta m$  selection. The data (dots) at  $\sqrt{s} = 206 \text{ GeV}$  are compared to the background Monte Carlo (filled histograms). The dashed histograms show the signal distributions (for the values  $m_{\tilde{t}_R} : m_{\chi} : m_{\tilde{\tau}_1} = 97 : 123 : 94 \text{ GeV}/c^2$ ) in an arbitrary normalisation. The location of the cut is indicated with an arrow. The cut values were optimised and fixed before analysing the data, as described in Sec. 3.3.2.

and  $n$  is compatible with this expectation, then it is reasonable to assume that the observed candidate events come from background and not from signal. Thus an upper limit on the number of possible signal events can then be calculated. Usually the upper limit  $a_n$  for  $n$  candidates observed, is given with a 95% confidence level (C.L.), by solving:

$$P_n(a_n) = e^{-a_n} \sum_{k=0}^n \frac{a_n^k}{k!} = 0.05 \quad (3.15)$$

This is the probability to see  $n$  or less candidates if we expect  $a_n$ . The coefficients  $a_n = 3.00, 4.74, 6.30 \dots$  are the solutions to Eq. 3.15 with  $n = 0, 1, 2, \dots$ . For example, if no candidate events are observed in the data, every signal leading to 3.00 or more expected events is excluded at 95% C.L. This follows from the fact that the number of observed events from a signal process described by a Poisson distribution with a mean of three, has a 5% chance of fluctuating down to zero.

The selection procedure should be optimised to yield the signal efficiency and the background expectation corresponding to the best obtainable limit. As regards the background expectation, the position  $x$  of the cut on the discriminating variable being optimised is determined by minimising  $\bar{N}_{95}$ . This is the expectation value of  $a_n$  in the absence of any signal, i.e. if all candidates are background:

$$\bar{N}_{95}(x) = e^{-b(x)} \sum_{n=0}^{\infty} a_n \frac{b(x)^n}{n!} = e^{-b(x)} \left[ 3.00 + 4.74b(x) + 6.30 \frac{b^2(x)}{2!} + 7.75 \frac{b^3(x)}{3!} + \dots \right] \quad (3.16)$$

where  $x$  is the position of the cut to be optimised,  $b(x)$  is the expected number of background events surviving the cut and  $n$  is the number of observed events. The number  $b(x)$  is determined after all other cuts on the selection have been applied to the total background Monte Carlo sample. Equation. 3.16 is just the sum of the coefficients  $a_n$ , weighted by the Poisson probability to observe  $n$  events if  $b$  background events are expected.

However, if the number of expected background is large it is useful to recalculate the coefficients  $a_n$  taking into account the background. This procedure is referred to as ‘subtracting the background’, and generally only applies to well modelled and understood backgrounds. It is possible to only subtract one type of background events and not the total, i.e. only WW expected events or even only 80% of them if one is cautious about the systematic uncertainties in the estimation. In this case, if  $b_{sub}$  is the number of ‘subtracted’ background events, Eq 3.15 is modified to become [5]:

$$\frac{P_n(a_n + b_{sub})}{P_n(b_{sub})} = 0.05 \quad (3.17)$$

The expected limits when background is subtracted are stronger than the limits produced when background is not subtracted. Fig. 3.14 shows the different  $\bar{N}_{95}$  as a function of the expected background events, if background is fully subtracted or not. The background level in the selections developed in this chapter is low and there is no need to perform background subtraction.

Finally, the best position  $x$  for the cut on the variable under optimisation is such that the expected excluded cross section:

$$\bar{\sigma}_{95} = \frac{\bar{N}_{95}(x)}{\varepsilon(x)\mathcal{L}} \quad (3.18)$$

is minimal. While the numerator depends only on the number of accepted background events,



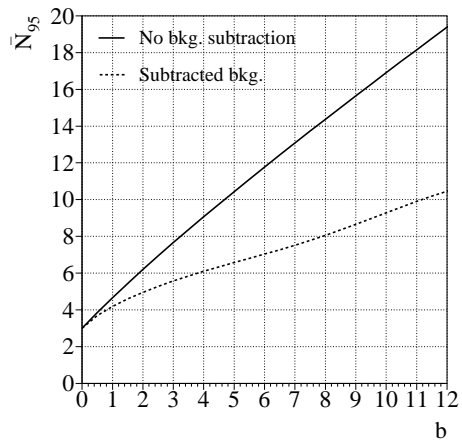


Figure 3.14: The expected limit on the signal events as a function of the expected background  $b$ , if the background is subtracted, and if no background subtraction is performed.

the denominator only depends (cumulatively) on the number of selected signal events. Thus the best possible limit is calculated at the Monte Carlo level without using the data. Figure 3.15 shows this process on two selected variables. First, the cut values are set approximately by looking at background and signal distributions as shown in Figs. 3.12 and 3.13. Once the chosen cuts give a good background rejection, the list of cuts is frozen and each one is optimised sequentially applying the others.

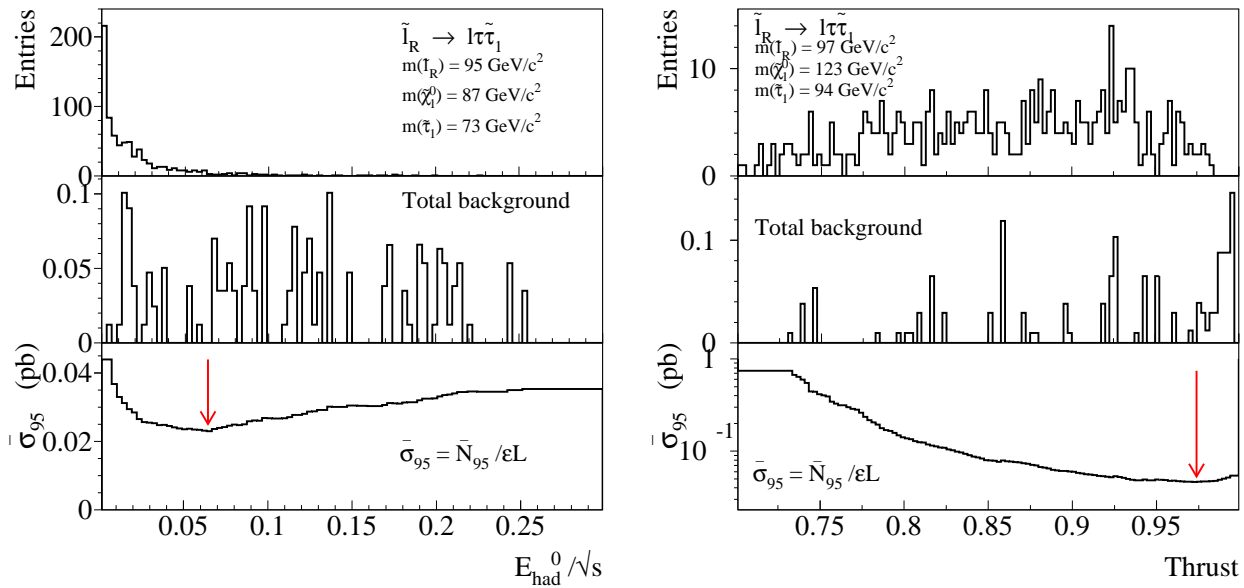


Figure 3.15: The optimisation procedure for the neutral hadronic energy in the small  $\Delta m$  selection (left) and the thrust in the large  $\Delta m$  selection (right). The signal distribution is shown on the upper third, the background in the middle and the minimised  $\bar{\sigma}_{95}$  at the bottom. All other cuts have been applied and the arrow indicates the optimal position of the cut on these variables.

### 3.3.3 Selection efficiencies

The main systematic uncertainties on the efficiencies come from the number of generated events in the simulated samples ( $\sim 3\%$ ). The total systematic uncertainty introduced by lepton identification variables has been estimated to be  $< 2\%$  [65]. Selected data events and background MC were compared to see any difference in the performance of the lepton identification algorithms. The estimators were shifted by the difference between data and MC, and new efficiencies were calculated to see the impact. These effects have been taken into account by conservatively reducing the selection efficiency by one standard deviation.

The generated signal data contained selectron and smuon events with the appropriate cross sections and branching ratios calculated by ISAJET. Thus no separation between selectron and smuon events in the selection efficiency is possible. The efficiency values are then for the topology as a function of  $\Delta m$  rather than independent measurements of the flavour of the event.

Signal events were only generated at 189, 206 and 208 GeV, thus an interpolation for intermediate energies was needed. A check on some signal efficiencies was performed at these intermediate energies to parametrise the efficiency as a function of  $\sqrt{s}$ . It was found that a linear interpolation between centre-of-mass values was appropriate since the calculated values were well within the systematic errors on the efficiencies of the generated points. Furthermore, only a few points had variations larger than 10% between the efficiency at 189 and 208 GeV.

Finally, the selection efficiencies are presented in Fig. 3.16 as a function of  $\Delta m = m_{\tilde{l}_R} - m_{\tilde{\tau}_1}$  for both two- and three-body signal points. Efficiencies greater than 30% are assured over the full range in  $\Delta m$ . The spread in the bands is due to the range in slepton masses generated from the kinematical limit down to  $70 \text{ GeV}/c^2$ . The spread in the large  $\Delta m$  selection when applied over two-body signal points arises from small or large slepton-neutralino mass differences. It is noticeable here that the same selection applied over three-body signal points shows no dependence on the virtuality of the neutralino.

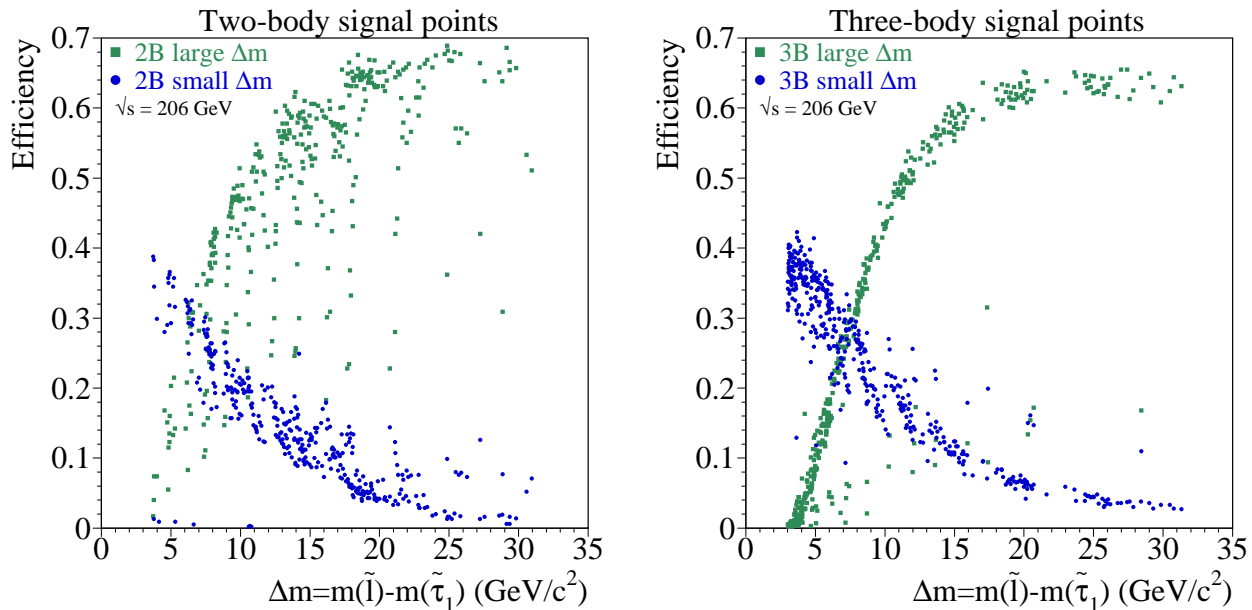


Figure 3.16: The efficiency of the small and large  $\Delta m$  selections as a function of  $\Delta m$  for all analysed signal points.

$\langle\sqrt{s}\rangle$	$\int \mathcal{L} dt$	6 $\ell$ small $\Delta m$		6 $\ell$ large $\Delta m$	
		data	bkg	data	bkg
189	173.6	0	0.73	0	0.25
192	28.9	1	0.12	1	0.04
196	79.9	0	0.34	0	0.12
200	87.0	1	0.37	0	0.13
202	44.4	1	0.14	0	0.23
205	79.5	0	0.34	0	0.12
206	126.5	0	0.54	0	0.18
208	7.8	0	0.03	0	0.01
TOT:	627.6	3	2.60	1	1.07

Table 3.5: After all cuts have been applied to the data and the background Monte Carlo the numbers of events for each selection at the different centre-of-mass energies. The P-values are:  $P(k \geq 3; b = 2.60, s = 0) = 0.48$  and  $P(k \geq 1; b = 1.07, s = 0) = 0.65$ .

## 3.4 Results

In this section the above selections are applied to the data and the background MC samples. The selected candidate events are briefly discussed and the significance of the observed results is described. Limits on the production cross section for selectrons and smuons are derived and conservative limits on the masses set.

### 3.4.1 Events selected in the data

The number of observed candidates in the data along with the SM background expectation at each centre-of-mass energy is presented in Tab. 3.5. Generated Monte Carlo samples for background processes were only available at the energies detailed in Tab. 3.2. To obtain an expected background value for intermediate energies, the two closest available values were scaled to the luminosity of the desired energy and linearly interpolated between them.

In the 628 pb<sup>-1</sup> of ALEPH data between 189 and 209 GeV, the search for six-lepton topologies with small  $\Delta m$  selects three events when 2.6 are expected and the search for large  $\Delta m$  finds one candidate event with 1.1 expected. What can one then say about the signal process under study? To quantify how likely it is to have signal production in the data, i.e.  $s \neq 0$  in Eq. 3.14, one can calculate the probability to find  $n$  events or more if background only was expected:

$$P(k \geq n; b, s = 0) = \sum_{k=n}^{\infty} \frac{b^k}{k!} e^{-b} = 1 - \sum_{k=0}^{n-1} \frac{b^k}{k!} e^{-b} \quad (3.19)$$

This is sometimes referred to as the confidence level (CL<sub>b</sub>) or P-value. 1-CL<sub>b</sub> measures the compatibility of the observation with the background hypothesis. As a convention, it is agreed that one has *discovered* a signal if 1-CL<sub>b</sub> is less than  $\sim 6 \times 10^{-7}$ . That is to say, the probability to observe such an unexpected result if the only source is the ‘known’ background, would have to be  $\sim 10^{-7}$  to be convinced that the signal is present in the data. The median expectation for pure background is 1-CL<sub>b</sub>=0.5. Therefore if CL<sub>b</sub> is smaller than 0.5 there is a deficit in the background expectation. The above equation yields a P-value of 0.48 and 0.65 for the small

$\sqrt{s}$	Run	Event	SM interpretation
191.6	50210	5122	Zee
199.3	51940	8969	WW
201.6	52100	3592	Zee
191.6	49630	10846	$\gamma\gamma q\bar{q}$

Table 3.6: Candidate events selected by the small  $\Delta m$  selection (first three) and the large  $\Delta m$  selection (bottom).

and large  $\Delta m$  selections, respectively. Thus the data is in perfect agreement with the expected value from the Standard Model<sup>3</sup>.

The composition of the expected background for the small  $\Delta m$  selection is as follows: WW and  $\gamma\gamma\tau\tau$  dominate with 40% each, the rest has equal contribution from  $\tau\tau$ ,  $W\nu$  and Zee. In the search for large  $\Delta m$  topologies, the dominant background is ZZ with 35%, followed by  $q\bar{q}$ ,  $\tau\tau$  and Zee. All other background sources are completely eliminated.

The four selected data events are all compatible with SM sources as listed in Tab. 3.6. They are displayed in Fig. 3.17. The event selected by the large  $\Delta m$  selection at 192 GeV, shown in Fig. 3.17a, has two identified electrons. One is isolated with momentum 6.5 GeV/ $c$  and the other has 66 GeV/ $c$  momentum, with 27 GeV of hadronic energy in a cone of 30° around its direction. There is large missing momentum in the  $z$  direction, suggesting that one particle went through the beam-pipe. It could therefore be a  $\gamma\gamma$  event with two low multiplicity jets, one of them with a semileptonic decay. Of the three candidate events selected by the small  $\Delta m$  selection, the two recorded at 192 and 202 GeV, in Figs. 3.17b and d, present a very energetic electron of 15 and 66 GeV respectively, and large missing longitudinal momentum. Both invariant masses are compatible with  $m_Z$ , at 59 and 98 GeV/ $c^2$  respectively. Therefore they are possibly Zee events where one of the electrons goes undetected. Finally, the event at 200 GeV shown in Fig. 3.17c is probably a WW event with a nuclear interaction very close to the IP. There is an identified electron with 50 GeV energy and a three-prong tau candidate with an invariant mass of 1.9 GeV/ $c^2$ , suggesting  $WW \rightarrow e\nu\tau\nu$ . The remaining two tracks have together an invariant mass of 0.1 GeV/ $c^2$ .

### 3.4.2 Limits on slepton production

In the absence of any evidence for a signal, it is possible to constrain the parameters of the theory that would produce such a signal. However, the statistical nature of the counting experiment makes it impossible to rule out with 100% certainty any hypothetical process. Thus all limits quoted here will be expressed at 95% confidence level, which should be understood as: ‘if the experiment were to be performed again, the probability to obtain a result which is in as bad or in worse agreement between the expectation and the observation is less than 5%’.

---

<sup>3</sup> Of course this argument relies heavily on the background estimation, so it should be used quoting estimation errors. In the case of a 10% fluctuation in the background expectation, the above results for the P-value would still be compatible with the background only hypothesis.

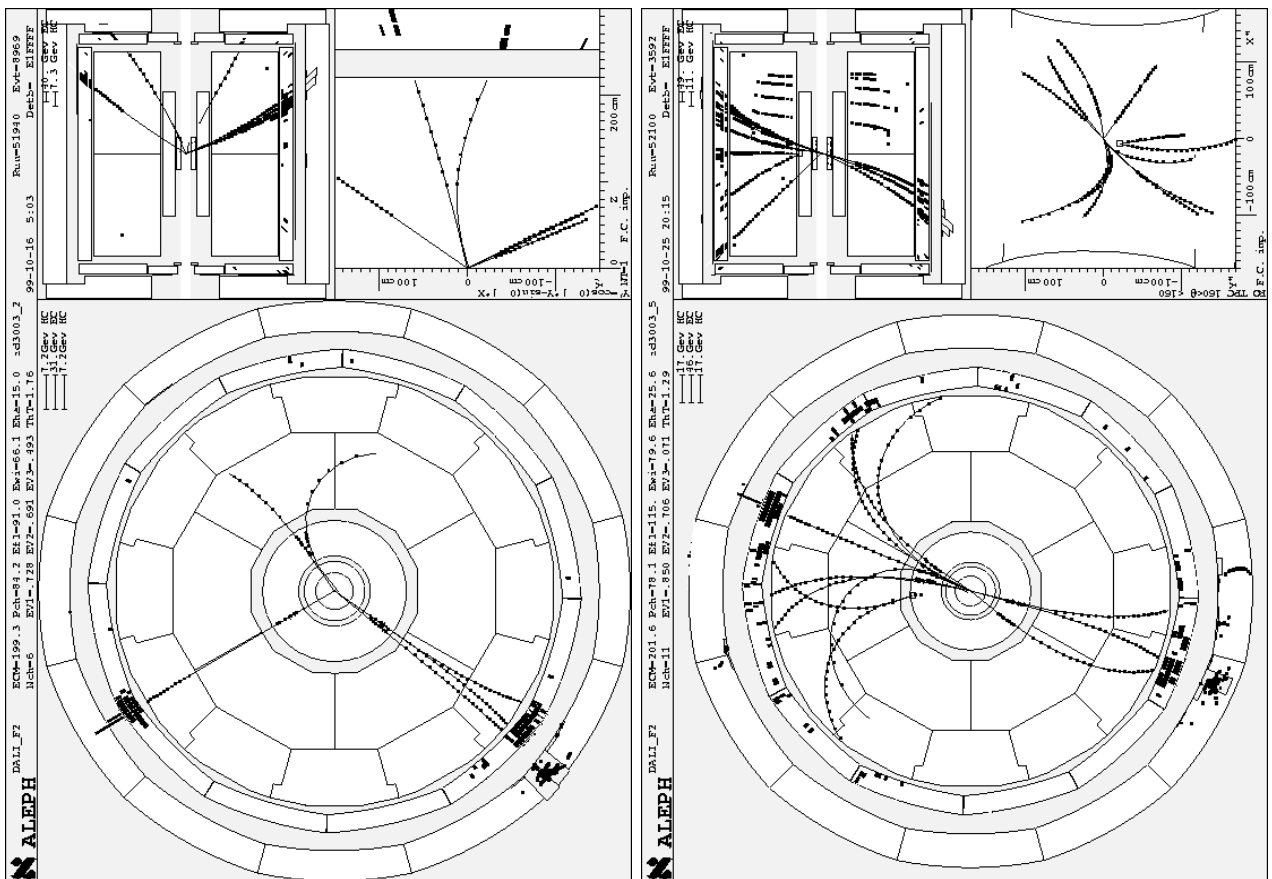
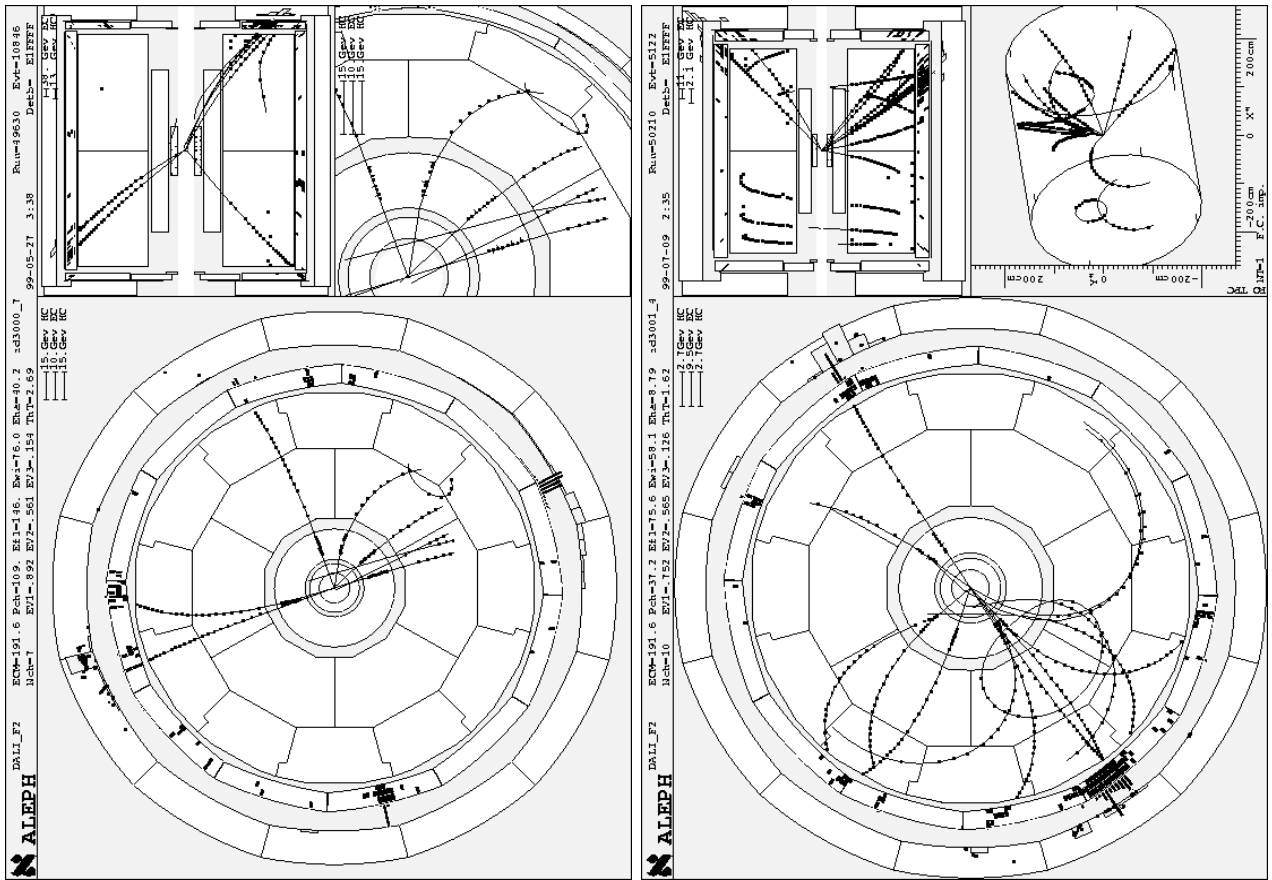


Figure 3.17: Candidate events.

## Mass limits

The ratio

$$\text{CL}_s = \frac{\text{CL}_{s+b}}{\text{CL}_b} = \frac{\prod_i P(k \leq n; s+b)}{\prod_i P(k \leq n; b)} = \frac{\prod_i \sum_{k=0}^n e^{-(s+b)} (s+b)^k / k!}{\prod_i \sum_{k=0}^n e^{-b} b^k / k!} \quad (3.20)$$

is used to derive a lower limit on the hypothetical slepton mass.  $\text{CL}_b$  was defined in Eq. 3.19 and  $\text{CL}_{s+b}$  follows from the same equation when the number of expected signal events  $s$  is also included.  $\text{CL}_{s+b}$  is thus a measure of the compatibility with the signal+background hypothesis. The product over  $i$  channels makes reference to the different energy bins where data was taken. Thus  $n$ ,  $s$  and  $b$  change with the centre-of-mass energy  $i$  (see Tab. 3.5). To perform the calculation of the observed  $\text{CL}_s$  and the average expected without looking at the data, the FORTRAN package described in Ref. [66] was used.

The limits on the masses are set when the confidence limit ( $\text{CL}_s$ ) reaches 0.05, i.e. the probability that a signal-like experiment is less compatible with the signal than what is observed is below 5%. The confidence level for the different selections as a function of the selectron and smuon masses is shown in Fig. 3.18.

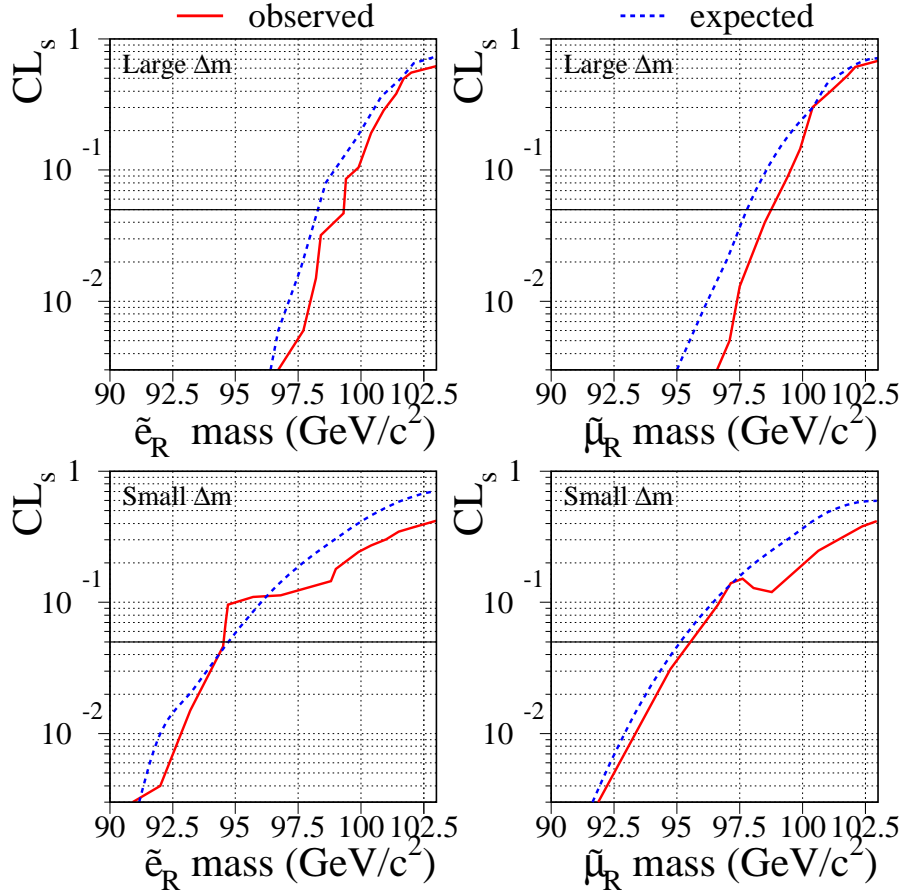


Figure 3.18: Lower mass limits for selectrons and smuons from the two six-lepton selections. The large  $\Delta m$  selection confidence level  $\text{CL}_s$  is plotted in the upper row for selectron and smuon masses. The small  $\Delta m$  selection in the lower plots. Solid lines give the observed limit and dashed lines the average expected limit for background.

The limits on the slepton masses derived from the above confidence level are the following:

Large $\Delta m$ :	$m_{\tilde{e}} > 99 \text{ GeV}/c^2$	$m_{\tilde{\mu}} > 98 \text{ GeV}/c^2$
Small $\Delta m$ :	$m_{\tilde{e}} > 94 \text{ GeV}/c^2$	$m_{\tilde{\mu}} > 95 \text{ GeV}/c^2$

### Cross section limits

The calculation of a model independent cross section limit is somewhat more problematic given the span of centre-of-mass energies of the recorded data. To provide a combined limit, the respective luminosities must take into account the appropriate phase space for slepton production at each energy. The best approach for the combination is to scale the luminosity of the lower energy data by the ratio of the cross section at that energy to the cross section at  $\sqrt{s} = 208 \text{ GeV}$ . Thus the upper limit on the production cross section at the 95% C.L. can be written as:

$$\sigma_{95} = \frac{N_{95}}{\sum_{\sqrt{s}} \varepsilon(\sqrt{s}) \mathcal{L}(\sqrt{s}) \frac{\sigma(\sqrt{s})}{\sigma(208)}} \quad (3.21)$$

where  $N_{95} = 3.00, 4.74, 6.30 \dots$  from Eq. 3.15 depends only on the number of observed candidates when no background subtraction is necessary as is the case here. This expression takes into account the variation of the efficiency with  $\sqrt{s}$  as well as the change in luminosity if the considered slepton mass cannot be produced at that centre-of-mass energy. Using the ratio of cross sections to perform this adjustment in the phase space, is more accurate than using the simple  $\beta^3/s$  factor expected for sfermion production. Cross sections are calculated taking into account radiative corrections and other model dependent factors whereas the  $\beta^3/s$  scale is only valid at the Born level and for  $s$ -channel production. Clearly,  $\sigma_{95}$  has a dependence on the sparticle mass through the efficiency function and the cross sections. Thus for every possible slepton mass a value of  $\sigma_{95}$  is calculated. If the production cross section for a slepton at that mass is greater than the upper limit  $\sigma_{95}$ , that test mass and more generally the model that produced that slepton are excluded. Or inversely, one can say that only those models of the theory which produce sleptons with  $\sigma < \sigma_{95}$  are possible and still realisable in Nature.

Figure 3.19 shows the excluded cross sections as shaded areas determined by the upper limit  $\sigma_{95}$  for the six-lepton selections as a function of the hypothetical slepton mass. The minimal possible production cross section is also shown.

The interpretation of these results in the wider context of GMSB models is left for Chapter 5, where these limits and the limits imposed by other searches in the GMSB framework are analysed in the most general scenario.

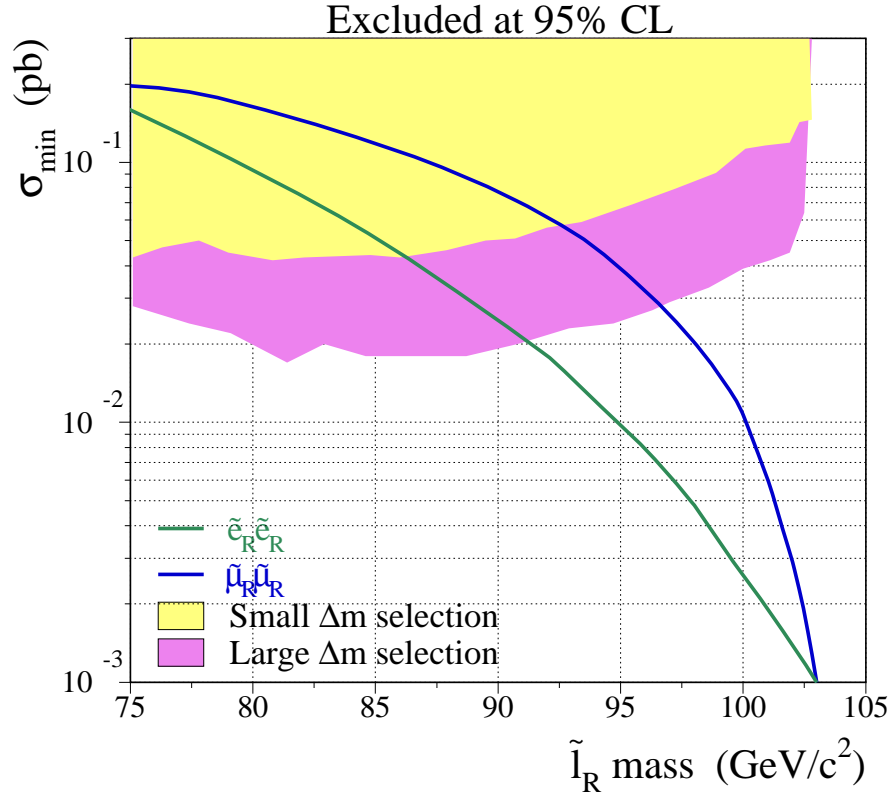


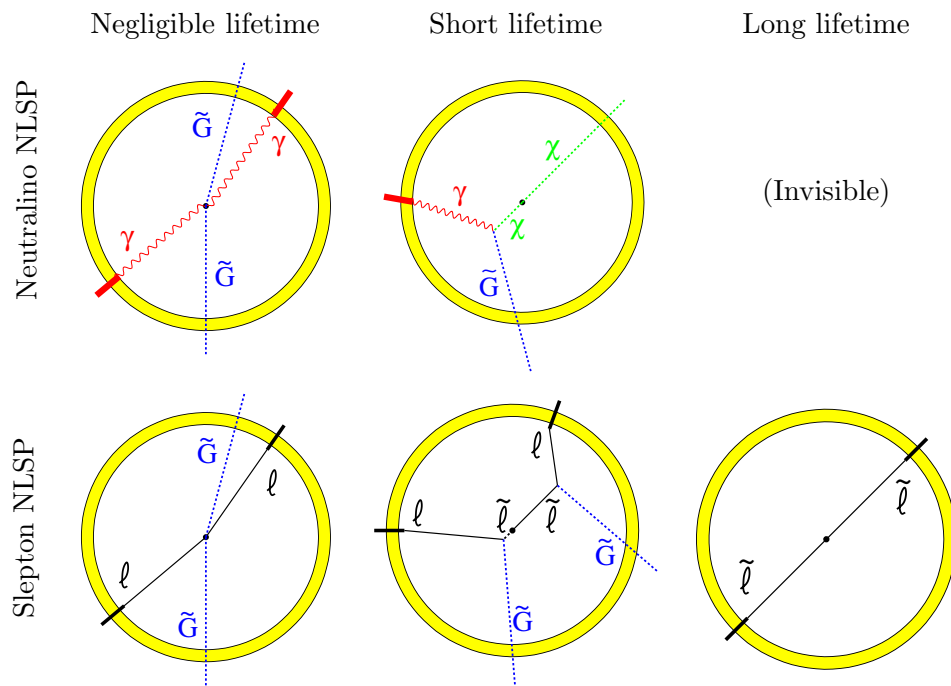
Figure 3.19: 95% C.L. excluded cross section areas as a function of the slepton mass for the small  $\Delta m$  (light shaded area) and large  $\Delta m$  (dark shaded area) selections. The minimum production cross section for pairs of selectrons and smuons covering all possible six-lepton topologies is also shown for comparison.



# Chapter 4

## GMSB searches and present limits

Gauge mediated Supersymmetry breaking models could be realised at LEP in the form of many different topologies. These arise from just two factors: whether the NLSP is the lightest neutralino or the lightest stau, and whether the NLSP lifetime is negligible (prompt decays), short (decays inside the detector) or long (decays outside the detector). Searches to cover all possible NLSP types and lifetimes, considering also indirect production, have been developed by other members of the ALEPH collaboration and are described here. Their results will be used in the next chapter to constrain possible GMSB models. The possible final states under study are: two energetic photons, non-pointing single photons, two acoplanar leptons, large impact parameter leptons, detached slepton decay vertices, heavy stable charged sleptons and multi-leptons plus missing energy final states.



NLSP	$e^+e^- \rightarrow$	Decay mode	Signal	$\lambda = c\tau\gamma\beta$	Expected topology
$\chi$	$\chi\chi$	$\chi \rightarrow \gamma\tilde{G}$	$\gamma(\gamma) \cancel{E}$	$\lambda \ll \ell_{\text{det}}$ $\lambda \sim \ell_{\text{det}}$ $\lambda \gg \ell_{\text{det}}$	Acoplanar photons Non-pointing photon [Indirect search]
	$\tilde{\ell}\tilde{\ell}$	$\tilde{\ell} \rightarrow \ell\chi \rightarrow \ell\gamma\tilde{G}$	$\ell\ell\gamma\gamma \cancel{E}$	$\lambda \ll \ell_{\text{det}}$ $\lambda \sim \ell_{\text{det}}$	Leptons and photons Leptons and displaced $\gamma$
co- $\tilde{\ell}$ or $\tilde{\tau}_1$	$\tilde{\ell}\tilde{\ell}$	$\tilde{\ell} \rightarrow \ell\tilde{G}$	$\ell\ell \cancel{E}$	$\lambda \ll \ell_{\text{det}}$ $\lambda \sim \ell_{\text{det}}$ $\lambda \gg \ell_{\text{det}}$	Acoplanar leptons Kinks and large $d_0$ Heavy charged particles
	$\chi\chi$	$\chi \rightarrow \tilde{\ell}\tilde{\ell} \rightarrow \ell\ell\tilde{G}$	$\ell\ell'(\ell\ell') \cancel{E}$	$\lambda \ll \ell_{\text{det}}$ $\lambda \sim \ell_{\text{det}}$	Four leptons Kinks and large $d_0$
$\tilde{\tau}_1$	$\tilde{l}_R\tilde{l}_R$	$\tilde{l}_R \rightarrow \ell\tau\tilde{\tau}_1$	$\tau\tau(\ell\tau\tau) \cancel{E}$	$\lambda \ll \ell_{\text{det}}$	Six leptons

Table 4.1: All possible final state topologies according to the NLSP scenario and decay length  $\lambda$ . Particles in brackets may be soft or even undetected. Only  $\ell\ell\gamma\gamma \cancel{E}$  signals were not studied in the 189 – 209 GeV ALEPH data set.

## 4.1 Description of GMSB topologies

There is a breadth of topologies to study at LEP2 to cover all possible GMSB scenarios if one considers not only the NLSP type but also its lifetime [32]. Table 4.1 lists all possible searches in the different NLSP scenarios.<sup>1</sup>

Depending on the gravitino mass, the following topologies are expected:

- If the gravitino mass is below a few  $\text{eV}/c^2$ , the NLSP decays immediately after its production before the tracking subdetectors. In the neutralino NLSP scenario, two very energetic photons and missing energy are expected from direct neutralino production. If the sleptons are accessible, the cascade decay  $\tilde{\ell} \rightarrow \ell\chi$  with two photons and two leptons in the final state is a background free search. Nevertheless, two photon searches alone are able to exclude most of the neutralino NLSP parameter space in the ‘no lifetime’ region. In the slepton NLSP scenario, if sleptons are directly produced, SUGRA searches for two acoplanar<sup>2</sup> leptons can be used. Also cascade decays  $\chi \rightarrow \tilde{\ell}\tilde{\ell}$  are possible here, if the neutralino pair-production is kinematically allowed. Indeed, its production cross section will be greater than the slepton production cross section because of the  $\beta^3/s$  suppression factor on scalars. Finally, in the purely stau NLSP case, where selectrons and smuons are heavier than the stau, final states with two leptons and four taus are possible, as described in the preceding chapter.
- For  $m_{\tilde{G}}$  between a few  $\text{eV}/c^2$  and a few hundred  $\text{eV}/c^2$ , the NLSP will decay somewhere inside the detector (see Fig. 1.7) The decay products of the NLSP, either photons or leptons, will present large impact parameters or in the case of slepton NLSP when the

<sup>1</sup>OPAL and DELPHI also include searches for charginos in  $e^+e^- \rightarrow \chi_1^+\chi_1^- \rightarrow W^*\chi W^*\chi$  and  $\chi_1^+\chi_1^- \rightarrow \tilde{\nu}\tilde{\nu}$  with the NLSP decaying inside the detector [53]. But charginos may only be produced at LEP2 if  $M_m$  is very large. DELPHI has also searched for sgoldstino production and decay to  $\gamma\gamma\gamma$  and  $gg\gamma$ , and is able to set limits on the scale of SUSY breaking  $\sqrt{F_0}$  from this search [67].

<sup>2</sup>The acoplanarity  $\alpha$  is defined as the angle between the projections of two tracks into the transverse plane.

slepton is reconstructed in the tracking volume, the slepton and the lepton will form a ‘kinked’ track.

- For  $m_{\tilde{G}}$  above a few hundred eV/ $c^2$  the NLSP is stable for detector searches as it decays outside the detector volume. Only in the slepton NLSP case are direct searches possible: highly ionising back-to-back tracks are formed by slow moving sleptons. The situation in the neutralino NLSP reverts to the usual SUGRA phenomenology with a neutralino LSP escaping the detector, and only searches for indirect production of neutralinos are possible.

## 4.2 Searches for neutralino NLSP

Searches for  $\chi \rightarrow \gamma\tilde{G}$  rely on good photon identification. The highly segmented ALEPH ECAL makes it possible to measure the energy of isolated photons with an excellent resolution (Eq. 2.4). The main SM background source for this search is  $e^+e^- \rightarrow \nu\bar{\nu}$ , from diagrams with  $s$ -channel Z exchange or  $t$ -channel W exchange and one or two initial state radiation (ISR) photons. The invariant missing mass  $M_{\text{miss}}^2 \equiv (p_{e^+} + p_{e^-} - p_{\gamma_1} - p_{\gamma_2})^2$ , will thus have a pronounced peak at the Z mass and a long tail from the contribution of the W exchange.

The simulation of the background was performed using the KK generator [68], which was checked with an independent generator NUNGPV [69]. Signal processes were simulated using SUSYGEN [56].

### 4.2.1 Acoplanar photons

Each neutralino is produced with the beam energy  $\sqrt{s}/2$ , and since the gravitino is nearly massless and the decay  $\chi \rightarrow \gamma\tilde{G}$  is isotropic in the neutralino rest frame, the photon energy spectrum is expected to be flat  $E_{\text{min}} < E_{\gamma_1}, E_{\gamma_2} < E_{\text{max}}$ , with [32]:

$$E_{\text{max,min}} = \frac{1}{4} \left( \sqrt{s} \pm \sqrt{s - 4m_\chi^2} \right) \quad (4.1)$$

Thus imposing a threshold cut of  $E_{\text{min}} = 37$  GeV on the energy of the least energetic photon is very effective against the SM background, where the photons are produced via bremsstrahlung. The cut value was optimised for models with a pure bino neutralino and  $m_{\tilde{e}_R} = 1.1m_\chi$  [70]. The preselection procedure is based on the requirement of two acoplanar photons and cuts to reduce the  $e^+e^- \rightarrow \gamma\gamma(\gamma)$  events, like  $\alpha < 177^\circ$  and no additional energy greater than 1 GeV. To reduce the doubly radiative Bhabha events  $e^+e^- \rightarrow e^+e^-\gamma\gamma$ , a cut on the total transverse momentum of the photon system  $p_t$  is very effective. The complete set of cuts for this search is summarised in Tab. 4.2. The distribution of data and background for the missing energy and  $E_{\gamma_2}$  is shown in Fig. 4.1 before the cut on  $E_{\gamma_2}$ .

A total of four candidate events are selected in the data while 4.9 are expected from background. After full subtraction of the expected background, a 95% C.L. upper limit on the neutralino production cross section can be set for an NLSP laboratory lifetime of less than 3 ns, as shown in Fig. 4.1. Systematic uncertainties, mainly due to the photon reconstruction efficiency and the level of background, only change the cross section limit by less than 1% [34].

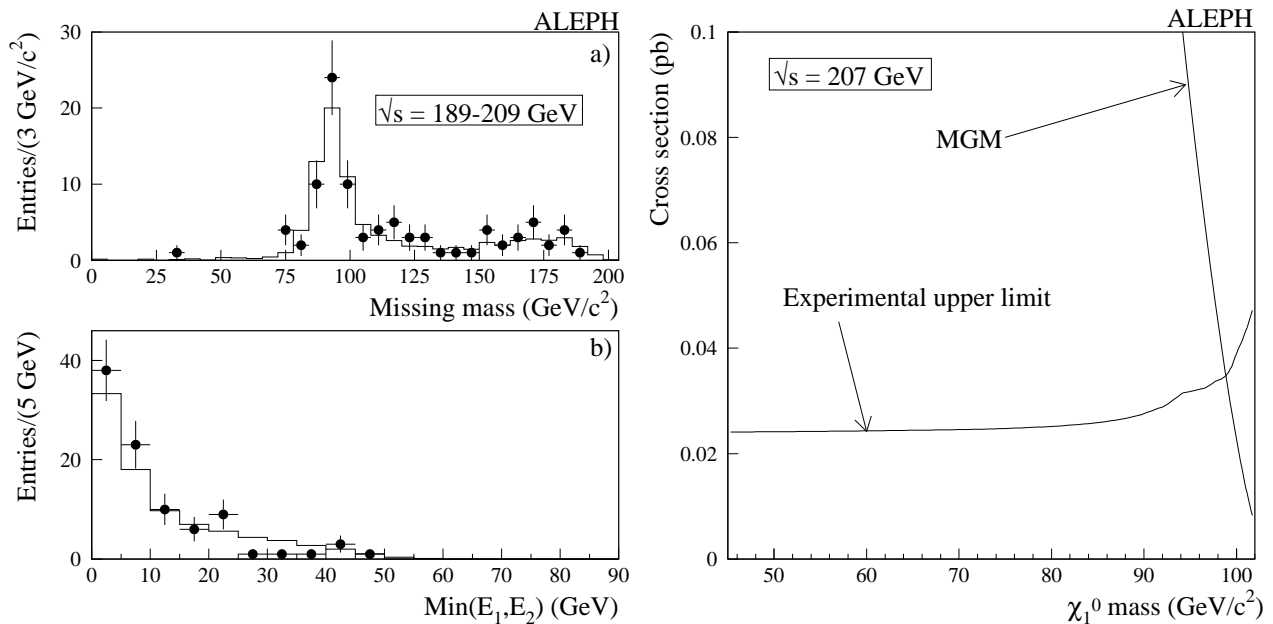


Figure 4.1: The distributions of (a) the invariant mass of the system recoiling against the photon candidates and (b) the energy of the second most energetic photon, for the two photon search before the cut on the energy of the second most energetic photon. The SM expectation is the histogram and dots with errors are data. On the right, the 95% confidence level upper limit on the  $e^+e^- \rightarrow \chi\chi$  cross section in the neutralino NLSP scenario when the neutralino lifetime is negligible:  $\tau_\chi < 3$  ns. The expected cross section for the MGM model [70] (where the neutralino is purely bino and  $m_{\tilde{e}_R} = 1.1m_\chi$ ) is also shown. From Ref. [34].

### 4.2.2 Non-pointing photons

If the neutralino NLSP has medium decay length such that it can decay inside the detector, the most probable topology is a single photon which does not point to the interaction region. Therefore one of the produced neutralinos is more likely to escape the detector while the other decays before the ECAL. Here, the calorimeter granularity is crucial to be able to reconstruct the shower axis and thus accurately determine the displaced vertex distance to the IP. The basic selection criteria are to select only one identified photon with an impact parameter greater than 40 cm in the acceptance region  $|\cos\theta_\gamma| < 0.95$  and require no charged tracks (which excludes photon conversions). To eliminate radiative Bhabha events  $e^+e^- \rightarrow e^+e^-\gamma$ , there must be no energy deposited within  $14^\circ$  of the beam axis and less than 1 GeV in additional energy. To further reduce ECAL noise and cosmic muons, at least 40% of the photon energy must be recorded in the ECAL, there must be no activity in the muon chambers or within a transverse distance of 15 cm from the photon candidate in the ECAL.

The efficiency for this selection reaches a maximum of 10% at neutralino decay lengths of around 8 m. After all cuts, 0.8 events are expected from  $e^+e^- \rightarrow \nu\bar{\nu}\gamma$  and  $0.2 \pm 0.2$  events from cosmic rays and detector noise. Two events are selected in the data.

A limit on the neutralino mass as a function of its decay length is obtained under the assumptions of the MGM (minimal gauge mediated) model [70], with a maximum of  $98.8$  GeV/c<sup>2</sup> at 95% C.L. when both two-photon and non-pointing photon searches are included. As will be seen in the next chapter, this limit is reduced to  $\sim 94$  GeV/c<sup>2</sup> if the conditions of the MGM model are removed. The CDF detector at the Tevatron recorded an event with two opposite

Two photons	Non-pointing photon
$N_\gamma=2$ or ( $N_\gamma \geq 3$ and $E_{\text{miss}} > 0.4\sqrt{s}$ ) Accept conversions Acoplanarity $< 177^\circ$ $E_{\gamma_2} \geq 37 \text{ GeV}$	$N_\gamma=1$ and $d_0 > 40 \text{ cm}$ No conversions $E_{14} = 0$ $E_{\text{ECAL}} \geq 0.4E_\gamma$ and $E_{\text{ECAL}}^{15 \text{ cm}} = 0$
Additional energy $< 1 \text{ GeV}$ $ \cos \theta_\gamma  < 0.95$ Total $p_t > 0.0375E_{\text{miss}}$	

Table 4.2: List of cuts for the neutralino NLSP scenario in the no lifetime case (two acoplanar photons and  $\cancel{E}$ ) and the intermediate lifetime case (non-pointing photon).

charge electrons with transverse energy of 63 and 36 GeV, two photons of 36 and 30 GeV and a total missing transverse energy of 55 GeV [71]. This type of signature has a very low background expectation ( $\sim 10^{-3}$ ) and could be interpreted as a GMSB process in the neutralino NLSP scenario:  $q\bar{q} \rightarrow \tilde{e}_R\tilde{e}_R \rightarrow e^+e^-\chi\chi \rightarrow e^+e^-\gamma\gamma\tilde{G}\tilde{G}$  [72]. At LEP, the plane  $(m_{\tilde{e}_R}, m_\chi)$  is directly probed by the direct production of neutralinos through the selectron  $t$ -channel exchange, thus the searches described above are sensitive to the same parameter space. Figure 4.2 shows the excluded area in that plane. The region favoured by the CDF event is now completely excluded with 95% C.L.

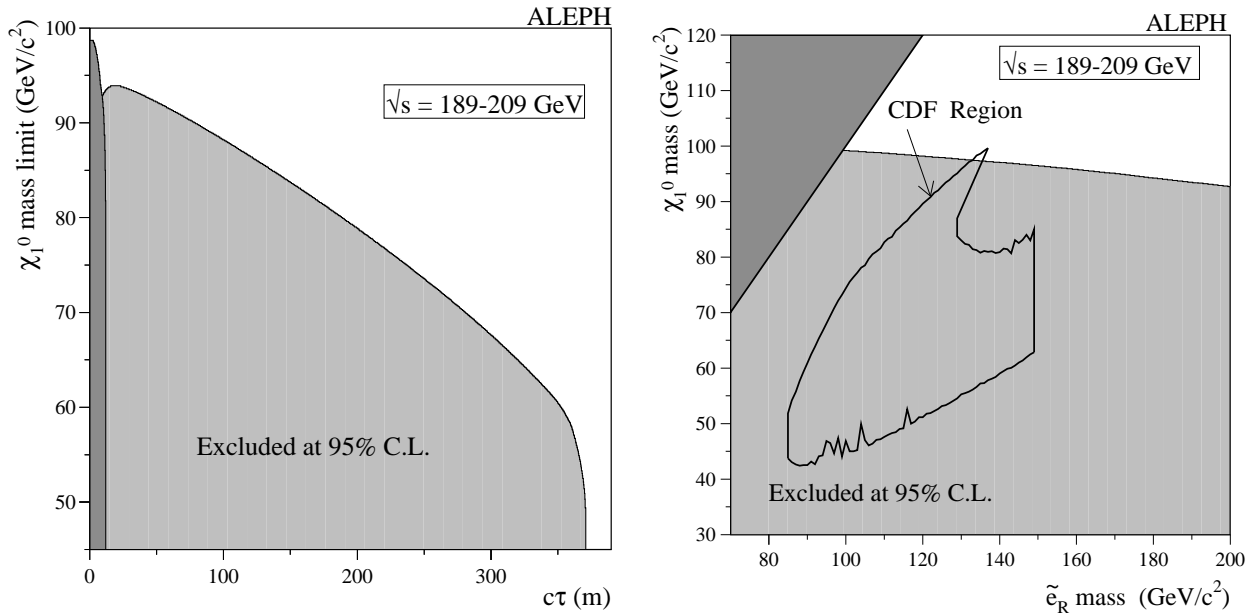


Figure 4.2: Left, the excluded neutralino mass as a function of the proper lifetime for the two-photon search (dark shade) and non-pointing photon search (light shade). On the right, in the neutralino-selectron mass plane the 95% C.L. excluded area by photon searches assuming a pure bino neutralino NLSP. Overlaid is the region favoured by the CDF event [71], interpreted as  $q\bar{q} \rightarrow \tilde{e}_R\tilde{e}_R \rightarrow e^+e^-\chi\chi \rightarrow e^+e^-\gamma\gamma\tilde{G}\tilde{G}$  [72]. The dark shaded region corresponds to  $m_{\tilde{e}_R} < m_\chi$ . From Ref. [34].

### 4.2.3 Indirect searches

For neutralinos with decay lengths greater than the detector size, indirect searches have to be used to obtain a limit on the neutralino mass. This scenario is identical to gravity mediated models with a stable neutralino LSP escaping the detector. Thus searches for sleptons  $e^+e^- \rightarrow \tilde{\ell}\tilde{\ell} \rightarrow \ell\chi\ell\chi$  and charginos  $e^+e^- \rightarrow \chi_1^+\chi_1^- \rightarrow W^{*+}\chi W^{*-}\chi$ , as developed for the SUGRA case, are utilised here<sup>3</sup>. The relationship between the  $\chi$  mass and the slepton and chargino masses in these processes can be exploited to set limits on the neutralino mass. Searches for two acoplanar leptons and missing energy are described in Ref. [73]. The exclusion limits in the slepton-neutralino mass plane can be seen in Fig. 4.3.

Charginos in the MSSM can either decay to a W boson and a neutralino (generally referred as three-body chargino decay), to a sneutrino and the corresponding lepton (two-body decay), or to a slepton and the corresponding neutrino (slepton decay mode). Chargino searches in the three-body decay mode are split into three, according to the decays of the virtual W: hadronic  $\chi_1^+ \rightarrow q\bar{q}\chi$  (four jets and missing energy), leptonic  $\chi_1^+ \rightarrow \ell^+\nu\chi$  (two acoplanar leptons and large missing energy) and mixed (two jets and one lepton). The final results are given in Ref. [74] and the selections are described in Ref [75].

## 4.3 Searches for slepton NLSP

### 4.3.1 Acoplanar leptons

If the slepton lifetime is negligible, of the order of a few mm or less, the GMSB signature arising from slepton pair-production  $\tilde{\ell} \rightarrow \ell\tilde{G}$  does not differ from that of models with gravity mediated SUSY breaking and neutralino LSP with a very small mass  $\tilde{\ell} \rightarrow \ell\chi$ . Two energetic acoplanar leptons and missing energy are expected. The search used to cover this topology is developed in the SUGRA framework but its results can be interpreted in GMSB taking  $m_\chi \simeq 0$  (the gravitino is at least six orders of magnitude lighter than the neutralino). Details of the selection criteria are described in Ref. [73]. The largest background is due to W pair-production followed by leptonic W decay:  $W \rightarrow \ell\nu$  which is kinematically very similar to  $\tilde{\ell} \rightarrow \ell\tilde{G}$  for slepton masses around the W mass. Cuts on  $M_{\text{vis}}$  and the momentum of the most energetic lepton are needed to reduce this type of background<sup>4</sup>.

For each lepton flavour, the number of data events selected in year 2000 data is 39, 39 and 11 for electrons, muons and taus, to be compared with respectively 38.7, 34.7 and 12.2 expected events from background. The contribution from the WW background is around 80%. Thus good agreement between the SM prediction and the experimental results is obtained in this topology. The expected and observed mass limits (with WW background subtraction) for each slepton flavour are shown in Fig. 4.3.

### 4.3.2 Large impact parameters and kinks

Two distinctive topologies with very small background level may arise for intermediate slepton lifetimes. If the slepton decays before having produced a reconstructible track, i.e. for  $\lambda$

<sup>3</sup> If the sleptons are lighter than the charginos, two-body decays of charginos will dominate:  $\chi_1^+ \rightarrow \tilde{\ell}^+\nu$  or even  $\chi_1^+ \rightarrow \ell^+\tilde{\nu}$ .

<sup>4</sup> The lepton's energy distribution is flat with the same endpoints  $E_{\text{min}}, E_{\text{max}}$  as Eq. 4.1 with  $m_{\tilde{\ell}}$ . Thus leptons are expected to be energetic and, specially smuons and staus with only  $s$ -channel production, to have symmetric distributions in the polar angle  $\theta$ .

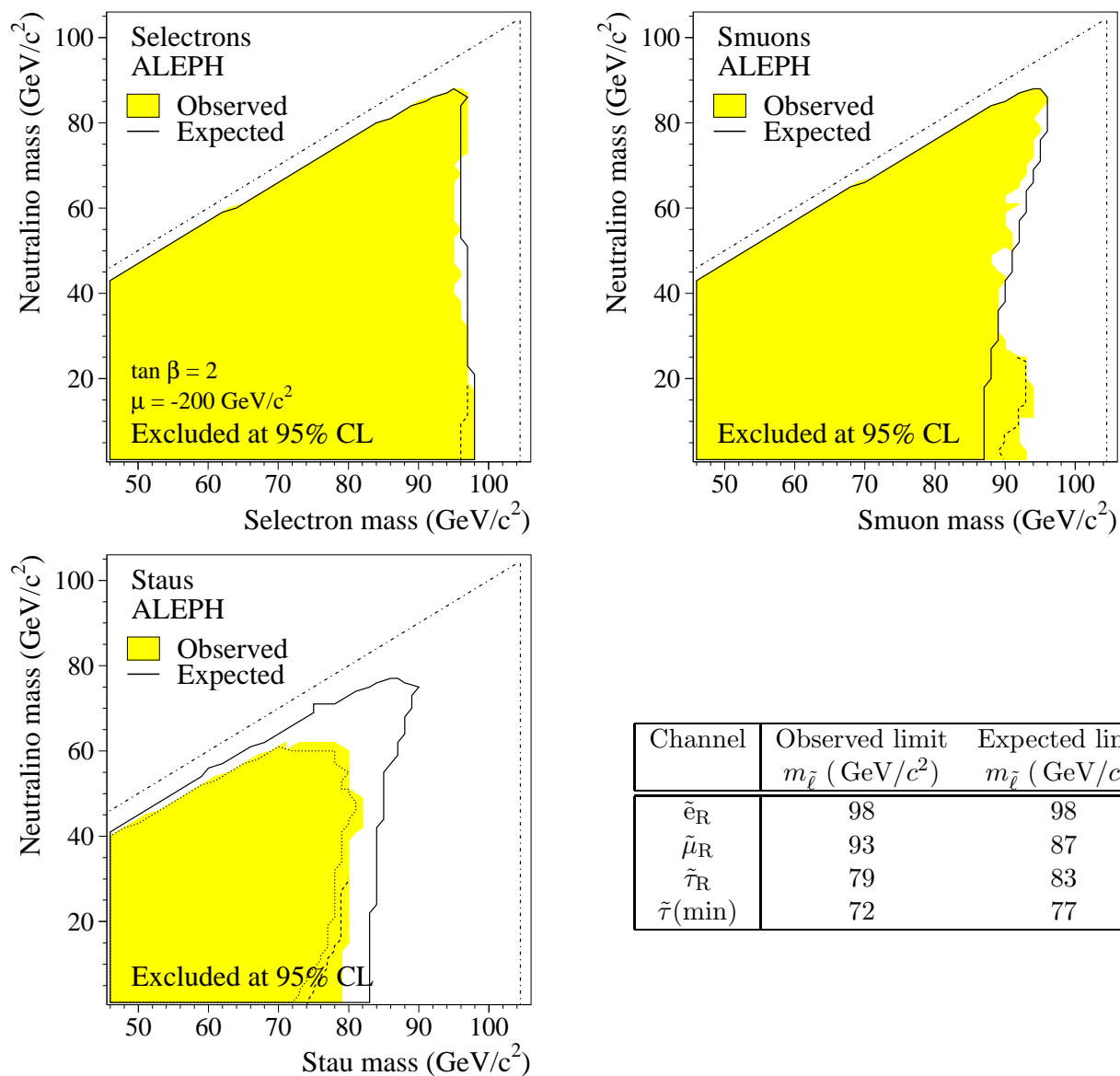


Figure 4.3: Excluded regions at 95% C.L. in the  $m_{\tilde{\ell}_R}$  versus  $m_\chi$  plane in the acoplanar leptons SUGRA search [73]. The observed (shaded area) and expected (solid curve) limits are given for  $\text{BR}(\tilde{\ell}_R \rightarrow \ell\chi) = 1$ . The dashed curves give the observed limits when slepton cascade decays (into  $\ell\chi_2$ ) are taken into account, generally for very small neutralino masses. The dashed-dotted curves mark the kinematically accessible region in the MSSM at 209 GeV for a neutralino LSP. The table lists the lower limits on the slepton masses for  $m_\chi \simeq 0$ . For the stau, the minimum limit (shown as the dotted curve in the stau plot) is calculated with a mixing angle of  $\theta_{\tilde{\tau}} \simeq 52^\circ$  which minimises the production cross section.

	Large impact parameter	Kinks
Anti- $\gamma\gamma$	1 or more tracks with 6 TPC hits and $p_t > 0.03\sqrt{s}$ $E_{\text{vis}} > 0.03\sqrt{s}$	
Anti- $\ell\ell$ , cosmics, Bhabha	Remove conversions ECAL timing with single helix fit $E_{\text{vis}} < 0.65\sqrt{s}$	
Tracks quality cuts	2 or 4 tracks with $\geq 4$ TPC hits  <u>Track #1</u> : $d_0 > 1$ cm and $p_1 > 0.01\sqrt{s}$ <u>Track #2</u> : $d'_0 > 0.025$ cm	$\leq 6$ tracks with TPC hits. Same-charge tracks with $d_{r\phi} < 5$ cm and $d_z < 20$ cm. <u>Inner track</u> : $d_0^{(1)} < 0.5$ cm. <u>Outer track</u> : $d_0^{(2)} > 1$ cm with at least 4 TPC hits, $p > 0.015\sqrt{s}$ and $\alpha_{2,z} > 18.2^\circ$
Anti- $\gamma\gamma$ , $\ell\ell$ and had. ints.	Acoplanarity $< 175^\circ$  Acollinearity $< 11.5^\circ$	$\alpha_{1,2} > 5^\circ$ or $\alpha_{1,2} > 10^\circ$ if outer track has no TPC hits. $E_5^1 < 5$ GeV

Table 4.3: List of cuts for the large impact parameter and kinks selections.

between a few mm and a few cm, the lepton tracks will present large distances to the beam axis (impact parameters). Otherwise, if the slepton reaches the tracking devices and is reconstructed as a charged track decaying with  $\lambda \gtrsim 40$  cm, the typical signature consists then of kinks formed between the slepton track and its lepton decay product.

The preselection procedure is the same for both large impact parameter and kinks searches. Anti- $\gamma\gamma$ , dilepton and cosmic rays cuts are applied as listed in Tab. 4.3.

### Search for large impact parameters

Events containing exactly two or four charged tracks are selected to attempt tau identification. At least one track (track 1) is required to have an impact parameter greater than 1 cm and total momentum of at least  $1\%\sqrt{s}$ . Only one or three additional tracks with at least four TPC hits are allowed. If there are three tracks, they must be consistent with a three-prong tau decay. These tau triplets are treated as one track (track 2) calculating the mean value of the three impact parameters as the tau  $d_0$  and the sum of the momenta as the tau direction. Track 2 is required to have an impact parameter of at least 0.025 cm. The acoplanarity and acollinearity<sup>5</sup> of tracks 1 and 2 are used to suppress dilepton and  $\gamma\gamma$  background.

### Search for kinks

Kinks are reconstructed by searching for same-sign tracks crossing in the  $r\phi$  plane (transverse to the beam axis) or approaching each other in this projection closer than 5 cm inside the tracking volume. At this point, the separation between the two in the  $z$  direction should be less than 20 cm.

In the search for kinks the most important sources of background are hard bremsstrahlung and hadronic interactions in the material of the detector from  $K_s^0$ ,  $K^\pm$  or  $\pi^\pm$  decays. To reduce

<sup>5</sup>The acollinearity is defined as the opening angle between two tracks.



the former, the angle between the primary and secondary track  $\alpha_{1,2}$  must be greater than  $5^\circ$  at the kink vertex: kinks from bremsstrahlung are peaked at low values of  $\alpha_{1,2}$ . Finally, the residual background comes from ditau events with hadronic interactions in the material, i.e. when the kink is found between 26 and 34 cm radius. These events are characterised by accompanying collinear particles to the interacting hadron, thus the energy deposited in the calorimeters within  $5^\circ$  around the axis from the IP to the kink must be less than 5 GeV to reject these events.

## Combination

Combined efficiencies above 20% and with a maximum of  $\sim 65\%$  for stau samples are obtained in the NLSP lifetime range covered by the large impact parameter and kinks searches from  $\sim 10^{-10}$  to  $10^{-7}$  s. The efficiency is higher for selectron and smuon samples due to the absence of three-prong decays and the higher momenta of the leptons. In the 189 – 209 GeV data sample only one event is selected by the combined search with 1.1 expected from SM backgrounds. The event is recorded at 189 GeV and is compatible with a three-prong tau decay in the large impact parameter selection [76].

### 4.3.3 Heavy stable charged particles

Long-lived sleptons can be detected as two back-to-back charged particles with unusually high values of  $dE/dx$  for their momentum. They are not expected to interact hadronically (they do not have colour charge) nor electromagnetically (since they are very heavy). Thus they should be very similar to dimuon events only distinctive by their high specific ionisation. In the kinematical limit, where the sleptons are expected to be very slow, the energy loss becomes high enough to saturate the TPC electronics. To cover this interesting mass region an additional selection based on calorimeter information and the pattern of saturated hits was developed [77].

Stable sleptons	
$N_{\text{ch}} = 2$ each with $p_t > 0.1E_{\text{beam}}$ $ \cos\theta  < 0.9$ with more than 1 ITC hit $ d_{01}  +  d_{02}  < 0.3$ cm $ z_{01}  +  z_{02}  < 5$ cm No identified electron Acollinearity $> 160^\circ$ $ p_1 - p_2  < 3\sqrt{\sigma_{p_1}^2 + \sigma_{p_2}^2}$ $E_\gamma < 250$ MeV $E_{\text{ECAL1}} + E_{\text{ECAL2}} < 20$ GeV and $E_{\text{HCAL1}} + E_{\text{HCAL2}} < 50$ GeV	
$0.52 < m_{1,2}/E_{\text{beam}} < 0.80$	$0.80 < m_{1,2}/E_{\text{beam}} < 0.98$
Acollinearity $> 174^\circ$	$R_{I1} + R_{I2} > 10$

Table 4.4: List of cuts for the heavy stable charged particle selection for intermediate-high masses. The region close to the kinematic limit ( $m_{1,2} \geq 0.95E_{\text{beam}}$ ) is explored by the search for saturated TPC hits described in Ref. [77].

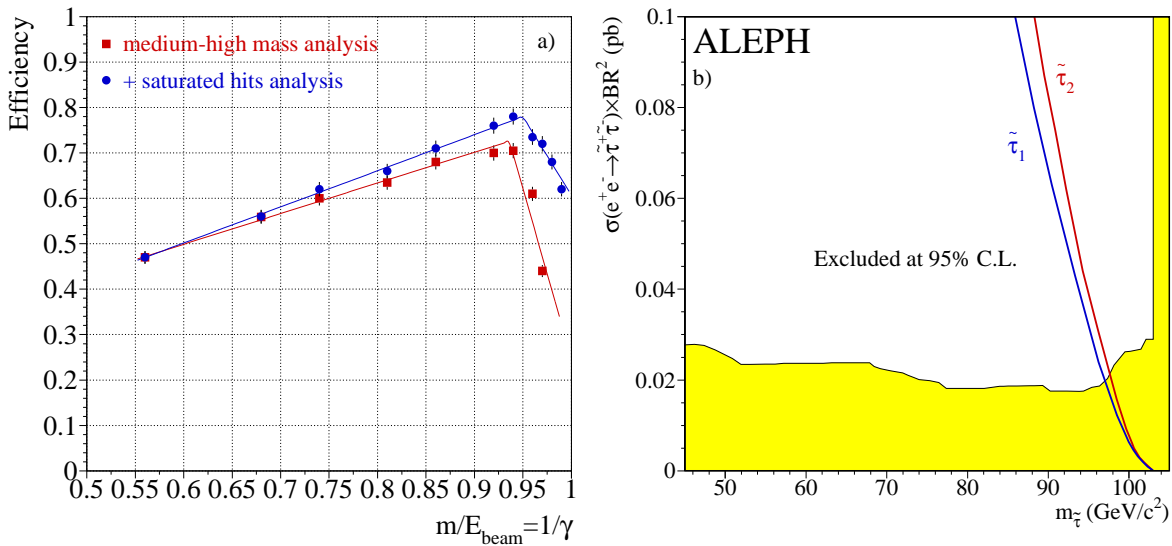


Figure 4.4: (a) Efficiency of the search for pair-production of massive, spin-0 stable particles as a function of  $m/E_{\text{beam}}$  with (circles) and without (squares) analysis of events with no good tracks due to saturation. (b) The maximum allowed cross section calculated at 95% confidence level with data taken in year 2000 at centre-of-mass energies of 202–209 GeV (filled area) with the heavy stable charged particles search (including the analysis of saturated hits). The solid lines represent the minimum expected cross section times branching ratio for the lightest and heaviest  $\tilde{\tau}$  pair-production at  $\sqrt{s} = 207$  GeV. Thus stau masses of up to 97 GeV/ $c^2$  are excluded by this search alone in the stau NLSP scenario.

Table 4.4 describes the cuts used in the selection of medium-high masses. The track quality criteria, the first four cuts in Tab. 4.4, are imposed to reject events with poorly reconstructed tracks and cosmic rays. The electron ID veto and the angle acceptance reduce the large Bhabha background. The acollinearity cut effectively reduces the radiative  $Z$  returns,  $\gamma\gamma$  and  $\tau^+\tau^-$  events. The momentum cuts also reject  $\gamma\gamma$  and  $\tau\tau$  events. Requiring no photons with energy greater than 250 MeV considerably reduces on-shell  $Z$  events and Bhabhas. Finally the ECAL and HCAL energy deposits help in Bhabha rejection. After these cuts are applied, the high mass of the signal has not been used and the background is dominated by  $\mu^+\mu^-$  events. If the reconstructed mass of the particles  $m_i = \sqrt{E_{\text{beam}}^2 - p_i^2}$  is low the momenta of the tracks are high enough to produce an energy loss similar to that of ordinary particles. Only in the high mass range will the  $dE/dx$  information be useful in terms of the estimator  $R_I = (I - \langle I_\mu \rangle) / \sigma_I$ . Here one compares the measured  $dE/dx$ ,  $I$ , to that expected for a muon  $\langle I_\mu \rangle$ , where  $\sigma_I$  is the expected resolution of the measurement.

The case of masses  $m_i$  above  $0.95E_{\text{beam}}$  is described in Ref. [77] where the selection makes use of the position of the two most energetic calorimeter objects and the IP to perform a single-helix fit of the transverse momentum and polar angle of the two track candidates. Thus the trajectories of the particles can be estimated without ITC or TPC information and are then compared with the saturated and unsaturated hits. The efficiency ranges roughly from 50 to 70% for the intermediate-high mass, between 0.5 and 0.93  $m/E_{\text{beam}}$ . If the analysis of saturated hits is included as described in Ref. [77], the efficiency is improved and maintained with an approximately flat distribution (within  $\pm 10\%$ ) reaching the highest values of  $m/E_{\text{beam}}$ . The efficiencies for both medium-high and ultra-high  $p$  masses selections are shown in Fig. 4.4a.

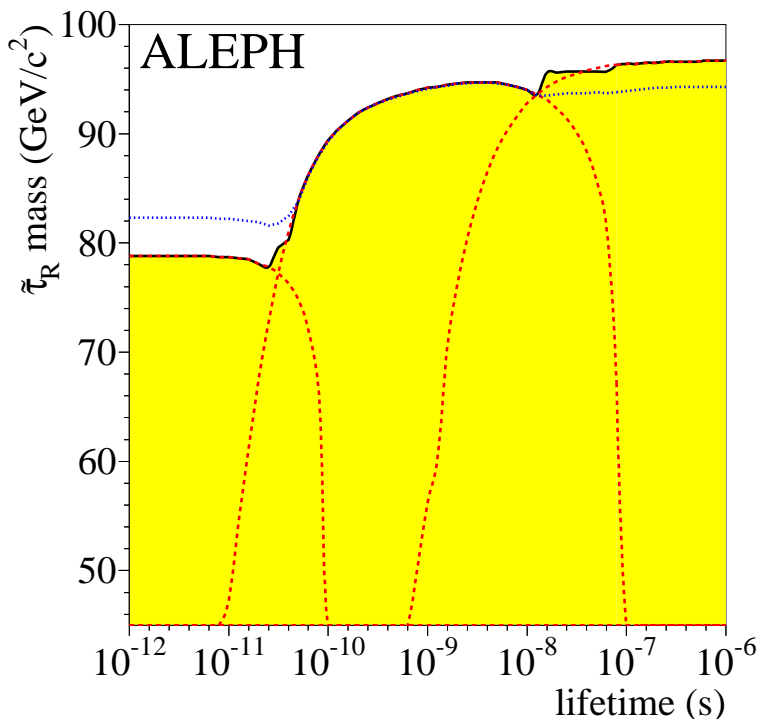


Figure 4.5: Excluded stau mass at 95% confidence level as a function of its lifetime (shaded area) from direct searches. Dashed curves give the limits from the different topologies. The search for acoplanar leptons covers the case of small lifetimes, searches for tracks with large impact parameter and for kinks are used in the intermediate range, whereas for large lifetimes a search for heavy stable charged particles is performed. The dotted curve gives the expected limit. From Ref. [65].

The combination of intermediate-high mass searches and the saturated hits analysis selects one data event while 2.3 are expected from background, mainly dimuons. Systematic effects have been studied with independently selected dimuon samples from the data to check the performance of the tracking system. Specific ionisation effects have been checked with electrons, muons and pions over a large range in momentum. A total systematic error of less than 5% is estimated and conservatively applied to the selection efficiency. Figure 4.4b shows that cross sections as low as 0.02 pb are excluded using only the year 2000 data set for stau pair-production.

### Combination of direct slepton NLSP production searches

When all the above selections are combined including all lifetimes, the 95% confidence level lower limits on the right-slepton masses, independent of lifetime, are set at 83, 88 and 77 GeV/ $c^2$  for selectron, smuon and stau, respectively. The selectron mass limit is obtained neglecting the  $t$ -channel exchange contribution to the production cross section. Figure 4.5 gives the excluded stau mass as a function of its lifetime when all the above described searches are combined. The dotted lines represent the independent limits from searches for negligible lifetime (acoplanar leptons from SUGRA with  $m_\chi \sim 0$ ), intermediate lifetime (large impact parameters and kinks) and long lifetime (heavy stable charged particles). The .OR. of the searches is the solid line [65].

### 4.3.4 Cascade decays of neutralinos

Searches for slepton NLSP pairs when they are produced directly at LEP and decay to a lepton and a gravitino have been described above. However, if the  $\chi\chi$  production is allowed, it generally provides the dominant signal in the slepton NLSP scenario. This is because the production cross section for neutralinos is larger than for sleptons since it is not  $\beta^3$  suppressed, even for  $m_\chi > m_{\tilde{\ell}}$  (see Fig. 3.2b). The expected signal is therefore four leptons and missing energy from the cascade decay:  $e^+e^- \rightarrow \chi\chi \rightarrow \tilde{\ell}\tilde{\ell}'\tilde{\ell}'' \rightarrow \ell\tilde{G}\ell'\tilde{G}$ . Two of the leptons may be very soft depending on the mass difference between the neutralino and the slepton. However, in half of the cases the two hard leptons may have the same charge because of the Majorana nature of the neutralino. This makes this type of decay a very clean discovery signal in models with small  $N_5$  and  $\tan\beta$  not too large. In ALEPH, searches for  $\ell\ell'(\ell\ell')\cancel{E}$  have been carried out for both negligible slepton lifetimes and intermediate slepton lifetimes, when two of the tracks present kinks or large impact parameters [65]. Since the neutralinos decay independently of one another, there are six possible topologies for the slepton co-NLSP, namely:  $\tilde{e}\tilde{e}$ ,  $\tilde{\mu}\tilde{\mu}$ ,  $\tilde{\tau}\tilde{\tau}$ ,  $\tilde{e}\tilde{\mu}$ ,  $\tilde{e}\tilde{\tau}$  and  $\tilde{\mu}\tilde{\tau}$ . In the stau NLSP case, only the  $\tilde{\tau}\tilde{\tau}$  topology is relevant.

Selection		$\tilde{e}\tilde{e}$	$\tilde{\mu}\tilde{\mu}$	$\tilde{\tau}\tilde{\tau}$	$\tilde{e}\tilde{\mu}$	$\tilde{e}\tilde{\tau}$	$\tilde{\mu}\tilde{\tau}$
Negligible Lifetime	obs.	6	1	22	2	8	5
	exp.	5.15	0.44	16.49	3.65	5.52	5.72
Intermediate Lifetime	Short $\lambda$	obs.	5				
		exp.	5.25				
	Long $\lambda$	obs.	4				
		exp.	1.51				

Table 4.5: Number of observed and expected events in the searches for four leptons and missing energy in the 189 – 209 GeV data. In the intermediate lifetime case there is large overlap between the different selections and the results are given for the total.

### Four leptons and $\cancel{E}$

In the ‘no lifetime’ case for topologies not involving taus, the presence of at least three identified electrons or muons is required but not more than four charged tracks. This helps to reject  $q\bar{q}$  and four-fermion events with high multiplicity. For each topology, at least two energetic leptons are required which must be acoplanar, acollinear and their energies must be in the range allowed by the signal kinematical properties. These cuts reject effectively the dilepton background. The kinematic cuts reduce also leptonic WW decays and  $W\ell\nu$  background.

For topologies involving taus  $\tilde{e}\tilde{\tau}$  and  $\tilde{\mu}\tilde{\tau}$ , the number of charged tracks per event and the mean number of neutrinos carrying away missing energy and momentum are considerably bigger than in  $\tilde{e}\tilde{e}$ ,  $\tilde{\mu}\tilde{\mu}$  and  $\tilde{e}\tilde{\mu}$  topologies. Thus four, five or six charged tracks are allowed with at least one identified lepton. Finally, for  $\tilde{\tau}\tilde{\tau}$  topologies at least three identified tau jets are required with not more than two other charged tracks. Cuts on the Durham cluster thresholds, the energy of the event and the momentum of the most energetic lepton are used to reduce the main background contributions, WW and  $\tau\tau$  events. The selection cuts are described in detail in Ref. [65].

Efficiencies of up to 80% are achieved in the  $\tilde{e}\tilde{e}$  and  $\tilde{\mu}\tilde{\mu}$  selections. For topologies with taus, the efficiency can be as low as 30% for small differences between the neutralino and the

stau, reaching a maximum of 60% for energetic taus. Figure 4.6a displays the efficiencies as a function of  $\Delta m_{\chi\tilde{\ell}}$ . The number of selected events in the 189 – 209 GeV data is shown in Tab. 4.5 for each topology.

### Four leptons and $\cancel{E}$ with lifetime

A detailed description of this search can be found in Ref. [78]. The topology consists of two tracks with large impact parameter or kinks and two tracks originating from the interaction point. Thus the basic selection requirements rely on tracks with more than four hits in the TPC and high- $d_0$ . The main background sources are nuclear interactions, photon conversions, ECAL ‘splashbacks’ and cosmic muons. Table 4.5 shows the comparison between expected background and selected data events in the large impact parameter and kinks searches. All but one of the selected events can be assigned to a known source of background.

The efficiency of the long decay selection (kinks) as a function of lifetime is presented in Fig. 4.6b for the  $\tilde{\tau}\tilde{\tau}$  signal. A peak of 80% efficiency is achieved at decay lengths around 10 cm deteriorating for small  $\Delta m_{\chi\tilde{\tau}} = m_\chi - m_{\tilde{\tau}}$ . Also shown in that figure is the efficiency for the negligible lifetime selection when applied to signal data with slepton lifetime. Overall, an efficiency in excess of 10% is maintained for slepton decay lengths from  $\sim 1$  mm to  $\sim 10$  m for all channels [78].

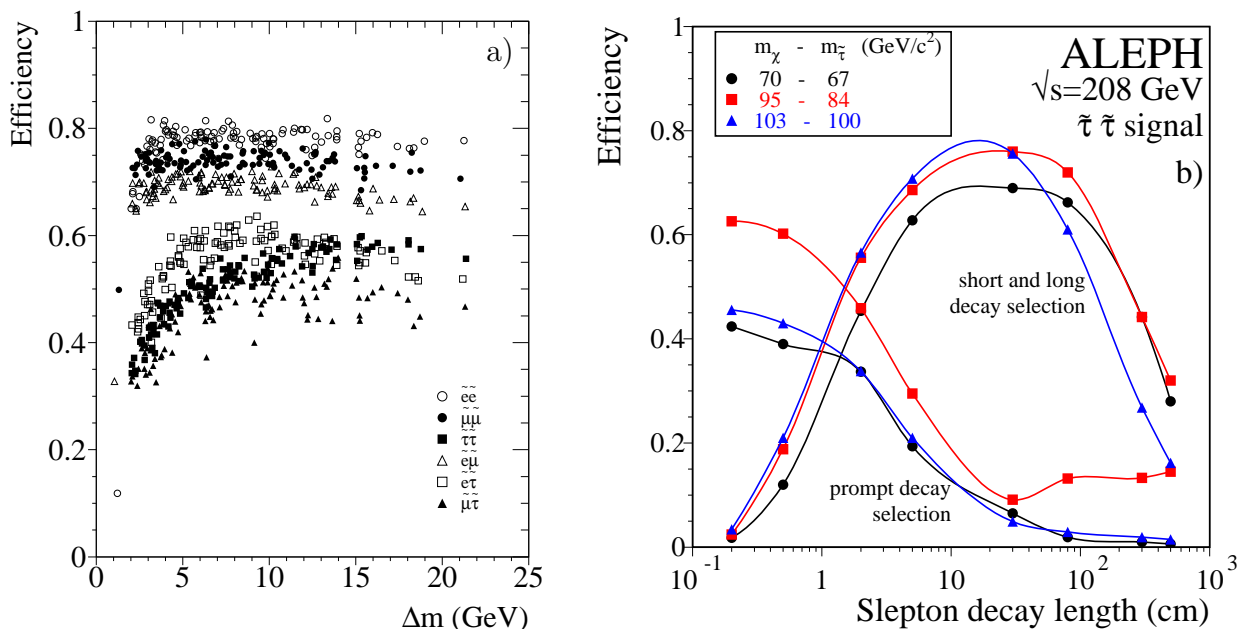


Figure 4.6: (a) Selection efficiencies for the six different event topologies versus  $\Delta m_{\chi\tilde{\ell}} = m_\chi - m_{\tilde{\ell}}$  in the negligible slepton lifetime case. The spread of points observed for a given topology is due to different values of neutralino and slepton masses. (b) Probability for a signal stau-pair event to be selected by at least one of the six topological searches versus slepton decay length. The set of curves with higher efficiency in the 0.1 cm area corresponds to the prompt decay selection. Those peaking at  $\sim 10$  cm correspond to the short and long decay length selection. Different lines correspond to different points in the  $(m_\chi, m_{\tilde{\tau}})$  space as indicated.

## 4.4 Neutral Higgs boson searches in the MSSM

Searches for neutral MSSM Higgs bosons can also be used to constrain the GMSB parameter space. Although these searches are performed in the framework of gravity mediated scenarios, the Higgs sector is intrinsically the same in GMSB models. Thus limits from one can be applied to the other taking into account the different parameters involved in the determination of the Higgs masses and couplings.

At LEP2 the lightest CP-even  $h^0$  and CP-odd  $A^0$  neutral Higgs bosons can be produced through *Higgsstrahlung*  $e^+e^- \rightarrow Z^* \rightarrow hZ$  and *associated production*  $e^+e^- \rightarrow Z^* \rightarrow hA$  (see Fig. 1.6d). The cross sections of these two reactions are complementary, Higgsstrahlung is dominant at low  $\tan\beta$ ; while  $hA$  has larger cross sections at large  $\tan\beta$ . This is due to the MSSM suppression factors  $\sin^2(\beta - \alpha)$  and  $\cos^2(\beta - \alpha)$  [5]:

$$\sigma(e^+e^- \rightarrow hZ) \sim \sin^2(\beta - \alpha)\sigma_{\text{SM}} \quad (4.2)$$

$$\sigma(e^+e^- \rightarrow hA) \sim \cos^2(\beta - \alpha)\sigma_{\text{SM}} \quad (4.3)$$

where  $\sigma_{\text{SM}}$  is the production cross section for the SM Higgs boson radiated off from a  $Z$ , and  $\alpha$  is the mixing angle of the two Higgs fields that produce  $h$  and  $H$ .

From now on  $h$  denotes the MSSM as well as the SM Higgs boson. The two most relevant decays of  $h$  and  $A$  are to  $b\bar{b}$  and  $\tau^+\tau^-$ . Thus four main signal topologies arise: four jets, missing energy, leptonic and tau final states, as listed in Tab. 4.6.

Topology	Z decay	$h$ decay	$A$ decay	BR( $hZ \rightarrow$ )	BR( $hA \rightarrow$ )
Four jets	$q\bar{q}$	$b\bar{b}$	$b\bar{b}$	70%	86%
Missing energy	$\nu\bar{\nu}$	$b\bar{b}$	$\chi\chi, \tilde{G}\tilde{G}, \dots$	20%	small
Leptonic	$l^+l^-$	$b\bar{b}$	—	7%	—
With taus	$q\bar{q}$	$\tau\tau$	$b\bar{b}$	3%	13%
	$\tau\tau$	$b\bar{b}$	$\tau\tau$		

Table 4.6: The four main topologies considered in neutral Higgs boson searches, as derived from  $hZ$  or  $hA$  decays. The branching ratios for  $hZ$  decays are given for the Standard Model Higgs with mass  $115 \text{ GeV}/c^2$ . In  $hA$  decays, the listed branching fractions are valid for maximal  $h$  masses and  $\tan\beta < 30$ .

Searches for all the above topologies have been performed in ALEPH and the selections are described in Ref. [79] with the final results given in Ref. [80], here only a general description is given.

The four-jet final state is the most likely signal given its large branching fraction, but suffers from irreducible backgrounds such as  $ZZ, b\bar{b}$  with FSR hard gluon splitting to a pair of  $b$ -quarks and  $WW$  with  $b$ -quark misidentification. Nevertheless, the four jets in the signal are expected to be contained in a plane if the  $Z$  and  $h$  or  $h$  and  $A$  are produced almost at rest. In the first case, the invariant mass of two of the jets should be close to  $m_Z$  and the other two contain  $b$  flavour, while for the second case all four jets contain  $B$  hadrons.

The missing energy final state is characterised in  $hZ$  production by  $M_{\text{miss}} \sim m_Z$  and substantial missing transverse momentum. In the case of  $hA$  production, if other SUSY particles are kinematically accessible or the bosons undergo a  $WW$  fusion process into  $b\bar{b}\nu_e\bar{\nu}_e$ , a similar event topology is obtained.

If the  $Z$  decays to electrons or muons, the two leptons must reconstruct the  $Z$  mass and the two jets should be tagged as  $b$ -jets.  $m_h$  can then be reconstructed accurately from the system recoiling against the two leptons with a typical mass resolution of about  $1.5 \text{ GeV}/c^2$ .

The relevant limit for GMSB searches is obtained by the combination of the  $hZ$  and the  $hA$  searches in the plane given by the  $h$  mass and the factor  $\sin^2(\beta - \alpha)$ . This plane is model independent and the present ALEPH exclusion is shown in Fig. 4.7.

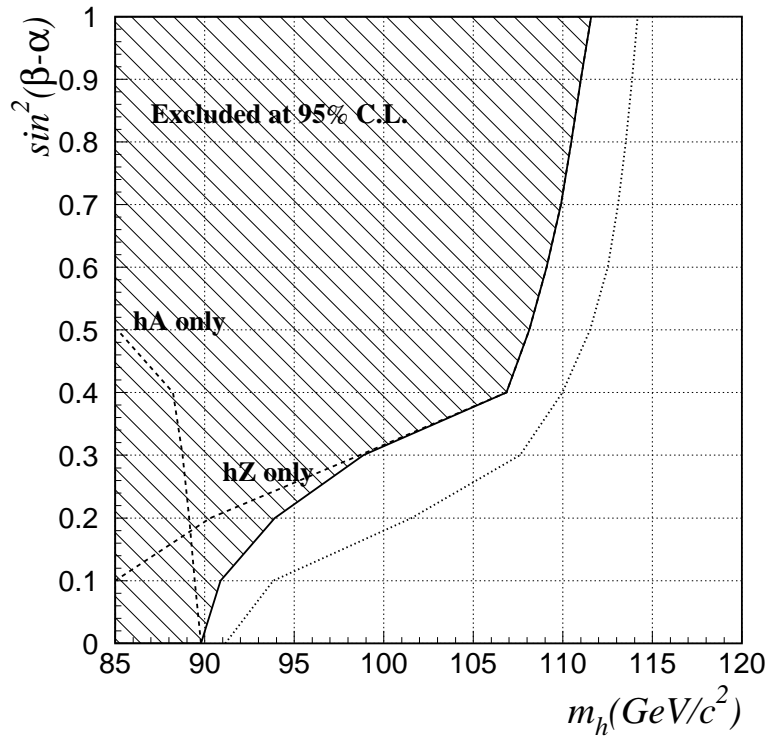


Figure 4.7: The 95% confidence level exclusion contours for the  $hZ$  and  $hA$  searches as a function of  $\sin^2(\beta - \alpha)$  (dashed lines). The combined exclusion is shown by the hatched area and the dotted line indicates the expected exclusion. From Ref. [80].

# Chapter 5

## Interpretation of results

The previous two chapters describe all the searches performed in the ALEPH collaboration in the search for GMSB topologies. No hint for a signal is observed in any of them. This chapter is therefore devoted to understand what the lack of evidence for such signals may tell about the theoretical models that predict them. Understanding the effect of ‘not seeing’ any signal at LEP is important to design new searches at future colliders and maybe address new theoretical models.

The interpretation of the search results in this work has been limited so far to a specific model or constrained by simplifying assumptions made to derive the limits. To extrapolate these results to the more general case, a scan is performed over the six parameters that fully determine GMSB phenomenology. It is then possible to test the robustness of the previous results, checking how they may change when no assumptions whatsoever are made, and to interpret them in a wider context. Moreover, each of the above searches will contribute to exclude different regions in the minimal GMSB parameter space, thus constraining the different parameters of the model distinctively. It will be important to determine which searches set the most effective limits on the theoretical parameters.

The final ALEPH combined limits on the parameters set in this chapter are in most cases very close to the sensitivity of the detector to such signals. A discussion on the allowed ranges of the parameters is presented, to assess the validity of these limits if the scan ranges were enlarged.



## 5.1 The scan

The entire sparticle mass spectrum and all possible phenomenological topologies can be determined by only six parameters in GMSB models [32]. A scan over these parameters has been performed to interpret the results of the experimental searches. The aim is to understand which searches contribute to exclude which regions in the parameter space and to be able to set a lower limit on the mass of the NLSP and on the universal mass scale  $\Lambda$ , independent of the NLSP lifetime (i.e., for all gravitino masses). The program ISASUSY 7.51 [57] was used to calculate masses, cross sections, and branching ratios for all SUSY particles at each point in the parameter space. Radiative corrections to chargino and neutralino masses were applied. The Higgs bosons' masses and couplings were calculated using the improved Haber et al. treatment at two loops implemented in HZHA 3.0 [81] with a top mass of  $175 \text{ GeV}/c^2$ .

### 5.1.1 Scan ranges

The ranges of the scan are given in Tab. 5.1 for each parameter as well as the step size. In total, over 2.3 million points in the minimal GMSB parameter space have been tested. If the NLSP mass is greater than the highest beam energy (104.5 GeV) the point is not considered (and cannot be excluded). The scan is not exhaustive but it covers a large portion of the allowed range of the minimal GMSB parameter space, as discussed next.

Parameter	Lower limit	Upper limit	Steps
$M_m$	$10^4 \text{ GeV}/c^2$	$10^{12} \text{ GeV}/c^2$	7
$m_{\tilde{G}}$	$10^{-1} \text{ eV}/c^2$	$10^5 \text{ eV}/c^2$	15
$\Lambda$	$10^3 \text{ GeV}/c^2$	$\min(\sqrt{F_m}, M_m)$	100
$N_5$	1	5	5
$\tan \beta$	1.5	40	22
$\text{sign}(\mu)$	–	+	2

Table 5.1: Minimal set of parameters and their ranges of variation used in the scan.

### Validity of the ranges

$M_m$  An approximate upper bound on the common messenger mass is imposed by flavour universality. This can only be maintained if gravity mediated contributions to the observable masses (of the order  $F_0/M_P$ ) are kept small  $\sim \mathcal{O}(10^{-3})$ . Thus to avoid large flavour violating transitions [29]:

$$M_m \lesssim \frac{1}{10^{\frac{3}{2}} 4\pi} \alpha M_P \sim 10^{15} \text{ GeV}/c^2 \quad (5.1)$$

Furthermore, NLSP decays in the early Universe must not spoil the predictions from Big Bang nucleosynthesis. These bounds can further reduce the upper limit on  $M_m$  as described in Ref. [82]. The lower limit is determined by  $\Lambda$  with the condition  $M_m > \Lambda$ .

$m_{\tilde{G}}$  The gravitino mass range is deduced from Cosmology and from indirect searches. Direct collider searches  $e^+e^- \rightarrow \tilde{G}\chi$  set a lower limit on  $m_{\tilde{G}}$  of  $\sim 10^{-5} \text{ eV}/c^2$  (see Sec. 1.5), but

previous indirect limits suggest that  $m_{\tilde{G}} > 10^{-2} \text{ eV}/c^2$  [76]. In any case, the gravitino mass controls the lifetime of the NLSP. Phenomenologically, setting  $m_{\tilde{G}}$  below  $10^{-1} \text{ eV}/c^2$  would not improve the scan, since that is enough to cover all cases with negligible NLSP lifetime  $\sim 10^{-12} \text{ s}$ . As regards the upper limit of  $100 \text{ keV}/c^2$ , it is imposed by standard Big Bang constraints [83]. A heavier gravitino would overclose the Universe at an early stage, because  $\rho_{3/2}(T) \equiv m_{\tilde{G}} n_{\tilde{G}}(T) > \rho_c(T)$  where  $n_{\tilde{G}}$  is the number density of gravitinos, which depends on scattering processes off thermal radiation and the decay of heavier particles into gravitinos, and  $\rho_c$  is the critical density. Even assuming dilution mechanisms such as inflation, an overproduction of heavier gravitinos in the reheating epoch can lead to cosmologically unacceptable values of the relic density [84].

**$\Lambda$**  The universal mass scale parameter is constrained from above by the mass of scalar messengers.

$$(m_0^{\text{mess}})^2 = M_m^2 \pm F_m > 0 \iff F_m < M_m^2 \quad (5.2)$$

$$\Lambda \equiv \frac{F_m}{M_m} \implies \begin{cases} \Lambda < M_m \\ \Lambda < \sqrt{F_m} \end{cases} \quad (5.3)$$

This upper limit  $\Lambda < \min(M_m, \sqrt{F_m})$  means that values up to  $100 \text{ TeV}/c^2$  were scanned. Higher values would drive the NLSP mass beyond  $1 \text{ TeV}/c^2$ .

**$N_5$**  The number of messenger families is allowed to vary up to five. The messenger sector affects how the gauge couplings unify at the GUT scale. In order to maintain corrections to the GUT gauge coupling small, and thus allow for unification,  $N_5$  and  $M_m$  should obey [29]:

$$N_5 \leq \frac{150}{\ln\left(\frac{M_{\text{GUT}}}{M_m}\right)} \quad (5.4)$$

As can be seen in Fig. 1.7b, for  $M_m$  as low as  $100 \text{ TeV}/c^2$   $N_5$  can be at most five. Yet, for  $M_m = 10^{10} \text{ GeV}/c^2$   $N_5$  as large as ten is allowed. However, values of  $N_5 = 6$  do not change significantly the results as will be proved later.

**$\tan\beta$**  The ratio of the two Higgs doublets vacuum expectation values has been changed from 1.5 up to 40 in the scan. Lower values of  $\tan\beta$  are strongly disfavoured by Higgs boson searches, while calculations of SUSY parameters in the ultra-high regime, beyond  $\sim 40$ , become unreliable.

**$\text{sign}(\mu)$**  The value of the mass mixing parameter between the two Higgs doublets can be computed by enforcing correct electroweak symmetry breaking (Eq. 1.14), thus only an ambiguity in its sign remains.

### 5.1.2 Exclusion procedure

Once the possible GMSB models are available, the exclusion procedure takes place:

- First, the contribution from unknown processes to the Z width cannot exceed  $4.7 \text{ MeV}$ . The extremely precise measurement of  $\Gamma_Z$  from LEP1 allows one to exclude every new particle that could contribute to the Z decay width beyond the small experimental error. The procedure to determine  $\Delta\Gamma_Z$  is sketched in Fig. 5.1. The Z width depends on the Higgs mass  $m_h$ , the strong coupling constant  $\alpha_s$ , the electroweak coupling constant  $\alpha_{\text{em}}$

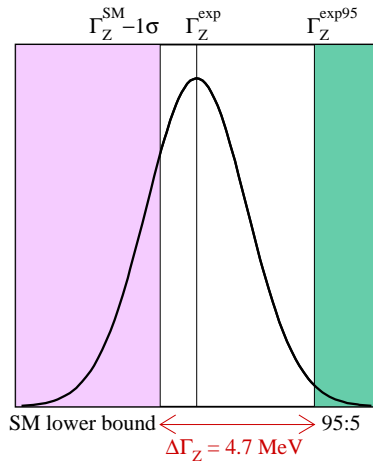


Figure 5.1: Procedure to determine the allowed SUSY contribution to  $\Gamma_Z$ .

and the top- and bottom-quark masses. Thus all these parameters, and their experimental errors, enter in the calculation of the predicted  $\Gamma_Z^{\text{SM}} \simeq 2496.1 \pm 1.2 \text{ MeV}$ , which defines a one-sigma lower bound (2494.9 MeV). This was calculated with the program ZFITTER [85] and the latest experimental values of the parameters [5]. Then a Gaussian distribution is assumed centered on the experimental value  $\Gamma_Z^{\text{exp}} \simeq 2495.2 \pm 2.3 \text{ MeV}$ . The 95% C.L. upper bound is calculated by dividing the remaining area under the gaussian curve in the ratio 95:5, to obtain  $\Gamma_Z^{\text{exp95}} = 2499.6 \text{ MeV}$ . The difference between the SM lower bound and the 95% C.L. upper limit  $\Gamma_Z^{\text{exp95}}$  is  $\Delta\Gamma_Z = 4.7 \text{ MeV}$ .

- Then the LEP1 limits are applied. The upper limit on the production cross section derived from heavy stable charged particles  $\sigma_{95} = 0.296 \text{ pb}$  [86] was used. Which generally means that NLSP masses below  $\sim m_Z/2$  are excluded by LEP1.
- Finally, cross section limits from GMSB searches (and SUGRA searches for sleptons and charginos) as described in the preceding chapters are imposed on every point for which the relevant topology is accessible. In addition, limits from neutral Higgs boson searches are imposed on every scan point taking the exclusion in the plane  $(\sin^2(\beta - \alpha), m_h)$  from Fig. 4.7.

Thus a point in the parameter space is excluded if it is kinematically accessible and the excluded cross section from at least one search is less than the production cross section for that topology, taking into account the branching ratio. Cross sections for SUSY particles were calculated at seven different averaged centre-of-mass energies, as listed in Tab. 3.1.

## 5.2 Lower limit on the NLSP mass

In the stau NLSP scenario, the 95% C.L. limit on  $m_{\tilde{\tau}}$  set by direct searches (Fig. 4.5) is almost unaffected by the stau mixing and is  $77 \text{ GeV}/c^2$  for any stau lifetime, over the full scan range. Thus Fig. 4.5 from direct slepton production searches sets the minimum allowed mass for the lightest stau as a function of the stau lifetime, over the full scan range. Searches in the stau NLSP scenario for neutralino production (for four leptons and missing energy, with prompt or short decays) are not able to improve this limit.

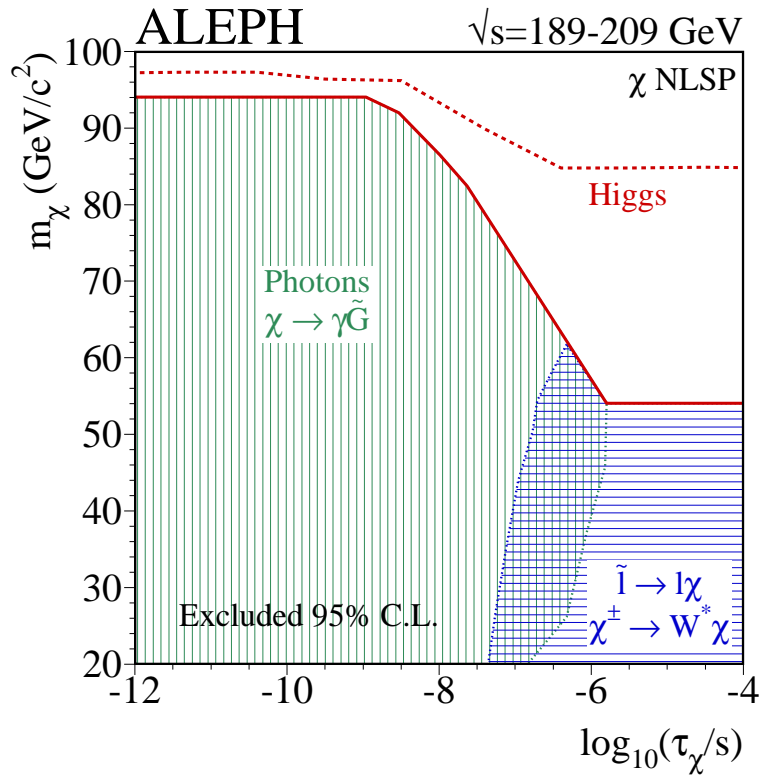


Figure 5.2: Absolute lower limit on the neutralino mass in the  $\chi$  NLSP scenario from GMSB searches as derived from the scan. The dashed line gives the lower limit obtained when searches for  $hZ$  and  $hA$  decays are included. The areas covered by searches for photons, and sleptons and charginos in SUGRA, are also shown. The search for single non-pointing photons extends into very long NLSP lifetimes, since the probability for only one neutralino decaying inside the detector is still large for lifetimes  $\sim 300$  m.

Limits on  $m_\chi$  in the neutralino NLSP scenario were shown in Fig. 4.2 assuming  $m_{\tilde{e}} = 1.1m_\chi$ . When this condition is relaxed and the full scan is tested,  $m_\chi < 94 \text{ GeV}/c^2$  remains excluded for short neutralino lifetimes. The dependence of this limit on the neutralino lifetime can be seen in Fig. 5.2 where searches for sleptons and charginos have been included to cover the long lifetime case. The absolute limit independent of lifetime is set at  $54 \text{ GeV}/c^2$  by indirect searches for sleptons and charginos in the long lifetime case.

The interplay of the different searches in the  $(m_\chi, m_{\tilde{\tau}})$  plane is shown in Fig. 5.3. For short NLSP lifetimes (Fig. 5.3a) searches for two photons, two leptons, four leptons and six leptons contribute to exclude points in this plane. It can be seen here how searches for four leptons and missing energy are able to extend the limit from acoplanar leptons searches in the slepton NLSP scenario up to  $94 \text{ GeV}/c^2$  in neutralino mass. Nevertheless, the search for six leptons and missing energy, described in Chapter 3 in this work, covers most of that area and is also able to exclude  $\tilde{\tau}_1$  masses below  $84 \text{ GeV}$  for  $m_\chi \leq 130 \text{ GeV}$ .

In Fig. 5.3b the case of long NLSP lifetimes is presented. Limits in the neutralino NLSP region are less constraining than those for the short neutralino lifetimes, due to the use of

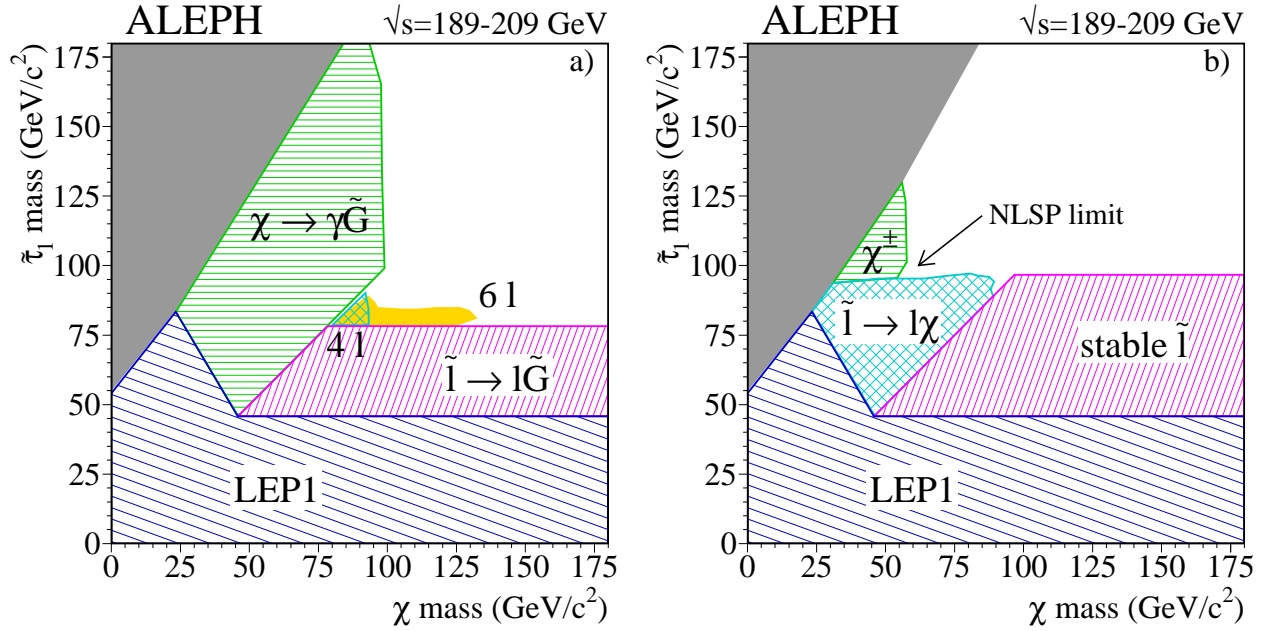


Figure 5.3: Region excluded by the different analyses described in the text at 95% confidence level in the  $(m_\chi, m_{\tilde{\tau}})$  plane for (a) short NLSP lifetimes ( $m_{\tilde{G}} \leq 10 \text{ eV}/c^2$ ) and (b) long NLSP lifetimes ( $m_{\tilde{G}} \geq 1 \text{ keV}/c^2$ ). Points in the dark region are not accessible to the scan. The absolute NLSP mass limit is set at  $54 \text{ GeV}/c^2$  in b by the intersection of chargino and slepton searches.

topologies with indirect neutralino production. The absolute lower limit on the NLSP mass of

$$m_{\text{NLSP}} \geq 54 \text{ GeV}/c^2 \quad (5.5)$$

is visible in this plot, determined by the chargino and sleptons searches. This point is found at  $N_5 = 1$ ,  $\tan\beta = 3$ ,  $\Lambda = 39 \text{ TeV}/c^2$ ,  $M_m = 10^{10} \text{ GeV}/c^2$  and  $m_{\tilde{G}} = 10^5 \text{ eV}/c^2$ , where the neutralino is the NLSP with the  $\tilde{\ell}$  masses around  $96 \text{ GeV}/c^2$  and all other supersymmetric particles above threshold.

The impact of the neutral Higgs boson searches on the neutralino and stau mass limits is shown in Fig. 5.4 as a function of  $\tan\beta$ . In this case, the NLSP absolute mass limit is  $77 \text{ GeV}/c^2$  obtained for large  $\tan\beta$  and in the stau NLSP scenario. Small values of  $\tan\beta$  are excluded almost independently of  $N_5$ .

### 5.3 Lower limit on the mass scale parameter $\Lambda$

The parameter  $\Lambda$  represents the energy scale at which the messenger particles couple to the visible sector and hence fixes the universal mass scale of SUSY particles. Hence a lower limit on the NLSP mass implies a lower limit on  $\Lambda$ . Since the relation between the masses and  $\Lambda$  depends on  $N_5$  (see Eqs. 1.17 and 1.18), it is interesting to see how this limit changes with  $N_5$ . The excluded values for the parameter  $\Lambda$  as a function of  $\tan\beta$  are shown in Fig. 5.5 for different values of  $N_5$ . In the short lifetime case the lower limit on  $\Lambda$  appears around  $12 \text{ TeV}/c^2$

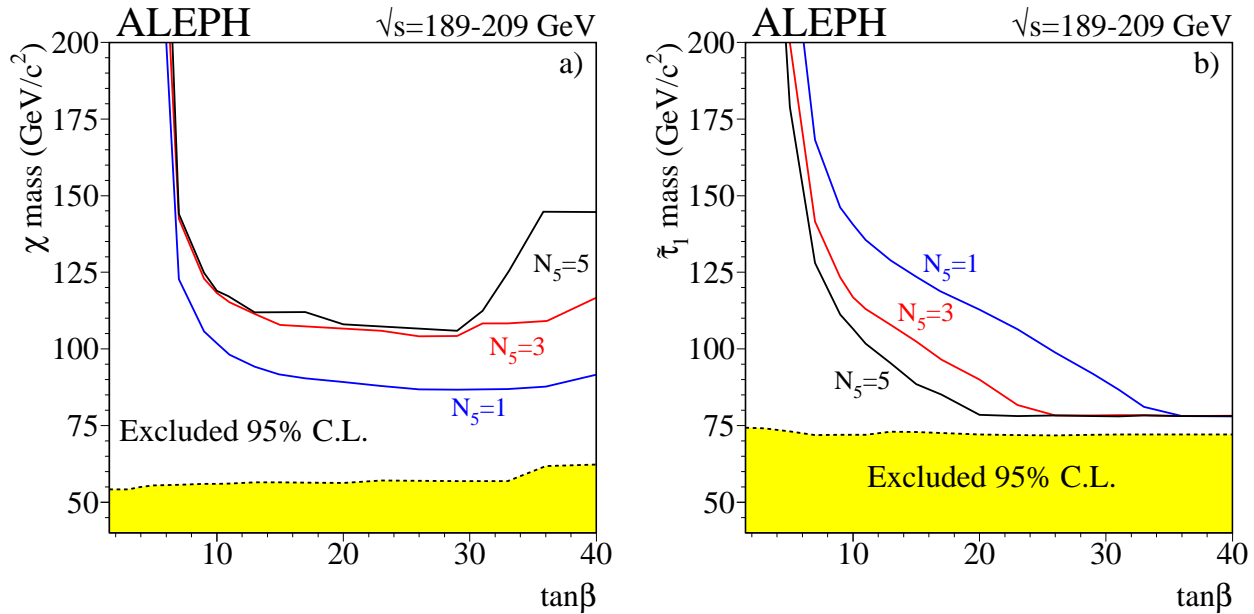


Figure 5.4: Lower limits on the masses of (a)  $\chi$  and (b)  $\tilde{\tau}_1$  as a function of  $\tan\beta$ , for different values of  $N_5$ , as set by the Higgs boson searches. The shaded area represents the minimum excluded area, for any  $N_5$ , as derived from GMSB searches alone.

for  $N_5 = 5$ . The absolute limit from the full scan is set at

$$\Lambda \gtrsim 10 \text{ TeV}/c^2 \quad (5.6)$$

in the long NLSP lifetime case. This limit is set at  $N_5 = 5$ ,  $\tan\beta = 1.5$ , and  $M_m = 10^{12} \text{ GeV}/c^2$ . The neutralino is the NLSP here with a mass of  $73 \text{ GeV}/c^2$ , slepton masses are around  $76 \text{ GeV}/c^2$  and all other sparticles are above threshold. The excluded  $\Lambda$  increases with  $\tan\beta$  as slepton NLSP searches become more relevant and improve on the indirect limits from neutralino searches alone.

Figure 5.5c shows the lower limit on  $\Lambda$  for any NLSP lifetime as a function of  $\tan\beta$ . When searches for neutral Higgs bosons are included, the excluded area significantly increases, as is shown in Fig. 5.5d, specially for low  $\tan\beta$ . For example, for  $N_5 = 1$ ,  $\Lambda$  up to  $67 \text{ TeV}/c^2$  and  $\tan\beta$  up to 6 are excluded.

Finally, the lower limit on  $\Lambda$  independent of lifetime and  $\tan\beta$  is shown in Fig. 5.6a as a function of  $N_5$ . If the Higgs exclusion is taken into account the limit on  $\Lambda$  increases up to 66, 39, 26, 20 and 16 for  $N_5 = 1, 2, 3, 4, 5$  respectively, assuming  $m_t = 175 \text{ GeV}/c^2$ .

The implication of possible extensions of the scan ranges is discussed next.

### 5.3.1 Validity of the limits

Two additional small scans are performed. One to check the limits if the number of families is increased to six, and the other to see the effect of a  $180 \text{ GeV}/c^2$  top mass on the limits derived with  $m_t = 175 \text{ GeV}/c^2$ .

The lower limit on  $\Lambda$  for  $N_5 = 6$  is 9.3 and  $14.4 \text{ TeV}/c^2$  for GMSB searches alone and Higgs boson searches, respectively. Thus the limit on the mass parameter  $\Lambda$  is reduced if more

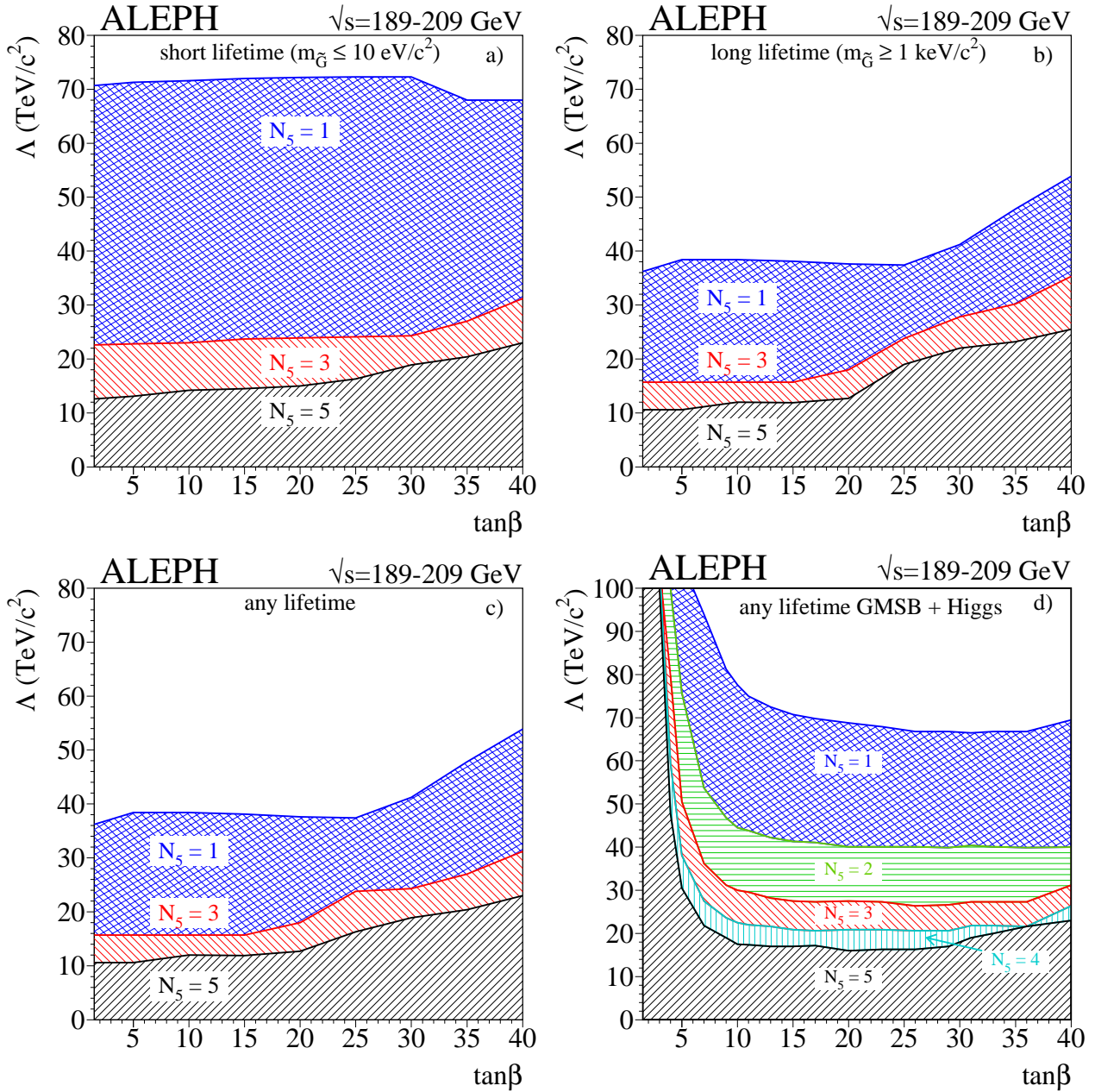


Figure 5.5: Region excluded at 95% C.L. in the  $(\Lambda, \tan\beta)$  plane for (a) short, (b) long and (c) any NLSP lifetime. The impact of the Higgs search is included in d. Values of  $\tan\beta$  less than 3 are excluded for large  $N_5$  at any mass parameter  $\Lambda$ , while  $\tan\beta$  up to 6 can be excluded for  $N_5 = 1$ .

families are included in the messenger sector. But it does so by a small amount, from around 10 to around  $9 \text{ TeV}/c^2$ , compared to the decrease from four to five messenger families.

The top mass is measured directly to be  $174.3 \pm 5.1 \text{ GeV}/c^2$  [5]. The general scan was performed assuming  $175 \text{ GeV}/c^2$ . If this is increased by the experimental error to  $180 \text{ GeV}/c^2$ , the lower limit on  $\Lambda$  for  $N_5 = 5$  from neutral Higgs boson searches is reduced from 16 to  $15 \text{ TeV}/c^2$ .

A change in the ranges of other parameters would not affect these limits on  $\Lambda$  because they are independent of the NLSP lifetime ( $m_{\tilde{G}}$  is completely covered) and larger values of  $\tan\beta$  ( $> 40$ ) may only produce lighter  $\tilde{\tau}_1$  which are already excluded.

## 5.4 Lower limit on the gravitino mass

The equation that relates the gravitino mass to the scale of SUSY breaking  $F_0$  can be exploited to put an indirect limit on the gravitino mass. Using Eq. 5.3 and the fact that the messengers ‘feel’ the SUSY breaking at a lower scale:  $F_0 > F_m$ ,

$$m_{\tilde{G}} = \frac{F_0}{\sqrt{3}M_{\text{P}}} \implies m_{\tilde{G}} > \frac{\Lambda^2}{\sqrt{3}M_{\text{P}}} \quad (5.7)$$

Thus the lower limit on  $\Lambda$  can then be converted into an indirect limit on the gravitino mass. The dependence of  $m_{\tilde{G}}$  on  $N_5$  is illustrated in Fig. 5.6b, and the lower limit of  $\Lambda > 10 \text{ TeV}/c^2$  ( $16 \text{ TeV}/c^2$  if the Higgs limits are included) implies a lower limit on  $m_{\tilde{G}}$  of  $0.024$  ( $0.061$ )  $\text{eV}/c^2$ . Therefore,

$$\boxed{m_{\tilde{G}} \gtrsim 2 \times 10^{-2} \text{ eV}/c^2} \quad (5.8)$$

This limit is set for  $N_5 = 5$ , but for only one messenger family and, if the  $hA$  and  $hZ$  limits are included, it is increased to  $1 \text{ eV}/c^2$ .



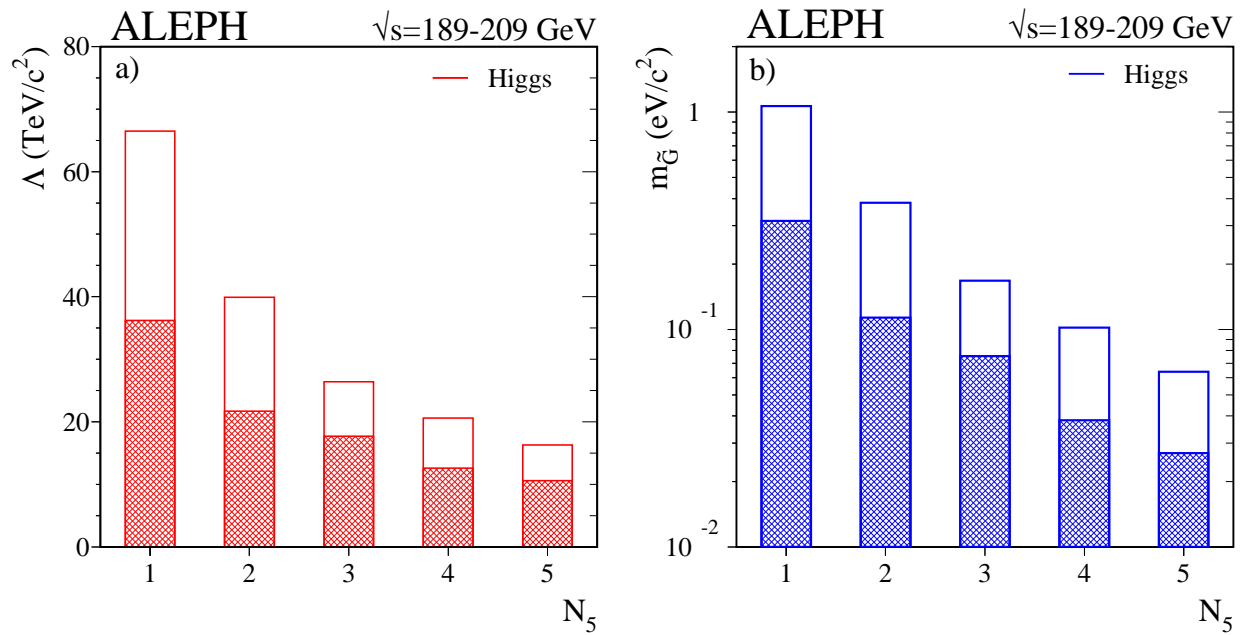


Figure 5.6: Exclusions at 95% confidence level (a) for  $\Lambda$  and (b) for  $m_{\tilde{G}}$  as a function of  $N_5$ , derived from the minimal GMSB scan (shaded). The unshaded bars represent the excluded region when the neutral Higgs boson exclusion is applied.

# Chapter 6

## Summary and discussion

### 6.1 This work

Models of supersymmetry where the MSSM masses are generated by radiative corrections due to messenger particles coupling through the gauge interactions offer an extremely rich phenomenology. Several differences arise with respect to the usual approach of gravity mediated SUSY breaking, as listed in Tab. 6.1.

mSUGRA	mGMSB
$m_{1/2}, m_0, A_0, \tan\beta, \text{sign}(\mu)$	$M_m, m_{\tilde{G}}, \Lambda, N_5, \tan\beta, \text{sign}(\mu)$
Gaugino unification mass relations (Eq. 1.16)	
Radiative EWSB (Eq. 1.14)	
$\sqrt{F_m} \sim 10^{11} \text{ GeV}$ $M_m \sim M_P$ possible FCNC $A_0 = \text{free parameter}$ $m_0^2 \gg m_{1/2}^2 \Rightarrow m_{\tilde{q}} \simeq m_{\tilde{l}} > m_\chi$ $m_0^2 \ll m_{1/2}^2 \Rightarrow m_{\tilde{q}} > m_{\tilde{l}} \simeq m_\chi$ $m_{\tilde{G}} \sim 100 \text{ GeV}/c^2$ $\chi_1^0 \text{ LSP}$	$\sqrt{F_m} \simeq 10^4 - 10^{10} \text{ GeV}$ $M_m \simeq 10^3 - 10^{15} \text{ GeV}$ no FCNC $A \simeq 0$ $m_{\tilde{q}} : m_{\tilde{l}_L} : m_{\tilde{l}_R} : m_\chi = 11 : 2.5 : 1.1 : \sqrt{N_5}$ $m_{\tilde{G}} < 1 \text{ keV}$ $\tilde{G} \text{ LSP with } \chi_1^0 \text{ or } \tilde{l}_1 \text{ NLSP,}$ NLSP has lifetime

Table 6.1: Comparison between minimal supergravity and minimal gauge mediated models.

If SUSY breaking is generated at  $M_m$  as opposed to  $M_P$ , the gravitino mass is drastically reduced and it becomes the LSP. The decay width of the next lightest sparticle to the gravitino  $\Gamma_{\text{NLSP}} \propto m_{\text{NLSP}}^5 m_{\tilde{G}}^{-2} M_P^2$  can then be small enough to produce displaced vertices inside detectors. The nature of the NLSP can be read off from Tab. 6.1 to be the neutralino if only one family of messengers exists, or the lightest slepton (usually the stau) in any other case.

In this last type of scenario, where the  $\tilde{\tau}_1$  is the NLSP and the other sleptons may be even heavier than the lightest neutralino  $\chi$ , signatures with two soft electrons or muons, four taus and missing energy are expected in ALEPH. A search for this topology has been developed

and, for the first time, special attention has been placed on three-body decays of selectrons and smuons to the corresponding lepton, a tau and the stau NLSP. A dedicated selection covered the region of very soft leptons, when the mass splitting between the sleptons and the NLSP is small. This search alone conservatively excludes selectron and smuon masses of up to 94 and 95 GeV/ $c^2$  respectively, with 95% confidence level in the case that the stau lifetime is negligible. The existing limits for selectron and smuon NLSP direct production were 98 and 93 GeV/ $c^2$ , respectively.

But the importance of this search becomes apparent when a full scan of all possible GMSB models is performed and the very many different searches are combined to understand the exclusions in a wide context. It is then proven to significantly exclude an as yet underestimated area in parameter space over that ruled out by cascade decays of neutralinos to sleptons and direct slepton decays (see Fig. 5.3a). Searches to cover almost every possible signature have been developed in ALEPH and are detailed here, including the neutral Higgs bosons searches. The interplay between the parameters of the models and the sensitivity of the limits to its variation has been studied. From the combined exclusion, and allowing the models to extend in the parameter space as much as physically possible, three model independent limits are set:

- The mass of the NLSP is excluded up to 77 GeV/ $c^2$  (see Tab. 6.2 for details).

NLSP	mass limit (95% C.L.)	validity
$\chi$	92 GeV/ $c^2$	short $\chi$ lifetime ( $m_{\tilde{G}} \leq 10$ eV/ $c^2$ )
	54 GeV/ $c^2$	any lifetime
$\tilde{\tau}_1$	77 GeV/ $c^2$	any lifetime
any	77 GeV/ $c^2$	Higgs exclusion

Table 6.2: NLSP mass limits from GMSB searches, as derived from the scan.

- The universal mass scale parameter  $\Lambda$  is excluded up to 16 TeV/ $c^2$  for  $N_5 = 5$ . This limit is not expected to be affected much for larger  $N_5$ . Values of  $\Lambda$  in excess of  $\sim \frac{100}{N_5}$  TeV/ $c^2$  would produce very heavy sparticles, destroying the solution to the hierarchy problem.
- The mass of the gravitino can be indirectly excluded up to  $6 \times 10^{-2}$  eV/ $c^2$ , or equivalently, the SUSY breaking scale  $\sqrt{F_0}$  has to be greater than 16 TeV. Cosmology bounds  $\sqrt{F_0}$  from above at  $\sim 1000$  TeV.

The above limits are calculated with neutral Higgs bosons results and GMSB results as described in Chapter 4.

## 6.2 GMSB after LEP

Supersymmetry has escaped detection at LEP, but the techniques and limits from this machine will be valuable for future experiments which will surely discover it, if it exists. The LEP collaborations have all developed very similar searches for possible GMSB signals, as described in Refs. [53, 67, 87]. The OPAL collaboration sets lower limits on the SUSY mass scale of  $\Lambda > 40, 27, 21, 17, 15$  TeV/ $c^2$  for  $N_5 = 1, 2, 3, 4, 5$  respectively, taking all NLSP lifetimes into account in a similar scan to the one described in this work. DELPHI quotes a limit of  $\Lambda > 17.5$  TeV/ $c^2$  for  $N_5 = 4$  and negligible NLSP lifetime. Only the ALEPH collaboration

has included neutral Higgs boson searches into the GMSB analysis, rendering better limits. As regards the NLSP mass, OPAL excludes them below 53.5, 87.4 and 93.7 GeV/ $c^2$  in the neutralino, stau and slepton NLSP scenarios respectively. DELPHI has also looked for direct evidence of a massive sgoldstino  $S$  (the bosonic superpartner of the goldstino, with even  $R_P$  and produced via:  $e^+e^- \rightarrow S\gamma$ ), in topologies with three energetic photons ( $S \rightarrow \gamma\gamma$ ) or two jets and one photon ( $S \rightarrow g\gamma$ ). This search allows direct exclusion of the SUSY breaking scale  $\sqrt{F_0}$  up to 650 GeV for a light sgoldstino.

To conclude, Fig. 6.1 gives the status of the full MSSM spectrum in gauge mediated models after the LEP era. With the scan described in Chapter 5 and using only the ALEPH exclusions as described here, the final excluded masses at 95% confidence level have been computed for each messenger index  $N_5$ . The ongoing LEP wide combination [88] of results will improve these limits.

## 6.3 Prospects

The allowed parameter space in GMSB for searches where the stau is the NLSP and selectrons and smuons are lighter than the neutralino is extremely large, and will surely be tested in the near future with new data. At the incipient Run II of the Tevatron in Fermilab with  $\sqrt{s} = 2$  TeV, the dominant SUSY production is  $p\bar{p} \rightarrow \chi_1^+ \chi_1^-$  or  $\chi_1^\pm \chi_2^0$  through off-shell W and Z. Charginos will tend to decay through their higgsino components by  $\chi_1^\pm \rightarrow \chi_1^0 W^\pm$  and likewise for the neutralino  $\chi_2^0 \rightarrow \chi_1^0 Z^0$ . Thus for a neutralino NLSP scenario, final states consisting of  $W^\pm Z^0 + \gamma\gamma + \cancel{E}_T$  and  $W^+W^- + \gamma\gamma + \cancel{E}_T$  will potentially lead to a discovery. The DØ collaboration [89], expects to be able to discover charginos of masses up to 290 (340) GeV/ $c^2$  in the  $\gamma\gamma + \cancel{E}_T$  signature in the prompt  $\chi$  NLSP decays for a collected luminosity of 2 fb $^{-1}$  (30 fb $^{-1}$ ) by the end of the year 2004 (2007+). In the case of a stau NLSP, stau masses up to 160 (200) GeV/ $c^2$  and chargino masses up to 340 (410) GeV/ $c^2$ , will be discovered if the stau is long-lived for the same luminosities. The LEP limits ( $2\sigma$  exclusion), as derived from the scan in this work, for the gluino and chargino masses, as a function of  $\tan\beta$  and  $N_5$  can be seen in Fig. 6.2. Overlaid in the chargino mass plot are the DØ discovery reaches ( $5\sigma$ ) in the  $\chi$  NLSP case for short lifetimes and the stau NLSP case for long lifetimes.

The task for the Large Hadron Collider at CERN ( $\sim 2007$ ) would then be to unravel the nature of SUSY breaking and measure the parameters of the theory with  $\sim 10\%$  accuracy. Present and future colliders are opening a new energy range in physics, thus at the beginning of this century we are about to test new theories that may reshape our understanding of spacetime... or even better, be surprised by something completely unexpected. Whether it is supersymmetry or something else, it is surely going to be exciting.

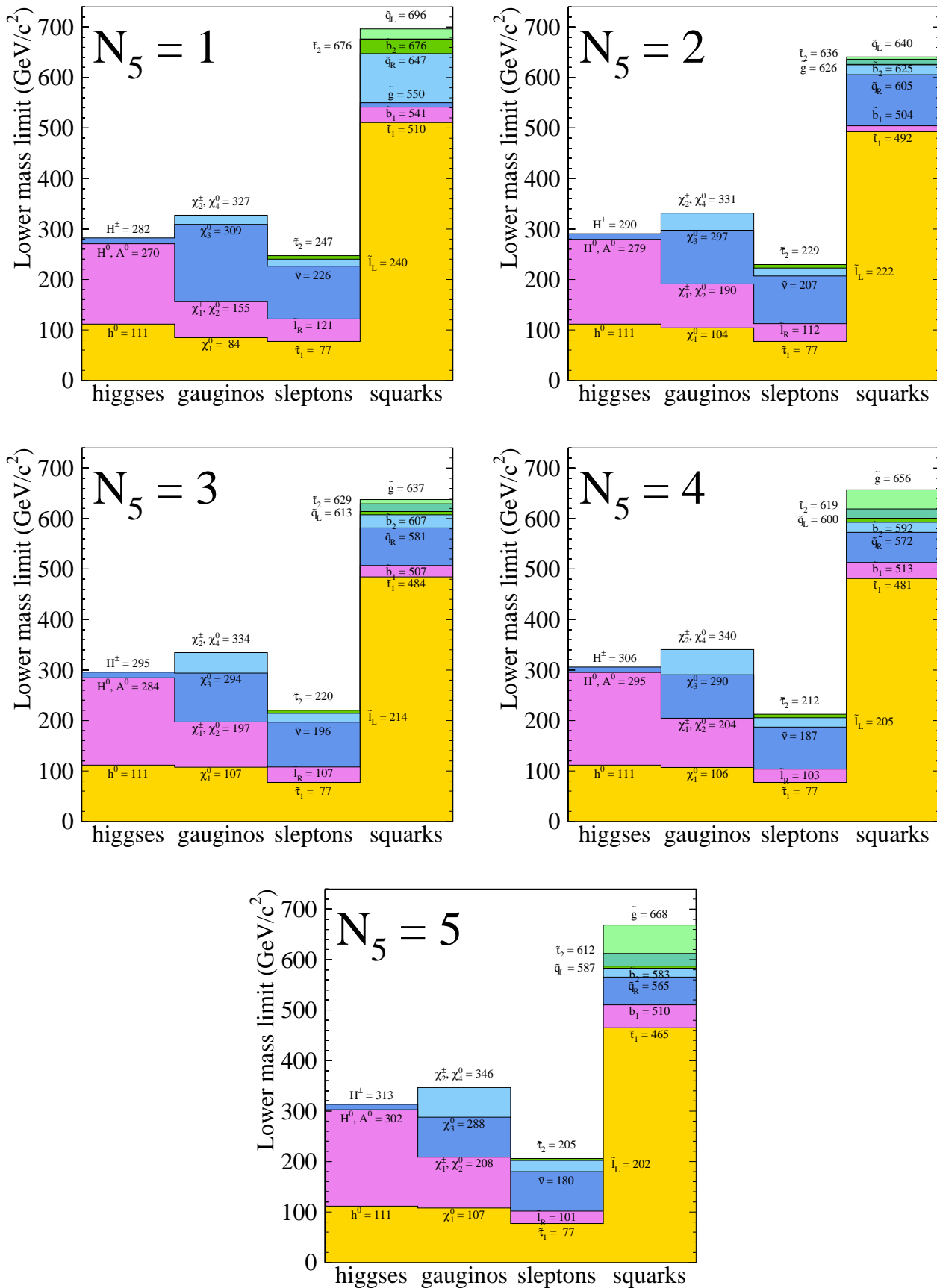


Figure 6.1: Lower mass limit for all supersymmetric particles as a function of the number of messenger families. The limits are derived from the scan after applying GMSB and neutral Higgs boson searches results. Higher masses may be excluded for certain regions of parameter space. Thus these limits define the minimum allowed values for the masses for all possible GMSB models inside the ranges described in the scan (Tab. 5.1).

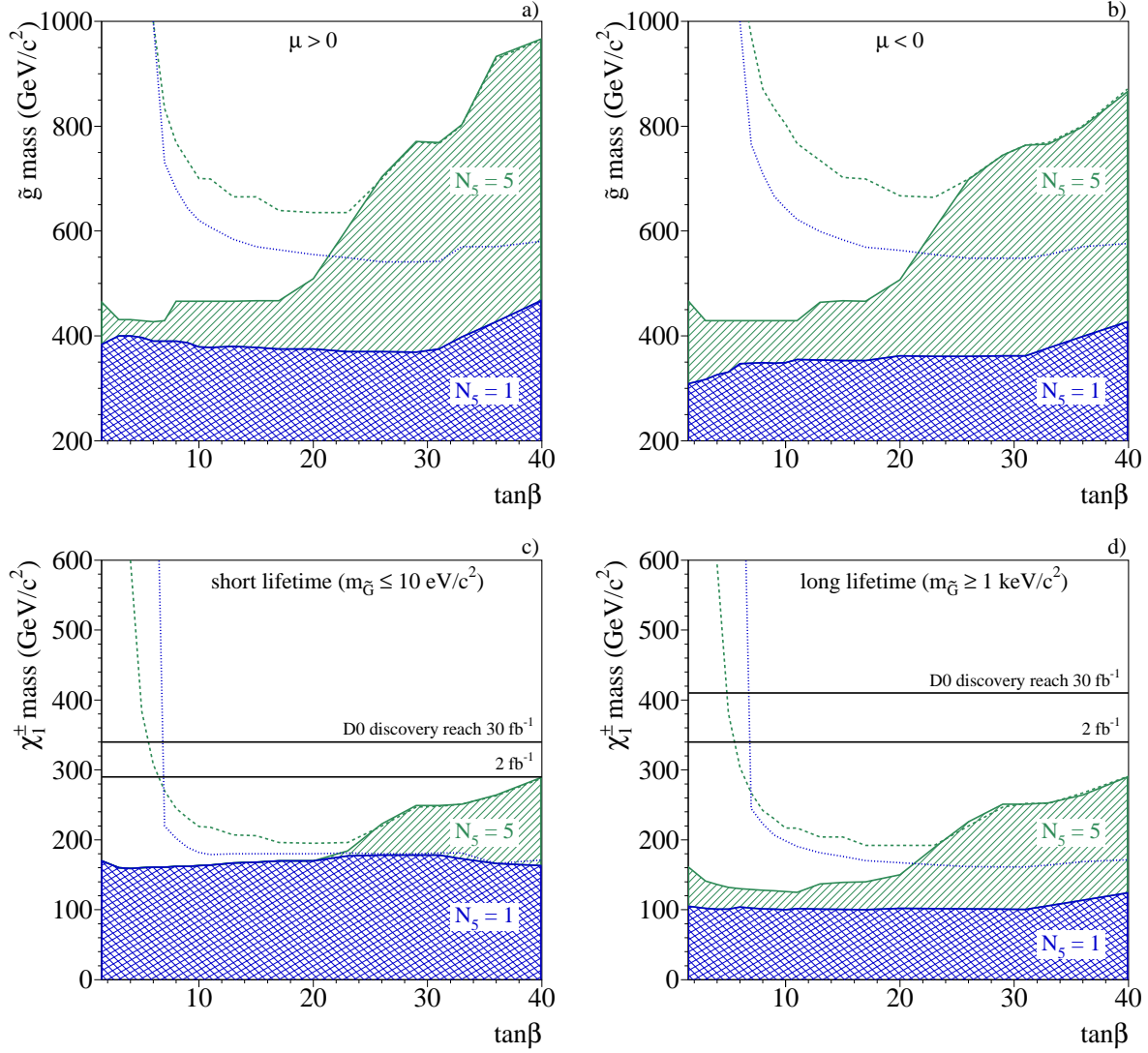


Figure 6.2: 95% C.L. exclusion on the gluino mass for (a) positive and (b) negative  $\mu$ , for models with one or five messenger families, as derived from the GMSB searches. The lower limit on the chargino mass at 95% C.L. is displayed for (c) short and (d) long NLSP lifetimes respectively. The dotted lines represent the lower limit from GMSB and Higgs boson searches for  $N_5 = 1$  and the dashed line for  $N_5 = 5$ .

# List of Figures

1.1	The Higgs potential . . . . .	5
1.2	One-loop contributions to the Higgs mass . . . . .	7
1.3	Gauge couplings evolution with energy in the SM and the MSSM . . . . .	10
1.4	Diagram of SUSY mediation and energy scales . . . . .	14
1.5	Coupling of messenger particles to gauginos and scalars through radiative loops . . . . .	15
1.6	Production of SUSY particles and MSSM Higgs neutral bosons at LEP when R-parity is conserved . . . . .	17
1.7	The NLSP nature as a function of parameters . . . . .	18
1.8	Evolution of sparticle masses with $M_m$ . . . . .	19
2.1	An overview of the LEP accelerator . . . . .	21
2.2	End-on view of the ALEPH detector showing all its subdetectors . . . . .	23
2.3	ALEPH coordinate system . . . . .	24
2.4	The vertex detector . . . . .	24
2.5	Drift cell geometry of the ITC . . . . .	25
2.6	TPC overall view . . . . .	26
2.7	TPC sector edge and gating diagrams . . . . .	27
2.8	TPC particle identification by $dE/dx$ and momentum measurements . . . . .	28
2.9	Detail of an ECAL layer . . . . .	29
2.10	Overview of the calorimeters . . . . .	30
2.11	ALEPH hermeticity and energy flow resolution . . . . .	35
2.12	Lepton identification efficiencies . . . . .	37
3.1	Slepton decay to a lepton, tau and stau . . . . .	41
3.2	Sparticles pair-production cross sections at $\sqrt{s} = 207$ GeV as a function of their mass . . . . .	42
3.3	Different NLSP regions in the $(\Lambda, \tan \beta)$ plane . . . . .	44
3.4	Slepton decay modes contribution to the total branching fraction as a function of $\tan \beta$ . . . . .	45
3.5	Energy distributions for the lepton and the primary tau in two- and three-body scenarios . . . . .	46
3.6	Signal Monte Carlo events at $\sqrt{s} = 208$ GeV . . . . .	47
3.7	Values of $m_{\tilde{l}_R}$ , $m_\chi$ and $m_{\tilde{\tau}_1}$ for each signal point in the two- and three-body scenarios . . . . .	49
3.8	Distribution of signal points in the $(m_{\tilde{\tau}_1}, m_\chi)$ plane . . . . .	50
3.9	Cross sections for Standard Model processes as a function of the centre-of-mass energy . . . . .	51
3.10	Feynman diagrams of SM background processes . . . . .	52
3.11	Background distributions in $(M_{\text{vis}}, M_{\text{had}})$ and $(y_{23}, y_{34})$ . . . . .	56

3.12	Distributions of data, expected background and signal in the large $\Delta m$ selection after preselection and anti- $\gamma\gamma$ cuts for the remaining cut variables . . . . .	57
3.13	Distributions of data, expected background and signal in the small $\Delta m$ selection after preselection and anti- $\gamma\gamma$ cuts for the remaining cut variables . . . . .	58
3.14	$\bar{N}_{95}$ as a function of the expected background $b$ . . . . .	60
3.15	Optimisation procedure . . . . .	60
3.16	The efficiency of the small and large $\Delta m$ selections as a function of $\Delta m$ for all analysed signal points . . . . .	61
3.17	Event displays of the selected data . . . . .	64
3.18	$CL_s$ for the two selections as a function of the selectron and smuon mass . . .	65
3.19	95% C.L. excluded cross section areas as a function of the slepton mass . . . .	67
4.1	Two-photon analysis results . . . . .	71
4.2	Excluded neutralino mass as a function of its lifetime and as a function of the selectron mass . . . . .	72
4.3	Excluded regions at 95% C.L. in the $(m_{\tilde{\ell}_R}, m_\chi)$ plane in the acoplanar leptons SUGRA search . . . . .	74
4.4	Efficiency of the search for heavy stable charged particles and its excluded cross section . . . . .	77
4.5	Excluded stau mass as a function of its lifetime in the stau NLSP scenario . .	78
4.6	Efficiencies in the cascade decays with zero lifetime and the combined efficiency as a function of lifetime . . . . .	80
4.7	Results of the neutral Higgs boson searches in the $(\sin^2(\beta - \alpha), m_h)$ plane . . .	82
5.1	Procedure to determine the allowed SUSY contribution to $\Gamma_Z$ . . . . .	86
5.2	Absolute lower limit on $m_\chi$ as a function of the $\chi$ NLSP lifetime . . . . .	87
5.3	Excluded area in the $(m_\chi, m_{\tilde{\tau}})$ plane . . . . .	88
5.4	Lower limits on $m_{\tilde{\tau}_1}$ and $m_\chi$ as a function of $\tan\beta$ . . . . .	89
5.5	Region excluded at 95% C.L. in the $(\Lambda, \tan\beta)$ plane . . . . .	90
5.6	Excluded $\Lambda$ and $m_{\tilde{G}}$ as a function of $N_5$ . . . . .	92
6.1	Lower mass limit for all supersymmetric particles as a function of the number of messenger families . . . . .	96
6.2	Gluino and chargino excluded masses as a function of $\tan\beta$ . . . . .	97



# List of Tables

1.1	Interactions and carrier particles . . . . .	3
1.2	Fermion summary table . . . . .	3
1.3	The MSSM particle zoo . . . . .	11
1.4	The four possible NLSP scenarios . . . . .	19
2.1	Summary of the ALEPH trigger system. . . . .	32
2.2	Momentum resolution in the ALEPH tracking subdetectors . . . . .	33
2.3	Tau branching ratios. . . . .	38
3.1	ALEPH collected luminosity by centre-of-mass energy bin . . . . .	48
3.2	Number of events generated and cross sections for the SM background processes analysed in the six-lepton search . . . . .	53
3.3	Selection criteria for six-lepton final states with large $\Delta m$ . . . . .	54
3.4	Selection criteria for six-lepton final states with small $\Delta m$ . . . . .	55
3.5	Number of candidate events in the six-lepton selections . . . . .	62
3.6	List of candidate events . . . . .	63
4.1	Possible final state topologies in GMSB . . . . .	69
4.2	List of cuts used in searches for a $\chi$ NLSP . . . . .	72
4.3	List of cuts for the large impact parameter and kinks selections . . . . .	75
4.4	List of cuts for the heavy stable charged particle selection for intermediate-high masses . . . . .	76
4.5	Number of observed and expected events in the searches for four leptons and missing energy . . . . .	79
4.6	$hZ$ and $hA$ decays . . . . .	81
5.1	Minimal set of parameters and their ranges of variation in the scan . . . . .	84
6.1	Comparison between minimal supergravity and minimal gauge mediated models. . .	93
6.2	NLSP mass limits from GMSB searches, as derived from the scan. . . . .	94

# Bibliography

- [1] S. L. Glashow, *Partial symmetries of weak interactions*, Nucl. Phys. **22**, 579–588 (1961).
- [2] S. Weinberg, *A model of leptons*, Phys. Rev. Lett. **19**, 1264–1266 (1967).
- [3] A. Salam, in *Proceedings of the 8th Nobel Symposium*, edited by N. Svartholm, (Almqvist and Wiksells, Stockholm, 1968), p. 367.
- [4] F. Halzen and A. D. Martin, *Quarks and leptons*, (John Wiley and sons, New York, 1984).
- [5] K. Hagiwara et al., *Review of particle physics*, Phys. Rev. **D66**, 010001 (2002).
- [6] P. W. Higgs, *Broken symmetries, massless particles and gauge fields*, Phys. Lett. **12**, 132–133 (1964).
- [7] F. Englert and R. Brout, *Broken symmetry and the mass of gauge vector mesons*, Phys. Rev. Lett. **13**, 321–322 (1964).
- [8] S. Armstrong, *A search for the Standard Model Higgs boson in four-jet final states at centre-of-mass energies near 183 GeV with the ALEPH detector at LEP*, Ph.D. thesis, University of Wisconsin-Madison (1998).
- [9] J. Goldstone, A. Salam and S. Weinberg, *Broken symmetries*, Phys. Rev. **127**, 965–970 (1962).
- [10] D. Wark, *Neutrino masses and oscillations*, in *Proceedings of ICHEP 2002 Amsterdam*, <http://www.ichep02.nl>.
- [11] Q. R. Ahmad et al., *Direct evidence for neutrino flavor transformation from neutral-current interactions in the Sudbury Neutrino Observatory*, Phys. Rev. Lett. **89**, 011301 (2002), nucl-ex/0204008.
- [12] G. Altarelli and F. Feruglio, *Neutrino masses and mixings: A theoretical perspective* (1999), hep-ph/9905536.
- [13] K. A. Olive, G. Steigman and T. P. Walker, *Primordial nucleosynthesis: Theory and observations*, Phys. Rept. **333**, 389–407 (2000), astro-ph/9905320.
- [14] A. E. Lange et al., *Cosmological parameters from the first results of BOOMERANG*, Phys. Rev. **D63**, 042001 (2001), astro-ph/0005004.
- [15] V. Rubakov, *Cosmology and Astrophysics*, in *2001 European School of High Energy Physics*, CERN 2002-02.

- [16] A. D. Sakharov, *Violation of CP invariance, C asymmetry, and baryon asymmetry of the Universe*, Pisma Zh. Eksp. Teor. Fiz. **5**, 32–35 (1967).
- [17] G. R. Farrar and M. E. Shaposhnikov, *Baryon asymmetry of the universe in the standard electroweak theory*, Phys. Rev. **D50**, 774 (1994), hep-ph/9305275.
- [18] S. R. Coleman and J. Mandula, *All possible symmetries of the S matrix*, Phys. Rev. **159**, 1251–1256 (1967).
- [19] R. Haag, J. T. Lopuszanski and M. Sohnius, *All possible generators of Supersymmetries of the S matrix*, Nucl. Phys. **B88**, 257 (1975).
- [20] J. R. Ellis, *Supersymmetry for Alp hikers* (2002), hep-ph/0203114.
- [21] J. Wess and B. Zumino, *A lagrangian model invariant under supergauge transformations*, Phys. Lett. **B49**, 52 (1974).
- [22] LEP Electroweak Working Group. <http://lepewwg.web.cern.ch/LEPEWWG/>.
- [23] LEP Higgs Working Group. <http://lephiggs.web.cern.ch/LEPHIGGS/www/>.
- [24] U. Amaldi, W. de Boer and H. Furstenau, *Comparison of grand unified theories with electroweak and strong coupling constants measured at LEP*, Phys. Lett. **B260**, 447–455 (1991).
- [25] H. K. Dreiner, *An introduction to explicit R-parity violation* (1997), hep-ph/9707435.
- [26] E. Witten, *Dynamical breaking of supersymmetry*, Nucl. Phys. **B188**, 513 (1981).
- [27] L. Girardello and M. T. Grisaru, *Soft breaking of Supersymmetry*, Nucl. Phys. **B194**, 65 (1982).
- [28] S. P. Martin, *A supersymmetry primer* (1997), hep-ph/9709356.
- [29] G. F. Giudice and R. Rattazzi, *Theories with gauge-mediated supersymmetry breaking*, Phys. Rept. **322**, 419–499 (1999), hep-ph/9801271.
- [30] H. P. Nilles, *Supersymmetry, supergravity and particle Physics*, Phys. Rept. **110**, 1 (1984).
- [31] J. L. Feng and T. Moroi, *Tevatron signatures of long-lived charged sleptons in gauge-mediated supersymmetry breaking models*, Phys. Rev. **D58**, 035001 (1998), hep-ph/9712499.
- [32] S. Ambrosanio, G. D. Kribs and S. P. Martin, *Signals for gauge-mediated supersymmetry breaking models at the CERN LEP2 collider*, Phys. Rev. **D56**, 1761–1777 (1997), hep-ph/9703211.
- [33] S. Dimopoulos, S. Thomas and J. D. Wells, *Sparticle spectroscopy and electroweak symmetry breaking with gauge-mediated supersymmetry breaking*, Nucl. Phys. **B488**, 39–91 (1997), hep-ph/9609434.
- [34] A. Heister et al., *Single- and multi-photon production in e+e- collisions at  $\sqrt{s}$  up to 209 GeV* CERN-EP-2002-033.

- [35] *LEP Design Report* CERN-LEP/84-01.
- [36] G. Altarelli, T. Sjostrand, F. Zwirner (eds.), *Physics at LEP2* (1996), CERN/96-01.
- [37] <http://press.web.cern.ch/Press/Photos>.
- [38] <http://alephwww.cern.ch/EDUC/alephdesc.html>.
- [39] D. Decamp et al., *ALEPH: A Detector for electron-positron annihilations at LEP*, Nucl. Instrum. Meth. **A294**, 121–178 (1990).
- [40] C. Bowdery (ed.), *The ALEPH Handbook 1995 Vol. 1*, European Organization for Nuclear Research, CERN, Geneva (1995).
- [41] C. Bowdery (ed.), *The ALEPH Handbook 1995 Vol. 2*, European Organization for Nuclear Research, CERN, Geneva (1995).
- [42] D. Buskulic et al., *Performance of the ALEPH detector at LEP*, Nucl. Instrum. Meth. **A360**, 481–506 (1995).
- [43] D. Creanza et al., *The new ALEPH Silicon Vertex Detector*, Nucl. Instrum. Meth. **A409**, 157 (1998).
- [44] G. J. Barber et al., *Performance of the Three-Dimensional Readout of the ALEPH Inner Tracking Chamber*, Nucl. Instrum. Meth. **A279**, 212 (1989).
- [45] W. B. Atwood et al., *Performance of the ALEPH Time Projection Chamber*, Nucl. Instrum. Meth. **A306**, 446–458 (1991).
- [46] J. Knobloch, *JULIA Users and Programmers Guide*, Tech. Rep. ALEPH 90-11, ALEPH internal report (1990), <http://alephwww.cern.ch/LIGHT/julia.html>.
- [47] H. Albrecht, E. Blucher and J. Boucrot, *ALEPH Physics Analysis Package - ALPHA User's guide - versions > 124*, Tech. Rep. ALEPH 99-087, ALEPH internal report (1999), <http://alephwww.cern.ch/LIGHT/alpha.html>.
- [48] P. Billoir, *Track fitting with multiple scattering: a new method*, Nucl. Instr. Meth. **A225**, 352 (1984).
- [49] J. M. Nachtman, Search for charginos at 161-GeV and 172-GeV with the ALEPH detector, Ph.D. thesis, University of Wisconsin-Madison (1997), UMI-98-07835.
- [50] Y. L. Dokshitzer, V. A. Khoze and S. I. Troian, *Particle spectra in light and heavy quark jets*, J. Phys. **G17**, 1481–1492 (1991).
- [51] R. Brun, F. Bruyant, M. Maire, A. C. McPherson and P. Zancarini, *GEANT3* CERN-DD/EE/84-1.
- [52] F. Ranjard, *GALEPH - Monte Carlo Program for ALEPH*, Tech. Rep. ALEPH 88-119, ALEPH internal report (1988), <http://alephwww.cern.ch/LIGHT/galeph.html>.
- [53] G. Abbiendi et al., *Searches for GMSB signatures in  $e+e-$  collisions at  $\sqrt{s} = 189 - 208$  GeV* Contributed paper to ICHEP 2002 Amsterdam, OPAL PN504.

- [54] S. Ambrosanio, G. D. Kribs and S. P. Martin, *Three-body decays of selectrons and smuons in low-energy supersymmetry breaking models*, Nucl. Phys. **B516**, 55–69 (1998), hep-ph/9710217.
- [55] H. Baer, P. G. Mercadante, X. Tata and Y.-l. Wang, *The reach of Tevatron upgrades in gauge-mediated supersymmetry breaking models*, Phys. Rev. **D60**, 055001 (1999), hep-ph/9903333.
- [56] S. Katsanevas and P. Morawitz, *SUSYGEN-2.2: A Monte Carlo event generator for MSSM sparticle production at  $e+e-$  colliders*, Comput. Phys. Commun. **112**, 227 (1998), hep-ph/9711417, <http://lyoinfo.in2p3.fr/susygen/susygen.html>.
- [57] H. Baer, F. E. Paige, S. D. Protopopescu and X. Tata, *ISAJET 7.48: A Monte Carlo event generator for  $p p$ , anti- $p p$ , and  $e+e-$  reactions* (1999), hep-ph/0001086, <http://paige.home.cern.ch/paige/>.
- [58] S. Jadach, W. Placzek and B. F. L. Ward, *BHWIDE 1.00:  $O(\alpha)$  YFS exponentiated Monte Carlo for Bhabha scattering at wide angles for LEP1/SLC and LEP2*, Phys. Lett. **B390**, 298–308 (1997), hep-ph/9608412.
- [59] S. Jadach, B. F. L. Ward and Z. Was, *The Monte Carlo program KORALZ, for the lepton or quark pair production at LEP/SLC energies: From version 4.0 to version 4.04*, Comput. Phys. Commun. **124**, 233–237 (2000), hep-ph/9905205.
- [60] M. Skrzypek, S. Jadach, W. Placzek and Z. Was, *Monte Carlo program KORALW-1.02 for  $W$  pair production at LEP-2 / NLC energies with Yennie-Frautschi-Suura exponentiation*, Comput. Phys. Commun. **94**, 216–248 (1996).
- [61] T. Sjostrand et al., *High-energy-physics event generation with PYTHIA 6.1*, Comput. Phys. Commun. **135**, 238–259 (2001), hep-ph/0010017.
- [62] D. Buskulic et al., *An Experimental study of  $\gamma\gamma \rightarrow$  hadrons at LEP*, Phys. Lett. **B313**, 509–519 (1993).
- [63] J. F. Grivaz and F. Le Diberder, *Complementary analyses and acceptance optimization in new particle searches LAL-92-37*.
- [64] G. Cowan, *Statistical data analysis*, (Oxford University Press, Oxford, 1998).
- [65] A. Heister et al., *Search for gauge mediated SUSY breaking topologies in  $e+e-$  collisions at centre-of-mass energies up to 209 GeV*, Eur. Phys. J. **C25**, 339–351 (2002), hep-ex/0203024.
- [66] T. Junk, *Confidence level computation for combining searches with small statistics*, Nucl. Instrum. Meth. **A434**, 435–443 (1999), hep-ex/9902006, <http://thomasj.home.cern.ch/thomasj/searchlimits/ecl.html>.
- [67] T. Alderweireld et al., *Update of the search for supersymmetric particles in light gravitino* Contributed paper to ICHEP 2002 Amsterdam, DELPHI 2002-024, CONF 558.
- [68] S. Jadach, B. F. L. Ward and Z. Was, *The precision Monte Carlo event generator KK for two-fermion final states in  $e+e-$  collisions*, Comput. Phys. Commun. **130**, 260–325 (2000), hep-ph/9912214.

- [69] G. Montagna, M. Moretti, O. Nicosini and F. Piccinini, *Single- and multi-photon final states with missing energy at  $e+e-$  colliders*, Nucl. Phys. **B541**, 31–49 (1999), hep-ph/9807465.
- [70] S. Dimopoulos, S. Thomas and J. D. Wells, *Implications of low energy supersymmetry breaking at the Tevatron*, Phys. Rev. **D54**, 3283–3288 (1996), hep-ph/9604452.
- [71] F. Abe et al., *Searches for new physics in diphoton events in  $p$  anti- $p$  collisions at  $\sqrt{s} = 1.8$ -TeV*, Phys. Rev. **D59**, 092002 (1999), hep-ex/9806034.
- [72] S. Ambrosanio, G. L. Kane, G. D. Kribs, S. P. Martin and S. Mrenna, *Supersymmetric analysis and predictions based on the CDF  $ee\gamma\gamma +$  missing  $E_T$  event*, Phys. Rev. Lett. **76**, 3498–3501 (1996), hep-ph/9602239.
- [73] A. Heister et al., *Search for scalar leptons in  $e+e-$  collisions at centre-of-mass energies up to 209-GeV*, Phys. Lett. **B526**, 206–220 (2002), hep-ex/0112011.
- [74] A. Heister et al., *results on chargino and neutralino searches in  $e+e-$  collisions up to  $\sqrt{s} = 209$  GeV and mass limit for the lightest neutralino including stau mixing* In preparation. To be submitted to Phys. Lett. B.
- [75] R. Barate et al., *Search for charginos and neutralinos in  $e+e-$  collisions at centre-of-mass energies near 183-GeV and constraints on the MSSM parameter space*, Eur. Phys. J. **C11**, 193–216 (1999).
- [76] R. Barate et al., *Search for gauge mediated SUSY breaking topologies at  $\sqrt{s} \sim 189$ -GeV*, Eur. Phys. J. **C16**, 71–85 (2000).
- [77] R. Barate et al., *Search for pair-production of long-lived heavy charged particles in  $e+e-$  annihilation*, Phys. Lett. **B405**, 379–388 (1997), hep-ex/9706013.
- [78] L. T. Jones, *A search for GMSB sleptons with lifetime at ALEPH*, Ph.D. thesis, Royal Holloway University of London (2001), hep-ex/0110022.
- [79] R. Barate et al., *Searches for neutral Higgs bosons in  $e+e-$  collisions at centre-of-mass energies from 192-GeV to 202-GeV*, Phys. Lett. **B499**, 53–66 (2001), hep-ex/0010062.
- [80] A. Heister et al., *Final results of the searches for neutral Higgs bosons in  $e+e-$  collisions at  $\sqrt{s}$  up to 209-GeV*, Phys. Lett. **B526**, 191–205 (2002), hep-ex/0201014.
- [81] P. Janot, *The HZHA generator* <http://alephwww.cern.ch/~janot/Generators.html>.
- [82] T. Gherghetta, G. F. Giudice and A. Riotto, *Nucleosynthesis bounds in gauge-mediated supersymmetry breaking theories*, Phys. Lett. **B446**, 28–36 (1999), hep-ph/9808401.
- [83] S. L. Dubovsky, D. S. Gorbunov and S. V. Troitsky, *Gauge mechanism of mediation of supersymmetry breaking*, Phys. Usp. **42**, 623–651 (1999), hep-ph/9905466.
- [84] T. Moroi, *Effects of the gravitino on the inflationary universe* (1995), hep-ph/9503210.
- [85] D. Y. Bardin et al., *ZFITTER v.6.21: A semi-analytical program for fermion pair production in  $e+e-$  annihilation*, Comput. Phys. Commun. **133**, 229–395 (2001), hep-ph/9908433.

- 
- [86] D. Decamp et al., *Searches for new particles in Z decays using the ALEPH detector*, Phys. Rept. **216**, 253–340 (1992).
- [87] P. Achard et al., *Search for Supersymmetry in  $e+e-$  collisions at  $\sqrt{s} = 202 - 208$  GeV*, Contributed paper to Moriond 2002, L3 note 2731.
- [88] LEP SUSY Working Group. <http://lepsusy.web.cern.ch/lepsusy/>.
- [89] J.-m. Qian, *Sensitivity to gauge-mediated supersymmetry breaking models of the Fermilab upgraded Tevatron collider* (1998), hep-ph/9903548.